

Mode Control with a Diode-pumped Solid-State Digital Laser

Teboho Bell

2017

Mode Control with a Diode-pumped Solid-State Digital Laser



UNIVERSITY OF TM
KWAZULU-NATAL

INYUVESI
YAKWAZULU-NATALI

Teboho Bell

Supervisor: Dr Sandile Ngcobo

Co-Supervisor: Dr Mathew Moodley

College of Agriculture, Engineering and Science
School of Chemistry and Physics

This thesis is submitted for the degree of

Doctor of Philosophy

June 2017

Supervisor's declaration

I, Dr _____, declare as follows:

1. The work described by this thesis was carried out at the Council for Scientific and Industrial Research (CSIR), Pretoria, between **03 February 2014** and **15 December 2016**, under the supervision of **Dr S. Ngcobo** of the CSIR and co-supervised by **Dr M.K. Moodley** of the University of KwaZulu-Natal (UKZN).
2. The work described in this thesis has not been submitted to UKZN or to any other tertiary institution for purposes of obtaining an academic qualification, whether by myself or any other party.

Signed:.....

Name:.....

Date:.....

Teboho Bell

June 2017

Author's declaration

I declare that the work in this thesis was carried out in accordance with the requirements of the regulations and Code of Practice for Research Degree Programmes of the University of KwaZulu-Natal and that it has not been submitted for any other academic award. Except where indicated by specific reference in the text, the work is the candidate's own work. People who contributed to this work have been acknowledged accordingly. Any views expressed in the thesis are those of the author.

Signed: .....
Name:.....**Teboho Bell**.....
Date:.....**14.06.2017**.....

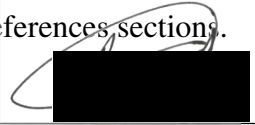
Teboho Bell
June 2017

*This thesis is dedicated to my late grandparent Charlie and Annah Bell;
my late sister Elizabeth Bell
and my late friend and colleague Nompumelelo Basi
....May their souls rest in peace....*

Plagiarism

I, Teboho Bell declare that

1. The research reported in this thesis, except where otherwise indicated, is my original research.
2. This thesis has not been submitted for any degree or examination at any other university.
3. This thesis does not contain other persons' data, pictures, graphs or other information, unless specifically acknowledged as being sources from other persons.
4. This thesis does not contain other persons writing, unless specifically acknowledged as being sources from other researchers. Where other written sources have been quoted, then:
 - a. Their words have been rewritten but the general information attributed to them has been referenced.
 - b. Where their exact words have been used, then their writing has been placed in italics and inside quotation marks, and referenced.
5. This thesis does not contain, text, graphics or tables copied and pasted from the Internet, unless specifically acknowledged, and the source being detailed in the thesis and in the References sections.

Signed:  _____

Peer-reviewed Conference Proceedings

Title of Proceeding	Photonic West
Title of Contribution	Intracavity generation of low-loss radial-order Laguerre-Gaussian modes using digital holograms
Title of Conference	Mode Control and Selection and Beam Characterization and Control II
All Authors in Order of Appearance on Output	T. Bell, A. Forbes, S. Ngcobo, K. Ait-ameur
Status	Published
Year	2016
Author's Contribution	First author and Speaker
City/Country	United State of America, San Francisco

Title of Proceeding	Photonic West
Title of Contribution	Thermal lensing measurement from the coefficient of defocus aberration using Shack-Hartmann wavefront sensor
Title of Conference	Mode Control and Selection and Beam Characterization and Control II
All Authors in Order of Appearance on Output	T. Bell, A. Forbes, S. Ngcobo, D. Naidoo
Status	Published
Year	2016
Author's Contribution	First author and speaker
City/Country	United State of America, San Francisco

Title of Proceeding	Photonic West
Title of Contribution	Discrete excitation of mode pulses using a diode-pumped solid-state digital laser
Title of Conference	Mode Control and Selection and Beam Characterization and Control II
All Authors in Order of Appearance on Output	S. Ngcobo, T. Bell
Status	Published
Year	2016
Author's Contribution	Speaker and 2nd author
City/Country	United State of America, San Francisco

Title of Proceeding	62nd Conference of the South African Institute of Physics
Title of Contribution	Digital laser mode amplification using ND: YAG amplifier
Title of Conference	South African Institute of Physics (MMU & RU)
All Authors in Order of Appearance on Output	T. Bell, S. Ngcobo
Status	Published
Year	2016
Author's Contribution	Speaker
City/Country	South Africa, Cape Town

Title of Proceeding	61st Conference of the South African Institute of Physics
Title of Contribution	Optimization of losses introduced by p -absorbing mask in a Digital Laser
Title of Conference	South African Institute of Physics (MMU & RU)
All Authors in Order of Appearance on Output	T. Bell, S. Ngcobo, A. Forbes
Status	Published
Year	2015
Author's Contribution	Speaker
City/Country	South Africa, Port Elizabeth

Title of Proceeding	61st Conference of the South African Institute of Physics
Title of Contribution	Fundamental Laguerre-Gaussian (LG_{p0}) mode with lower output power threshold
Title of Conference	South African Institute of Physics (MMU & RU)
All Authors in Order of Appearance on Output	T. Bell, S. Ngcobo, A. Forbes
Status	Published
Year	2015
Author's Contribution	Speaker
City/Country	South Africa, Port Elizabeth

Title of Proceeding	61st Conference of the South African Institute of Physics
Title of Contribution	Fundamental Laguerre-Gaussian (LG_{p0}) mode with lower output power threshold
Title of Conference	South African Institute of Physics (MMU & RU)
All Authors in Order of Appearance on Output	T. Bell, S. Ngcobo, A. Forbes
Status	Published
Year	2015
Author's Contribution	Speaker
City/Country	South Africa, Port Elizabeth

Title of Proceeding	Optics + Photonics
Title of Contribution	Low-loss selective excitation of higher-order modes in a diode-pumped solid state digital laser
Title of Conference	Laser Beam Shaping XVI
All Authors in Order of Appearance on Output	S. Ngcobo, T. Bell, K. Ait-Ameur and A. Forbes
Status	Published
Year	2015
Author's Contribution	Co-Author
City/Country	United State of America, San Diego

Title of Proceeding	Optics + Photonics
Title of Contribution	Selective excitation and detection of higher-order doughnut laser modes as an incoherent superposition of two petals modes in a digital laser resonator
Title of Conference	Laser Beam Shaping XVI
All Authors in Order of Appearance on Output	S. Ngcobo, T. Bell, I. Litvin, D. Naidoo, K. Ait-Ameur, and A. Forbes
Status	Published
Year	2015
Author's Contribution	Co-Author
City/Country	United State of America, San Diego

Title of Proceeding	Optical Society of America
Title of Contribution	Generation of Laguerre-Gaussian beams using a diode pumped solid-state digital laser
Title of Conference	Frontier in Optics
All Authors in Order of Appearance on Output	T. Bell, A. Forbes, and T. Ngcobo
Status	Published
Year	2015
Author's Contribution	Speaker and first author
City/Country	United State of America, San Jose

Title of Proceeding	60th Conference of the South African Institute of Physics
Title of Contribution	Thermally induced lensing determination from the coefficient of defocus aberration
Title of Conference	South African institute of Physics (UJ)
All Authors in Order of Appearance on Output	T. Bell, D. Naidoo, and A. Forbes
Status	Published
Year	2014
Author's Contribution	Speaker and first author
City/Country	South Africa, Johannesburg

Peer-reviewed Journal Articles

1. **T Bell**, A Hasnaoui, K Ait-Ameur, S Ngcobo, "Excitation of high-radial-order Laguerre-Gaussian modes in a solid-state laser using lower-loss digitally controlled amplitude mask", *Journal of Optics*, 19(10), **2017**.
2. **T Bell**, S Ngcobo, "Selective Excitation of Higher-radial-order Laguerre-Gaussian Beams Using a Solid-state Digital Laser", *Journal of Lasers, Optics & Photonics* 3 (2), **2017**.

Acknowledgements

- First of all I would like to thank and honour my God, the creator of heaven and earth, who sacrificed his only Son so that I could be welcomed back into His kingdom, for helping me take on and complete this study.
- Next, I would like to express my sincere gratitude towards my PhD supervisor, Dr Sandile Ngcobo of the National Laser Centre of the Council for Scientific and Industrial Research (CSIR). The door to Dr Ngcobo's office was always open whenever I ran into a spot of trouble or had a question about my research. He consistently allowed this work to be my own and steered me in the right direction whenever he thought I needed it.
- In addition to my supervisor, I wish to thank Prof. Andrew Forbes who gave me an opportunity to pursue my PhD at the CSIR. Prof. Forbes and his team (Drs Angela Dudley and Darryl Naidoo) were the first people to introduce me to solid-state lasers and laser beam shaping. I will forever be grateful to them.
- I am greatly indebted to my co-supervisor, Dr Mathew K. Moodley from the University of KwaZulu-Natal's School of Chemistry and Physics, who played a huge role in helping me write up my dissertation and completing it on time. I also wish to thank the technicians (Mr Gary King, Nico Marome and Mr Rocky Ramokolo) at NLC who helped me with laboratory equipment. Without their passionate participation and input, many of the experiments would not have been successfully conducted.

-
- Dr Shashi Prabhakar (NLC PostDoc) at the CSIR acted as peer reviewer of most of my work and I am extremely grateful to him for his invaluable comments. I must furthermore express my profound gratitude to the staff members of the National Laser Centre, the CSIR Optics Student Chapter, my family (Frans, Lindiwe, Musa and Annah Bell), and my close friends and colleagues (Sphume, Lizwe, Monnamme, Nomvula, Ms Myeza, Fakazi, Thandeka, Thuli, Chemist, Prince and Mosima) for providing me with unfailing support and continuous encouragement throughout my years of study – especially throughout the process of researching and writing this dissertation. This accomplishment would not have been possible without them. Thank you all.
 - Finally, I am grateful to the Department of Science and Technology and the National Research Foundation of the Republic of South Africa for having granted me financial assistance via the DST-NRF Professional Development Programme Fund to complete this PhD study.

Abstract

Recently a laser with an intracavity spatial light modulator (SLM) was demonstrated and showed in principle the creation of novel laser modes. The digital holograms written to the SLM altered the resonant mode of the cavity through amplitude and phase control, and thus the term “digital laser” was born. The technology holds much promise but requires further detailed study to fully realise its potential.

In this dissertation, we revisit the digital laser with the aim of enhancing its performance. We extend the digital laser to faster switching, higher energies, and diverse wavelengths. In the process, we study the impact of these advances on mode purity and laser performance. None of these developments have so far been reported in the literature, due to the complexity of the experiments and the novelty of the device. We hope the result will lead to a new understanding of such devices and therefore constitute an original contribution to the field of research. This work outline a roadmap for the development of a robust prototype device that may find many applications, for example, in laser additive manufacturing.

In Chapter 2, we experimentally demonstrate the measurement of thermally induced lensing, using a Shack-Hartmann wavefront sensor (SHWFS). The thermally induced lens from the coefficient of defocus aberration using a SHWFS is measured. As a calibration technique, we infer the focal length of standard lenses probed by a collimated Gaussian beam of wavelength 633 nm. The technique is applied to an Nd: YAG crystal that is actively pumped by a diode laser operating at 808 nm. The results were compared to the results obtained by changing the properties of the end-pumped solid-state laser resonator operating at 1064 nm, where the length

of an unstable plane-parallel laser resonator cavity was varied, and the laser output power was measured.

In Chapter 3, we focus on the generation of Laguerre-Gaussian modes using an end-pumped solid-state laser that has an ability to control the output laser modes. The solid-state digital laser is used in the generation of Laguerre-Gaussian modes, $LG_{p,l}$, with radial order $p = 0$ and azimuthal order $l = 0$ to $l = 5$ with a step of 1. We further use the digital laser to generate high-radial-order Laguerre-Gaussian, $LG_{p,0}$ modes by loading digital holograms on a phase-only spatial light modulator that acts as an end mirror of a diode-end-pumped laser resonator. The digital holograms were encoded with an amplitude ring mask, which contained absorption rings that match the p -zeros of the Laguerre polynomial. We demonstrate the generation of high-quality $LG_{p,0}$ modes with a mode volume that was directly proportional to the mode order, p .

In Chapter 4, we experimentally demonstrate selective excitation of high-radial-order $LG_{p,0}$ modes with radial-order, $p = 1 - 4$ and azimuthal-order, $l = 0$, using a diode-pump solid-state laser (DPSSL) that is digitally controlled using an SLM. We encoded amplitude mask containing p -absorbing rings, of various incompleteness (segmented), on grey-scale computer generated digital holograms (CGDH), and displayed them on an SLM, that acted as an end mirror of the diode-pumped solid-state digital laser (DPSSDL). The various incomplete (α) p -absorbing rings were digitally encoded to match the zero intensity nulls of the desired $LG_{p,0}$ mode. We illustrate that the creation of LG_p , for $p = 1$ to $p = 4$, only requires an incomplete circular p -absorbing ring that have a completeness of $\approx 37.5\%$, which makes the DPSSDL resonator to have the lower pump threshold power, while maintaining the same laser characteristics (such as beam propagation properties).

In Chapter 5, we efficiently generate on-demand laser modes using a single-mode solid-state digital laser. The Laguerre-Gaussian mode of azimuthal order $l=(0, 1, 2)$ with zero radial order ($p = 0$) was generated and discretely pulsed using a digital hologram that acts as a "Q-Switch".

Pulses of duration ≈ 200 ms and intensities as high as ≈ 1 mW, with repetition speed of 60 Hz, were produced at $1 \mu\text{m}$. The maximum peak power conversion efficiency measured is $\approx 1.3\%$.

In Chapter 6, we demonstrate the laser output power amplification of the higher-order $\text{LG}_{p,l}$ modes generated from a digital laser by using an extra-cavity Nd: YAG amplifier. The DPSSDL generates fundamental higher-order modes by encoding and displaying a digital hologram on a phase-only SLM that acts as an end mirror of the laser resonator cavity. The amplifier was designed in such a manner that when the $\text{LG}_{p,l}$ modes passed through the Nd: YAG amplifier, they would experience higher gain, which would increase the power of the mode when it is transmitted through the amplifier. Amplification of as high as 42% was realised for $\text{LG}_{2,0}$, and only 9% was realised for $\text{LG}_{2,2}$ due to pump mismatch.

Finally, in Chapter 7, we experimentally generated higher-order modes using DPSSDL operating at 532 nm (visible). A nonlinear crystal (Potassium titanyl phosphate-KTP) which is used for frequency conversion, is inserted inside the DPSSDL operating at 1064 nm (Near-IR). The KTP is pumped using the higher-order modes generated by the 1064 nm solid-state digital laser. We generated intra-cavity $\text{LG}_{p,l}$ modes and Hermite-Gaussian (HG) modes. The laser modes were characterised by analysing the intensity distribution profiles of the beams.

Contents

List of Figures	i
List of Tables	v
1 Introduction to solid-state lasers	1
1.1 Background	1
1.2 Basic optics and mode selection	4
1.2.1 The wave equation	4
1.2.2 Gaussian and higher-order beams	7
1.3 Resonator configuration	14
1.4 Introduction to the Digital Laser	19
2 Thermal aberrations in Nd: YAG crystal	22
2.1 Introduction	22
2.2 Defocus aberration	23
2.3 Calibration experiment	24
2.4 Testing known lenses	25
2.5 Thermally induced lensing in Nd: YAG crystal	29
2.6 Summary	31
3 Generation of Laguerre-Gaussian modes	32
3.1 Generation of petal-like Laguerre-Gaussian beams	32
3.1.1 Introduction	32
3.1.2 Experimental methodology and concept	33
3.1.3 Results and discussion	34
3.1.4 Summary	34
3.2 Generation of radial order Laguerre-Gaussian beams using a solid-state digital laser	35

3.2.1	Introduction	35
3.2.2	Radial Laguerre-Gaussian modes	36
3.2.3	Experimental methodology and concept	37
3.2.4	PC run numerical simulations	38
3.2.5	Results and discussion	40
3.2.6	Summary	44
4	Radial Laguerre-Gaussian mode generation using incomplete amplitude mask	45
4.1	Introduction	45
4.2	Radial-order Laguerre-Gaussian modes	47
4.3	Experimental methodology and concept	47
4.4	A PC run numerical simulations for incomplete ring	47
4.5	Results and discussion	51
4.6	Summary	56
5	Discrete excitation of mode pulses using a diode-pumped solid-state digital laser	58
5.1	Introduction	58
5.2	Q-switching using a spatial light modulator	59
5.3	Methodology	60
5.4	Results and discussion	61
5.5	Summary	64
6	Solid-state digital laser mode amplification using extra-cavity Nd: YAG amplifier	65
6.1	Introduction	65
6.2	Experimental setup and methodology	66
6.3	Results and discussion	66
6.4	Summary	67
7	Intracavity second harmonic generation for higher-order modes	72
7.1	Introduction	72
7.2	The second harmonic generation from 1064 nm to 532 nm	73
7.3	Experimental methodology and concept	77
7.4	Results and discussions	78
7.5	Summary	82
8	Conclusion remarks and future perspective	86

Bibliography	89
Appendix A Crystal Materials	98
A.1 Nd:YAG Crystal	98
A.2 KTP Crystals	98

List of Figures

- 1.1 End-pumping gain medium using diode laser. 3
- 1.2 Plane wave propagating in z-direction with red squares representing the electric field component, while the green squares represent the magnetic field. 8
- 1.3 Gaussian beam propagation in z-direction. 10
- 1.4 The Gaussian transverse amplitude profile. 11
- 1.5 Intensity distribution profiles. 13
- 1.6 Basic geometry of a laser cavity, with end-mirror and output coupler mirror having a reflectivity of 100% and $\pm 90\%$ respectively. 15
- 1.7 Different geometries of optical laser resonators. 17
- 1.7 Different geometries of optical laser resonators. 18
- 1.7 Different geometries of stable optical laser resonators. 19
- 1.8 Resonator cavity with a digital end mirror that is computer controlled. 21

- 2.1 Defocus phase variation (a) 2D and (b) 3D. 24
- 2.2 Experimental Setup for calibration. 24
- 2.3 CLAS-2D software snapshot varying the beam size from 20% (a) to 100% (b). The CLAS-2D software allowed one to draw an analysis Zernike circle over the Gaussian beam and then computes the Zernike coefficients. In addition, the Zernike coefficients are used to calculate the radius of curvature. 26
- 2.4 The graph of defocus coefficient versus the ratio of Zernike radius (a) over the Gaussian beam radius (w) to determine the lowest defocus coefficient with regard to the ratio. 27
- 2.5 (a) Measured focal lengths f_m against the nominal focal lengths f_n . (b) Measured focal length for nominal focal length of $f = 250$ mm as the ratio of radius to beam size increases. 28

2.6	The Nd: YAG gain medium pumped by a single-mode diode laser operating with a Gaussian beam at 808 nm (the intensity distribution of the focus pump at the centre of the crystal is also shown).	29
2.7	Power transmitted against the input pump power to determine the gain saturation. This graph is used to determine if the gain medium is still in good condition and lasing can still occur. In addition, this graph indicates that the gain medium is not damaged, and lasing will start at 17 Amps.	30
2.8	Unstable plane-parallel laser resonator used to determine thermally induced lensing.	30
2.9	The effective focal length of the thermally induced lens as a function of the optical pump power, for two measurement techniques used.	31
3.1	Schematic representation of DPSSDL, with the laser mode exiting the laser cavity comprising SLM and M_2 . Diode laser (pump) operating at 808 nm is shown in yellow, while the exciting (1064 nm) beam at the output coupler (M_2) is shown in red.	33
3.2	Computer-generated hologram (CGH) encoded to the SLM for the generation of $LG_{p,l}$ modes of order $p = 0$ & $l = 0 - 5$	34
3.3	Observed intensity profile for $LG_{p,l}$ modes of order $p = 0$ & $l = 0 - 5$, at the output coupler (M_2 on Fig. 3.1).	34
3.4	Schematic representation of the DPSSDL, with the laser mode exiting the at the output coupler mirror (M_3). Diode laser operating at 808 nm is shown in red, while the excited beam is shown in blue.	37
3.5	Intensity cross-section of numerically simulated lowest-loss eigenmodes for $p=1$ to 3, when a mask containing an absorbing p ring is inserted inside the resonator. The mask is inserted in such that the high-loss absorbing ring coincides with the intensity p -zero nulls. For an example, we looked at $p = 3$ Laguerre-Gaussian mode.	39
3.6	(a) Gray-scale (0 to 2π) holograms with amplitude modulation in the form of a checkerbox. (b) Observed intensity profiles (normalised to 1) of the Laguerre-Gaussian modes of order $p = 0 - 4$ at the output coupler. (c) Beam width at the output coupler as a function of mode order, with theoretical (Eq. 3.2) results represented by a solid red line.	41

3.7	(a) Beam propagation factor as a function of mode order, with theoretical (Eq. 3.3) results represented by a solid line. (b) The plot of modal decomposition results with intensity normalised to 1, for $p = 0 - 4$	42
3.8	(a) Power extraction (output power) for $p = 0$ and $p = 4$, as the function of the diode pump power (input power). (b) Slope efficiency (η) and pump threshold as a function of mode order.	43
4.1	Schematic diagram illustrating a 50% complete p -absorbing ring, regardless of the symmetry.	48
4.2	(a) Numerically simulated fundamental mode shape at the far-field. (b) Numerically simulated propagation factor M^2 as a function of truncation ratio $Y_c = r_0/w$ (r_0 is the aperture radius, while w is the beam width).	49
4.3	(a) Numerically simulated intra-cavity losses (δ) of the fundamental mode as the function of the beam truncation ration (Y_C). (b) Numerically simulated intra-cavity losses (δ) of the fundamental mode as the function of ring incompleteness (α).	50
4.4	Top row of (a)-(d) shows computer-generated digital holograms encoded as pixelated gray-scale images where the completeness of the p absorbing ring varies from 12.5% to 100% for $p = 1 - 4$. Bottom row of (a)-(d) shows the generated intensity profiles from the laser for the different corresponding p -absorbing ring digital holograms.	52
4.5	(a) Beam propagation factor, M_p^2 , and (b) beam radius, w_p , at the output coupler for LG modes of $p = 1 - 4$ with varying completeness of the absorbing rings.	53
4.6	The figure shows the slope efficiency, (a) η_p , and the pump power threshold, (b) ϵ_p , for LG $_p$ modes of $p = 1 - 4$ with varying completeness of the absorbing circular ring.	55
5.1	Schematic of the DPSSDL.	61
5.2	(a) Oscilloscope image displaying pulsed voltages for Gaussian mode in 200 ms. (b) Oscilloscope image displaying pulsed and continuous (solid straight line) voltage for Gaussian mode in 200 ms.	62
5.3	(a) Oscilloscope image displaying pulse voltage for on-demand modes in 200 ms, continuously. (b) Oscilloscope image displaying pulse voltage for on-demand modes in 200 ms, discretely.	63
6.1	Schematic of DPSSDL with a single-pass Nd: YAG amplifier.	67

6.2	Computer-generated holograms (CGH) encoded as pixelated gray-scale for generating $LG_{p,l}$. Rows represent $p=0$ to 2, and columns represent $l=0$ to 2.	68
6.3	(a) Observed intensity profiles of the seeded beams focused on the external Nd: YAG laser crystal. (b) Observed intensity profile of the amplified beams. Intensity profiles were recorded using a CCD camera; rows represent LG modes of order $p=0$ to 2, and columns represent LG modes of order $l=0$ to 2.	69
6.4	(a) The graph of the slope efficiency versus pump power to determine the pump power (shown by red rectangle) that should be used for amplification. (b) The graph of the slope efficiency graph versus the mode order p, l amplified using a 60 W pump power.	70
6.5	(a) The graph of the $LG_{p,l}$ beam width versus the mode order p, l . (b) The graph showing the amplification percentage against the mode order p, l	71
7.1	Laser resonator model for intra-cavity frequency doubling from 1064 nm to 532 nm.	76
7.2	Schematic of the Nd: YAG crystal digital laser with a nonlinear crystal (KTP) against the output coupler of the resonator.	77
7.3	(a) The observed 2D intensity profiles for $LG_{p,l}$ operating at 1064 nm. (b) The observed 2D intensity profiles $HG_{m,n}$ operating at 1064 nm.	79
7.4	(a) The observed 2D intensity profiles for $LG_{p,l}$ operating at 532 nm at the far-field with pump out of phase with KTP. (b) The observed 2D intensity profiles for $LG_{p,l}$ operating at 532 nm at the near-field with pump out of phase with KTP.	81
7.5	The observed 2D intensity profiles for $HG_{0,n}$ operating at 532 nm at the far-field and near-field with pump out of phase with KTP.	82
7.6	(a) The observed 2D intensity profiles for $LG_{p,l}$ operating at 532 nm with pump in phase with KTP. (b) The observed 2D intensity profiles for $HG_{p,l}$ operating at 532 nm with pump in phase with KTP.	83
7.7	(a) The size (w) of the $LG_{p,l}$ laser beams operating at 1064 nm as the function of mode order at the output coupler. (b) The size (w) of the $HG_{m,n}$ laser beams operating at 1064 nm as the function of mode order at the output coupler.	84
7.8	The size (w) of the $LG_{p,l}$ laser beams operating at 532 nm as the function of mode order at the output coupler. (b) The size (w) of the $HG_{m,n}$ laser beams operating at 532 nm as the function of mode order at the output coupler.	85
A.1	Four energy level diagram for Nd:YAG laser principle of operation.	99

List of Tables

1.1	Pros and cons of different laser resonator designs.	15
3.1	Laguerre polynomials and their roots.	36
7.1	Non-zero nonlinearity coefficient d_{mn} for KTP.	74
A.1	Nd: YAG optical properties.	99
A.2	KTP optical properties.	100

Chapter 1

Introduction to solid-state lasers

Control over laser modes constitutes one of the key tools for having almost full control of the laser. We investigated digitally controlled modes by using digital lasers that were recently discovered by scientists at the Council for Scientific and Industrial Research (CSIR) in the Republic of South Africa.

This introductory chapter will include the literature review and supporting theories, and it will cover the following information:

1. Background.
2. The core research problem and its significance.
3. A comprehensive overview of the relevant literature leading to clearly defined knowledge gaps.
4. A coherent problem statement highlighting the nature and magnitude of the problem, the discrepancies and knowledge gaps therein, and possible factors influencing the problem.
5. The structure and layout of the dissertation.

1.1 Background

All the work that has been done thus far on lasers and mode selections in lasers was due to the discovery of Maxwell's equations in 1861 [1]. Professor James Clerk Maxwell was a Scottish physicist who foretold the existence of electromagnetic waves with a vast range of wavelengths. Maxwell's equations are a set of partial differential equations that, together with the Lorentz force law, form the foundation of classical electrodynamics, and of classical optics

[2]. In the current study, the focus is more on the classical electromagnetic fields formulated from Maxwell's equation. In particular, Section 2 will emphasise the electromagnetic field for different laser modes that can be expressed.

The first laser, built in 1960 by Theodore H. Maiman at Hughes Research Laboratories, was based on theoretical work by Charles Hard Townes and Arthur Leonard Schawlow. The original maser principle is currently used in a vast diversity of devices operative in countless parts of the electromagnetic spectrum [3]. Laser devices employ extraordinary optical pumping methods that utilise a gain medium of different materials and resonator design approaches. Lasers have an ability to perform a wide range of functions due to high powers, short wavelengths, ultrashort pulses, and mode selections [4, 5, 6, 7, 8, 9].

The word "Laser" is an acronym that stands for "Light Amplification by Stimulated Emission of Radiation", which was coined in 1957 by the American physicist Gordon Gould who is widely known for the invention of the laser. While the original meaning of the laser means a principle of operation process. A typical laser comprises of laser cavity in which the light can "bounce" between two or more mirrors. A gain medium (such as laser crystal) is placed within the cavity, which serves to amplify the power of light. The gain medium typically requires an external source of energy, thus it is pumped using some electrical current or external light source [10] as shown in Fig. 1.1. Some portion of the light power circulating in the cavity is transmitted by an output coupler mirror (M_2), causing the transmitted beam to constitute the advantageous output of the laser. Furthermore, it must also be noted that lasers can be operated in a continuous wave or generate pulses. In addition, the shape of the output beam can be controlled outside or inside the laser cavity.

A flash lamp optical pump was initially used for high-powered solid-state lasers. In recent years, diode lasers have become a pumping source, due to the fact that diode lasers provide a highly compact design, better frequency stability, and higher efficiency [11, 12]. This diode pump was first illustrated by Keyes et al. in 1964 [13] who proposed that the GaAs diode lasers were best because they possess robust absorption in the emission bands of GaAlAs, GaAsP, and GaAs. Nd: YAG lasers were very popular long before the paper by Keyes et al., the interest in using Nd: YAG gain medium was high. The Nd: YAG gain medium has good properties, in particular for high-power solid-state lasers and Q-switched lasers emitting at $1 \mu\text{m}$.

Nd: YAG gain medium is generally used in a monocrystalline form, fabricated via the Czochralski growth method. However, polycrystalline Nd: YAG is also available in high quality and in large sizes [14]. In both of these types of Nd: YAG (monocrystalline and polycrystalline), absorption and scattering losses within the length of a laser crystal are normally negligible. Classically, neodymium doping concentration levels are in the order of 1.1 at.%. For high

doping concentrations, pump level and absorption length can be reduced. However, too high concentrations result in quenching of the upper-state lifetime. In addition, the density of dissipated power can become too high in high-power solid-state lasers. Table. A.1 shows the properties of Nd: YAG and necessary optical property values (see Appx. A).

A laser in its simplest form consists of a gain medium that is within a resonator. The diode laser is preferred for pumping solid-state mediums. To produce laser emissions, the gain medium must be excited. End-pumping is realised by guiding the excitation energy along the gain medium, after which laser emission is transmitted through the output coupler mirror (M_2) (see Fig. 1.1). The arrangement in Fig. 1.1 represents an end-pumped laser resonator. The gain medium is excited longitudinally by pumping it at the end face, and a lens focuses the pump beam to the centre of the gain medium. This type of end-pumped optical resonator

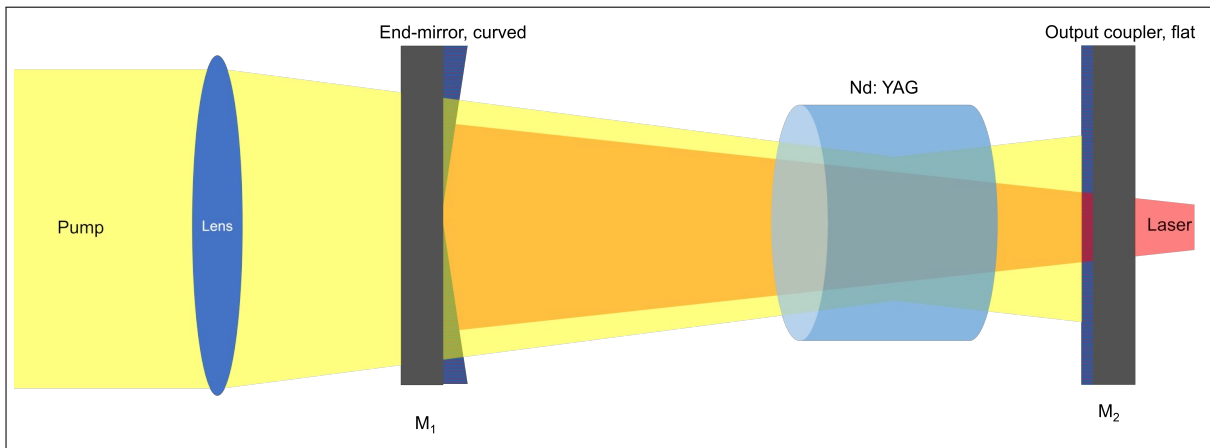


Figure 1.1 End-pumping gain medium using diode laser.

typically allows Gaussian mode selection. However, higher-order modes can be attained by increasing the pump power and using beam-shaping techniques inside the optical resonator. In this dissertation, we generate on-demand modes by replacing the end-mirror with a spatial light modulator (SLM).

Furthermore, in high-power solid-state lasers, the gain medium absorbs the pump energy, which results in end-face bulging, thus creating a thermally induced lensing effect that can be described by the coefficient of defocus aberration. This effect changes the optical path length, thus altering the properties of the selected mode at the output of the laser. With the digital laser, this effect can be reduced drastically by correctly choosing the curvature of the end digital mirror. Chapter 2 focuses on calculating a defocus aberration on Nd: YAG, for better design of the optical cavity.

The next section introduces the basic optics that one uses to study the behaviours and properties of the laser. It also describes the behaviour of visible, ultraviolet, and infrared light, as well as mode selection inside the laser resonator.

1.2 Basic optics and mode selection

This section deals with the basic theories associated with wave equation and discusses how a Gaussian beam propagates within the laser resonator, as well as how the selection of higher-order laser modes can be determined or achieved.

1.2.1 The wave equation

It is well known that all electromagnetic phenomena can be derived using Maxwell's equations. For a charge-free homogeneous isotropic dielectric, Maxwell's equations can be written as follows:

$$\nabla \cdot \mathbf{E} = 0 \quad (\text{Gauss's law}), \quad (1.1)$$

$$\nabla \cdot \mathbf{B} = 0 \quad (\text{Gauss's law for magnetism}), \quad (1.2)$$

$$\nabla \times \mathbf{E} = -\mu \frac{\partial \mathbf{B}}{\partial t} \quad (\text{Faraday's law}), \text{ and} \quad (1.3)$$

$$\nabla \times \mathbf{B} = \varepsilon \frac{\partial \mathbf{E}}{\partial t} \quad (\text{Ampere's law}), \quad (1.4)$$

where ε and μ represent the dielectric permittivity and magnetic permeability of the medium, and \mathbf{E} and \mathbf{B} represent the electric field and magnetic field respectively. If we take the curl of Eq. (1.3), we obtain

$$\begin{aligned} \nabla \times (\nabla \times \mathbf{E}) &= -\mu \frac{\partial}{\partial t} (\nabla \times \mathbf{B}) \\ &= -\varepsilon \mu \frac{\partial^2 \mathbf{E}}{\partial t^2}. \end{aligned} \quad (1.5)$$

The operator $\nabla^2 \mathbf{E}$ is now defined by the following equation:

$$\nabla^2 \mathbf{E} \equiv \text{grad}(\nabla \cdot \mathbf{E}) - \nabla \times (\nabla \times \mathbf{E}). \quad (1.6)$$

Using Cartesian coordinates, one can easily show that

$$(\nabla^2 \mathbf{E})_x = \frac{\partial^2 E_x}{\partial x^2} + \frac{\partial^2 E_x}{\partial y^2} + \frac{\partial^2 E_x}{\partial z^2} \quad (1.7)$$

$$= \nabla \cdot (\text{grad } E_x), \quad (1.8)$$

a Cartesian component of $\nabla^2 \mathbf{E}$ is the div grad of the Cartesian component. Thus, the following equation can be used:

$$\nabla \times (\nabla \times \mathbf{E}) = \nabla(\nabla \cdot \mathbf{E}) - \nabla^2 \mathbf{E}, \quad (1.9)$$

and we can now obtain

$$\nabla(\nabla \cdot \mathbf{E}) - \nabla^2 \mathbf{E} = -\epsilon\mu \frac{\partial^2 \mathbf{E}}{\partial t^2}, \quad (1.10)$$

or

$$\nabla^2 \mathbf{E} = -\epsilon\mu \frac{\partial^2 \mathbf{E}}{\partial t^2}. \quad (1.11)$$

Note that we used Eq. (1.1). Equation (1.11) is formally known as the three-dimensional wave equation and each Cartesian component of electric field \mathbf{E} satisfies the scalar wave equation:

$$\nabla^2 \psi = \epsilon\mu \frac{\partial^2 \psi}{\partial t^2}. \quad (1.12)$$

We can derive the wave equation that satisfied for the magnetic fields as:

$$\nabla^2 \mathbf{B} = \epsilon\mu \frac{\partial^2 \mathbf{B}}{\partial t^2}, \quad (1.13)$$

for a plane wave propagating in the \mathbf{k} direction, the electric and magnetic fields can be rewritten in form

$$\mathbf{E} = \mathbf{E}_0 e^{i(\omega t - \mathbf{k} \cdot \mathbf{r})}, \quad (1.14)$$

and

$$\mathbf{B} = \mathbf{B}_0 e^{i(\omega t - \mathbf{k} \cdot \mathbf{r})}, \quad (1.15)$$

where \mathbf{E}_0 and \mathbf{B}_0 are space and time independent vectors. We can substitute Eq. (1.14) in Eq. (1.11) and obtain the following equation:

$$\frac{\omega^2}{k^2} = \frac{1}{\epsilon \cdot \mu}, \quad (1.16)$$

where

$$k^2 = k_x^2 + k_y^2 + k_z^2. \quad (1.17)$$

Thus the velocity of the propagating wave, v , is given by

$$\begin{aligned} v &= \frac{\omega}{k} \\ &= \frac{1}{\sqrt{\epsilon \mu}} \\ &= 2.998 \times 10^8 m.s^{-1}, \end{aligned} \quad (1.18)$$

which is the speed of light, c , in free space. In a medium of density, the velocity of the propagating wave is

$$v = \frac{c}{n}, \quad (1.19)$$

where

$$n = \sqrt{\frac{\epsilon}{\epsilon_0}} \quad (1.20)$$

is known as the refractive index of the medium. If we substitute Eq. (1.14) into Eq. (1.2), we get

$$i [k_x E_{0x} + k_y E_{0y} + k_z E_{0z}] e^{i(\omega t - \mathbf{k} \cdot \mathbf{r})} = 0. \quad (1.21)$$

This suggests that

$$\mathbf{k} \cdot \mathbf{E} = 0 \quad \text{and} \quad (1.22)$$

$$\mathbf{k} \cdot \mathbf{B} = 0. \quad (1.23)$$

These two equations suggest that \mathbf{E} and \mathbf{B} are perpendicular to \mathbf{k} , thus the waves are transverse in nature. Furthermore, if we substitute the plane wave solutions (Eq. 1.14 and Eq. 1.15) in Eq.

1.3 and Eq. 1.4 respectively, we obtain

$$\mathbf{E} = \frac{k \times \mathbf{B}}{\omega \mu} \quad \text{and} \quad (1.24)$$

$$\mathbf{B} = \frac{k \times \mathbf{E}}{\omega \mu}. \quad (1.25)$$

Since \mathbf{E} , \mathbf{B} and \mathbf{k} are all at a right angle to each other, Eq. (1.24 and 1.25) will give

$$\mathbf{E}_0 = \eta \mathbf{B}_0 \quad \text{and} \quad (1.26)$$

$$\mathbf{B}_0 = \eta \mathbf{E}_0, \quad (1.27)$$

where η is known as impedance of free space. The energy density related to a propagating electromagnetic wave is given by:

$$\langle u \rangle = \frac{1}{2} \epsilon E_0^2 \quad (J \cdot m^{-2} \cdot s^{-1}), \quad (1.28)$$

where E_0 represents the amplitude of the electric field. The intensity (I) of the beam will be given by

$$\begin{aligned} I &= \langle u \rangle v \\ &= \frac{1}{2} \epsilon v E_0^2 \\ &= \frac{1}{2} \sqrt{\frac{\epsilon}{\mu_0}} E_0^2 \quad (J \cdot m^{-2} \cdot s^{-1}). \end{aligned} \quad (1.29)$$

1.2.2 Gaussian and higher-order beams

Gaussian laser modes are a paraxial solution of the scalar Helmholtz equation and are appropriate to define the propagation of coherent laser beams. Nevertheless, the effect of apertures on the laser beam was not considered in this description because apertures would generally interfere with the Gaussian beam. Furthermore, the alteration of laser beams at a lens is only treated in a paraxial sense and aberrations of the lens are not taken into account.

One of the characteristics of a collimated laser beam is that it propagates in a straight line in a homogeneous material. However, due to diffraction properties, the laser beam diverges during the propagation. The divergence of the laser beam might be large or small, depending on the diameter of the beam. The laser beam behaves as a plane wave along the direction of propagation (z -axis) as shown in Fig. 1.2. The amplitude will be a function of the transversal coordinates (x and y) and also a gradually varying function of the propagation distance along the z -axis. Mathematically, this means that the scalar complex amplitude $u(x, y, z)$ of a laser beam

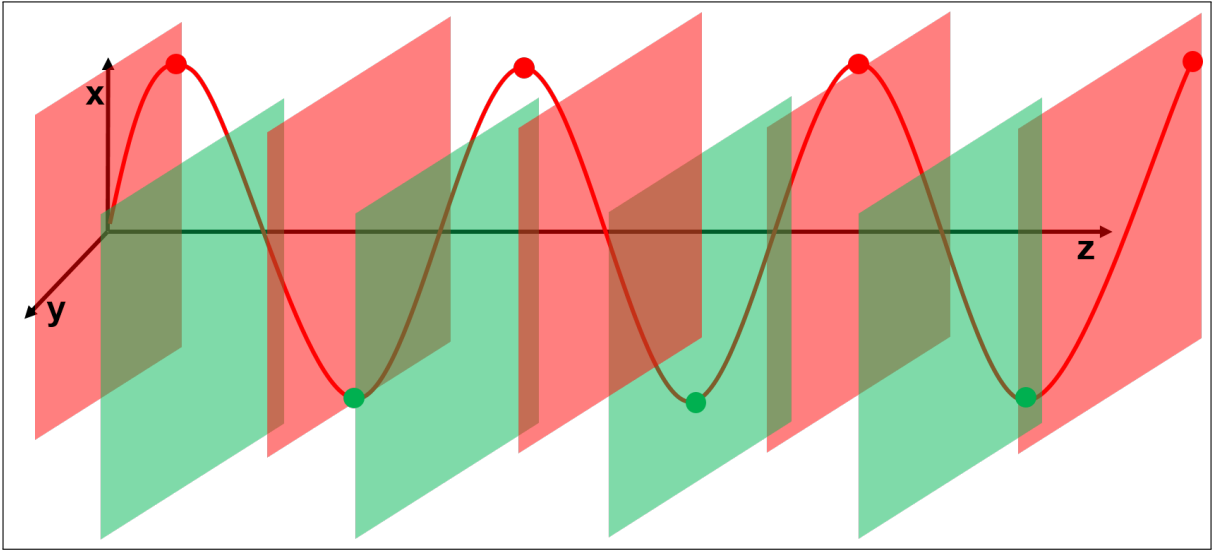


Figure 1.2 Plane wave propagating in z-direction with red squares representing the electric field component, while the green squares represent the magnetic field.

can be described by the product of a complex function $\Psi(x, y, z)$, which changes only slowly along the z-axis, and the complex amplitude of a plane wave propagating in the z-direction ($e^{(ikz)}$),

$$u(x, y, z) = \Psi(x, y, z)e^{ikz}. \quad (1.30)$$

The constant k is again defined as $2\pi n/\lambda$. To simplify the notation, the wavelength $\lambda_n = \lambda/n$, where n is the refractive index of the material used. By using the scalar Helmholtz equation

$$(\nabla^2 + k^2)u(x, y, z) = 0, \quad (1.31)$$

the following equation for u can be obtained:

$$\begin{aligned}
\frac{\partial u}{\partial x} &= \frac{\partial \Psi}{\partial x} e^{ikz} \\
\frac{\partial^2 u}{\partial x^2} &= \frac{\partial^2 \Psi}{\partial x^2} e^{ikz} \\
\frac{\partial u}{\partial z} &= \frac{\partial \Psi}{\partial z} e^{ikz} + k\Psi e^{ikz} \\
\frac{\partial^2 u}{\partial z^2} &= \frac{\partial^2 \Psi}{\partial z^2} e^{ikz} + 2ik \frac{\partial \Psi}{\partial z} e^{ikz} - k^2 \Psi e^{ikz} \\
\therefore (\nabla^2 + k^2)u &= \left(\frac{\partial^2 \Psi}{\partial x^2} + \frac{\partial^2 \Psi}{\partial y^2} \right) e^{ikz} + \frac{\partial^2 \Psi}{\partial z^2} e^{ikz} \\
&\quad + 2ik \frac{\partial \Psi}{\partial z} e^{ikz} = 0.
\end{aligned} \tag{1.32}$$

Agreeing to the assumption that Ψ changes only slowly along the z -direction, the term $\partial^2 \Psi / \partial z^2$ is assumed to be so small that it can be neglected. This will only hold if the relative variation of $\partial \Psi / \partial z$ during the propagation by one wavelength is much smaller than one. Mathematically, this can be explained as follows:

$$\begin{aligned}
\left| \frac{\partial^2 \Psi}{\partial x^2} \right| &\ll \left| 2k \frac{\partial \Psi}{\partial z} \right| \\
&= \frac{4\pi}{\lambda_n} \left| \frac{\partial \Psi}{\partial z} \right| \\
\Rightarrow \left| \frac{\partial \Psi}{\partial z} \right|_{\Delta z = \lambda_n} &\ll 4\pi.
\end{aligned} \tag{1.33}$$

Based on this explanation, the following equation for Ψ is obtained:

$$\left(\frac{\partial^2 \Psi}{\partial x^2} + \frac{\partial^2 \Psi}{\partial y^2} \right) - 2ik \frac{\partial \Psi}{\partial z} = 0. \tag{1.34}$$

This equation is called the paraxial Helmholtz equation. To solve it, we first use an approach for Ψ , which corresponds to a fundamental mode Gaussian beam

$$\Psi(x, y, z) = \Psi_0 e^{i(P(z) + \frac{kr}{2q})} \quad \text{whereby} \quad r^2 = x^2 + y^2, \tag{1.35}$$

with the two complex functions P and q . Ψ_0 is a constant that depends on the amplitude of the Gaussian beam and is determined by the boundary conditions. Equation (1.35) has a comparable form to paraxial spherical wave if we read q as a complex radius of curvature.

Therefore, one can split $1/q$ into a real and an imaginary part as follows:

$$\frac{1}{q(z)} = \frac{1}{R(z)} + \frac{i\lambda}{\pi w^2(z)}. \quad (1.36)$$

The real part is the curvature of the wave and R is the radius of curvature. When we insert the imaginary part of Eq. (1.36) into Eq. (1.35), we can clearly see that the real function w describes the distance r^2 from the z -axis, at which the amplitude decreases to $1/e$ of the maximum value (see Fig. 1.3). Hence, w is called the beam radius. Furthermore, if we let

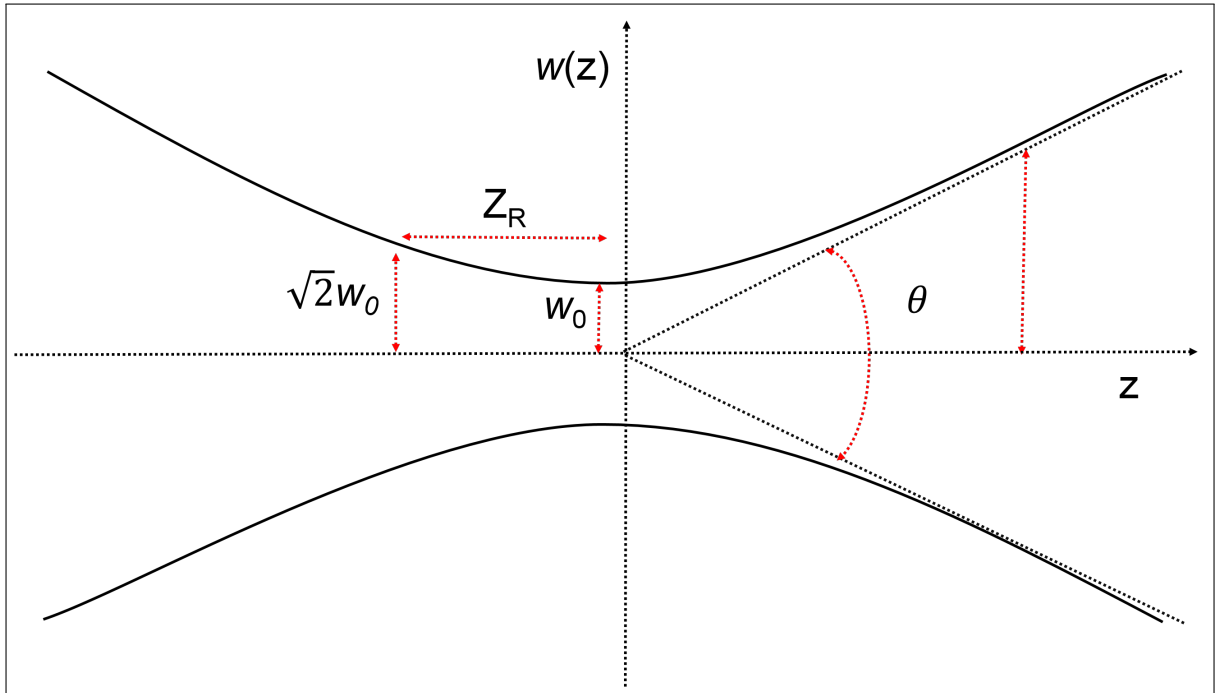


Figure 1.3 Gaussian beam propagation in z -direction.

$z = 0$, the radius of curvature, $R = \infty$. Then the imaginary part of Eq. 1.36 can be simplified as follows:

$$\begin{aligned} \frac{1}{q_0} &= i \frac{\lambda}{\pi w_0^2} \\ \therefore q_0 &= -i \frac{\pi w_0^2}{\lambda}, \end{aligned} \quad (1.37)$$

where w_0 is the propagation constant, called the beam waist. The parameters w and R of a Gaussian beam change during the propagation of the beam along the z -axis as shown in Fig. 1.3.

The solutions of Eq. (1.34) retain a fundamental functional form during propagation. A Gaussian beam is a solution of the paraxial Eq. (1.34) and is appropriate to describe laser beams inside and outside the resonator [15]. The solution is as follows:

$$\Psi(r, z) = \Psi_0 \frac{2}{\pi} \frac{w_0}{w(z)} \times e^{-r^2/w^2(z)} \times e^{-ikr/R(z)} \times e^{-i\phi(z)}. \quad (1.38)$$

The functions $R(z)$, $w(z)$, and $\phi(z)$ are described as follows.

$$w(z) = w_0 \sqrt{1 + \frac{z^2}{z_R^2}}, \quad (1.39)$$

$$R(z) = z \left[1 + \frac{z_R^2}{z^2} \right] \quad \text{and} \quad (1.40)$$

$$\phi(z) = \arctan \left(\frac{z}{z_R} \right), \quad (1.41)$$

where $z_R = \pi w_0^2/\lambda$ is called Rayleigh range. Equation (1.38) is given by the product of an amplitude factor and a transverse Gaussian distribution (shown in Fig. 1.4), a transverse phase factor and longitudinal phase factor respectively. When $z = z_R$, then $w = \sqrt{2}w_0$ so that

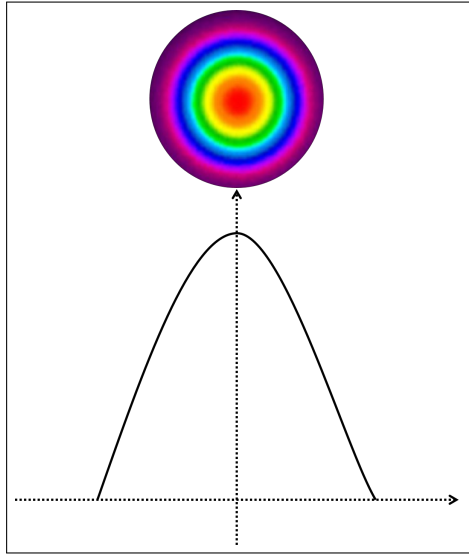


Figure 1.4 The Gaussian transverse amplitude profile.

the Rayleigh range z_R represents the distance from the beam waist at which the beam spot size increases by a factor of $\sqrt{2}$. At large distances, ($z \gg z_R$), w increases linearly with z , according to $w \cong (w_0/z_R)z$. Hence we can define a beam divergence due to diffraction as

$\theta = \lim_{z \rightarrow \infty} (w(z)/z)$ (see Fig. 1.3)

$$\theta_d = \frac{\lambda}{\pi w_0}. \quad (1.42)$$

The fundamental Gaussian beam defined in previous paragraphs can be used to define a general set of eigenfunction solutions of Eq. (1.34), which can be written as the product of a Laguerre polynomial, a Hermite polynomial and a Gaussian function. These are known as Laguerre-Gaussian and Hermite-Gaussian beams, and they assume the following forms respectively:

$$\begin{aligned} U_{p,l}(r,z) &= \sqrt{\frac{2p!}{\pi(p+|l|)!}} \times \frac{1}{w(z)} \left(\frac{\sqrt{2}r}{w(z)} \right)^{|l|} \\ &\times L_p^{|l|} \left(\frac{2r^2}{w(z)^2} \right) \times e^{\frac{-r^2}{w(z)^2} - \frac{ikr^2}{2R(z)}} \times e^{-i(2p+|l|+1)\phi} \\ &\times \arctan\left(\frac{z}{z_R}\right) \times e^{-il\phi}, \end{aligned} \quad (1.43)$$

and

$$\begin{aligned} U_{n,m}(r,z) &= \sqrt{\frac{1}{2^{m+n} \times m!n!}} \times \frac{1}{w(z)} \times H_n \left(\sqrt{\frac{2x}{w(z)}} \right) \\ &\times H_m \left(\sqrt{\frac{2y}{w(z)}} \right) e^{\frac{-r^2}{w(z)^2} - \frac{ikr^2}{2R(z)}} \times e^{-i(m+|n|+1)\phi(z)}. \end{aligned} \quad (1.44)$$

L_p^l is the Laguerre polynomials [16, 17] of order p and l . H_n and H_m are Hermite polynomials [17, 18] of order n and m . The lowest order of both Laguerre-Gaussian (LG) and Hermite-Gaussian (HG) beams is obtained by setting $p = l = 0$ and $n = m = 0$, in Eq. (1.43) and Eq. (1.44) respectively. These solutions are often referred to as TEM_{pl} and TEM_{mn} beams, where TEM stands for transverse electric and magnetic mode, within the paraxial approximation. Both electric and magnetic fields of the EM wave are, in fact, approximately transverse to the z -direction. The examples of the intensity distribution of the TEM_{pl} and TEM_{mn} are shown in Fig. 1.5. TEM_{pl} (see Fig. 1.5a) consists of rings and a central loop for non- l modes, whereas for l modes they adopt the pattern of a petal-like structure. The fundamental laser resonator (Gaussian) mode has the smallest beam radius and divergence in the resonator. The beam radius of each mode increases with increasing mode order number (p, l, m, n) . Due to the complex beam shapes of the TEM_{pl} and TEM_{mn} modes, it is impossible to express the beam size by a 1/e drop in amplitude as is the case for the Gaussian mode. Nevertheless, an impression of the

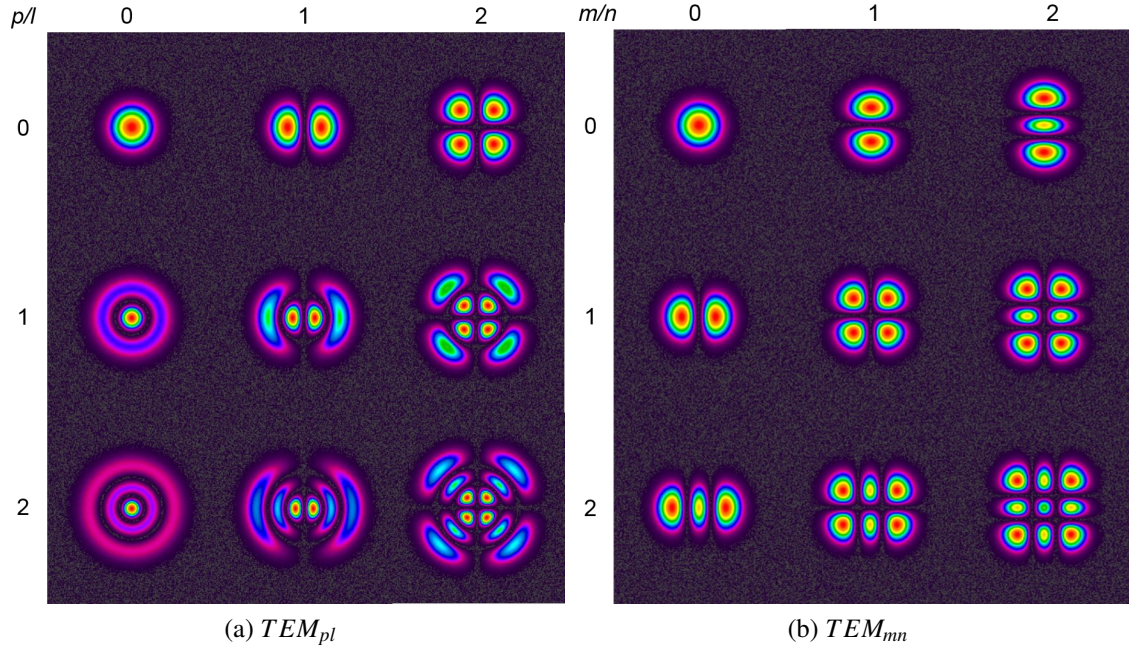


Figure 1.5 Intensity distribution profiles.

association of beam divergence and mode structure can be found if we define the spot size by a circle containing 90% of the energy for cylindrical modes, and, for rectangular modes, by a rectangle having dimensions of double the standard deviation [19]. Thus one can obtain the following equations for TEM modes sizes, depending on the order:

$$w_{pl} = w_0 \sqrt{2p + |l| + 1} \quad (TEM_{pl}), \quad (1.45)$$

$$w_m = w_0 \sqrt{2m + 1} \quad (TEM_{mn} \text{ in x-direction}) \text{ and} \quad (1.46)$$

$$w_n = w_0 \sqrt{2n + 1} \quad (TEM_{mn} \text{ in y-direction}), \quad (1.47)$$

where p, l, m, n and w_0 have been defined already in previous equations. The beam divergence for TEM higher-order mode increases according to Eq. (1.45, 1.46, & 1.47). The increase in beam width and divergence of a multimode beam can be expressed by the following equation:

$$\Theta = M\theta_0 \quad \text{and} \quad (1.48)$$

$$D = MD_0, \quad (1.49)$$

where the multimode beam divergence Θ and the beam diameter D are related to the fundamental mode parameters θ_0 and D_0 by a factor of M . Unfortunately, it is not enough to describe a laser mode by knowing the parameters described by Eq. (1.48) and Eq. (1.49). One of the beam

properties that cannot be altered by any optical system is the brightness (the beam intensity per unit solid angle). The brightness theorem states that the product of beam diameter and far-field angle is constant [20];

$$\theta D = M^2 \theta_0 D_0, \quad (1.50)$$

where M^2 is a dimensionless beam-quality figure of merit and θD is typically expressed as the beam parameter product (mm-mrad). A laser operating in the Gaussian mode is characterised by $M^2 = 1$ [21]. For TEM the mode, the brightness (B) of a laser beam may be defined as:

$$B = \frac{P}{M^4 \lambda^2} \quad (TEM_{pl}) \text{ and} \quad (1.51)$$

$$= \frac{P}{M_x^2 M_y^2 \lambda^2} \quad (TEM_{pl}), \quad (1.52)$$

where P is the output power of the laser mode. It must be noted that M^2 increases as a laser's output power increases, and also as the mode order increases. The beam quality or propagation factor (M^2), for high order modes, is defined as:

$$M^2 = 2p + |l| + 1 \quad (TEM_{pl}), \quad (1.53)$$

$$M_x^2 = 2m + 1 \quad (TEM_{mn} \text{ in x-direction}) \text{ and} \quad (1.54)$$

$$M_y^2 = 2n + 1 \quad (TEM_{mn} \text{ in y-direction}). \quad (1.55)$$

Most high-powered lasers have a “bad” beam quality due to thermal lensing in the laser gain medium.

1.3 Resonator configuration

Several laser resonator designs can be employed when designing a resonator [3, 15, 22, 23, 24], all of which favour or against desired output for application. Thus one need to choose an appropriate design since the design determines the beam radius of the fundamental mode. Table. 1.1 contains a list of designs, with their pros and cons. Although effective resonator design is determined by a thorough understanding of the most significant physical phenomena, that may limit the laser power output and modes. When designing the resonator, it is important to think carefully about the suitable matching of diode laser characteristics and the resonator design. From Table. 1.1, it is clear that if more power is obtained from the laser, the beam quality is affected – mainly by thermal lensing [25, 26, 27, 28].

Table 1.1 Pros and cons of different laser resonator designs.

Resonator design	Pros	Cons
Slab end-pumped	Match mode volume*	Poor beam quality
Slab side-pumped	High pump power Larger volume is excited	Poor beam quality Laser emission is not gain-guided
Rod end-pumped	Efficient	Limited power Thermomechanical damage
Rod side-pumped	High pump power Power amplifiers	Limited beam quality
Disc end-pumped	Small crystal volume	Low thermo-mechanical robustness Multi-pass excitation

*volume of the mode in the active medium.

Typical optical laser resonators are open constructions and consists of optical components, which includes two or more mirrors that are well aligned to allow a beam of light to circulate in a closed loop and produce an optical response to the gain medium. When an optical resonator is combined with the active medium the result is an optical oscillator [15]. For example; the resonator can consist of two parallel mirrors that are aligned; normally these mirrors are called the end-mirror and the output coupler mirror, as shown in Fig. 1.6. Optical resonators serve as a fundamental constituent of lasers. A number of pumped atoms in the excited states experience

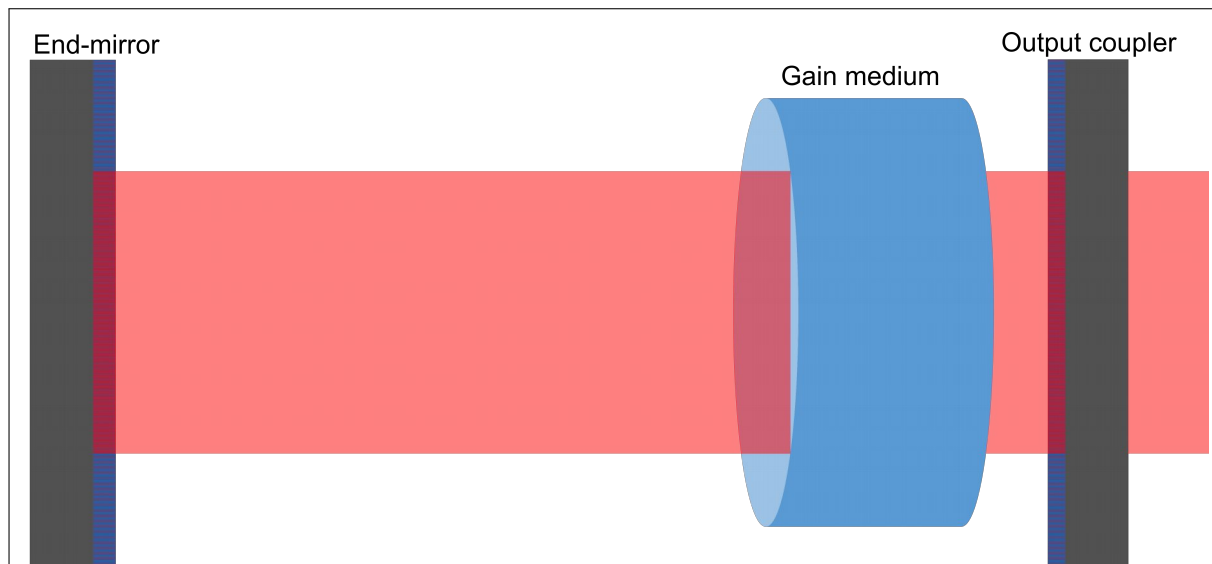


Figure 1.6 Basic geometry of a laser cavity, with end-mirror and output coupler mirror having a reflectivity of 100% and $\pm 90\%$ respectively.

spontaneous emission and get amplified through stimulated emission. Most of the energy gets reflected from both mirrors and passes through the active medium. It continues to be amplified

to a steady-state level of oscillation is reached. After reaching this stage, amplification of the wave within the cavity perishes and additional energy produced by the stimulated emission exits as laser output from the output coupler mirror.

When one has to design an optical laser resonator, different geometries for a stable resonator can be considered. Optical arrangements that are capable of retaining the light movement within the cavity after several transversals are known as stable resonators. Note that it is quite challenging to uphold a flawless collimated beam without a glitch when two flat mirrors are arranged in parallel, which causes major losses in the cavity [15, 29]. These losses may be minimised if appropriate mirrors, such as concave mirrors, are selected. Stable resonator cavities with different mirror combinations are shown in Fig. 1.7. Fig. 1.7(a) shows that one can excite a large fraction of the active medium (mode volume), although it is very difficult to align the mirrors. The confocal resonators are shown in Fig. 1.7(b) are the simplest to be aligned, but a smaller part of the active medium can be utilized.

In general, each and every laser resonator is characterised by a resonator quality factor Q , which is defined by

$$Q = 2\pi \frac{u_s}{u_d}, \quad (1.56)$$

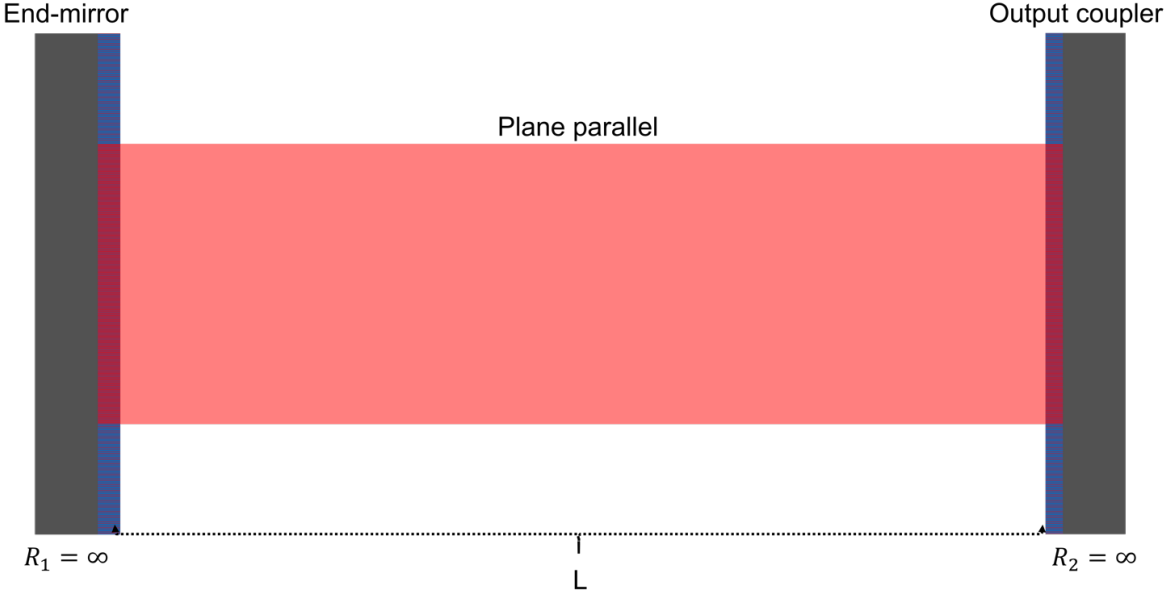
where u_s and u_d are energy stored and energy dissipated per cycle respectively. The Q value of laser resonator lies in the range of $\sim 10^5 - 10^6$ [12]. The resonator that has a low-quality factor Q or that does not maintain a laser beam parallel to its axis, is called an unstable resonator [30]. These resonators have high losses, but they can make efficient use of the mode volume and have an easy way of adjusting the output coupling of the laser.

Stable optical resonators that are shown in Fig. 1.7 consist of two mirrors with radii of curvature R_1 and R_2 , separated by an optical distance $L(nL_0)$; where L_0 is geometrical mirror spacing, and n is the index of refraction of a gain medium. The range of L within which a resonator is stable is determined by the condition in which a ray launched inside the resonator, parallel to the optical axis, remains inside the resonator after an infinite number of bounces (see Fig. 1.7). Each mirror will have a g -parameter, defined as follows:

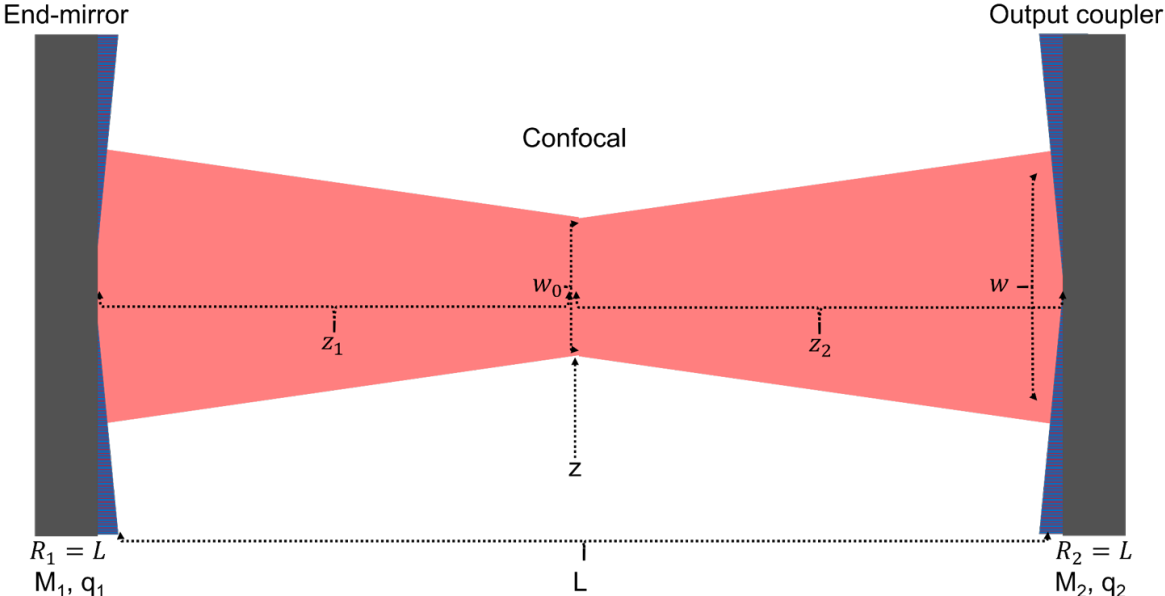
$$g_i = 1 - \frac{L}{R_i}, \quad i = 1, 2 \quad (1.57)$$

for the resonator to be stable, the following condition has to be satisfied:

$$0 < g_i < 1. \quad (1.58)$$

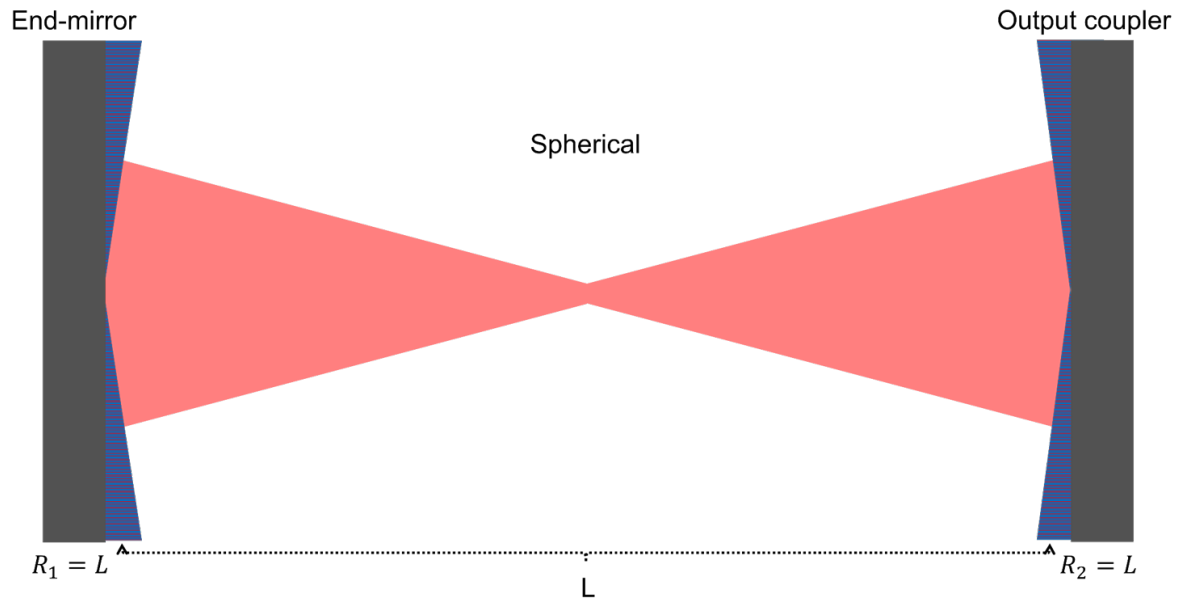


(a) Resonator consists of two plane mirrors set parallel to another.

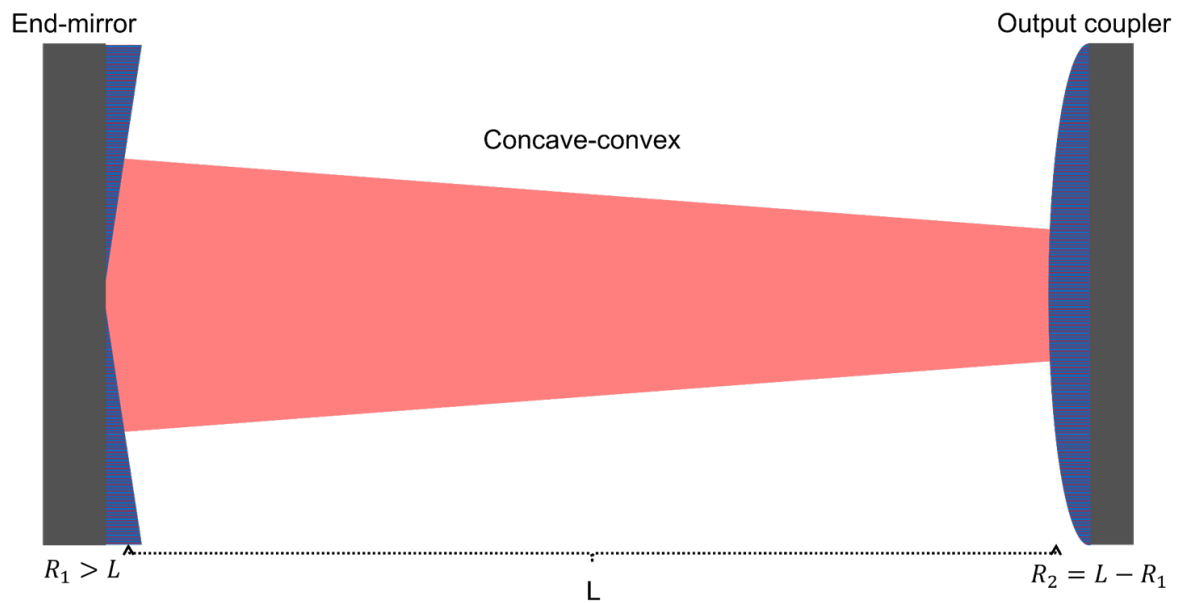


(b) Resonator consist of two spherical mirrors of the same radius of curvature R and separated by a distance L such that the mirror foci are coincident.

Figure 1.7 Different geometries of optical laser resonators.

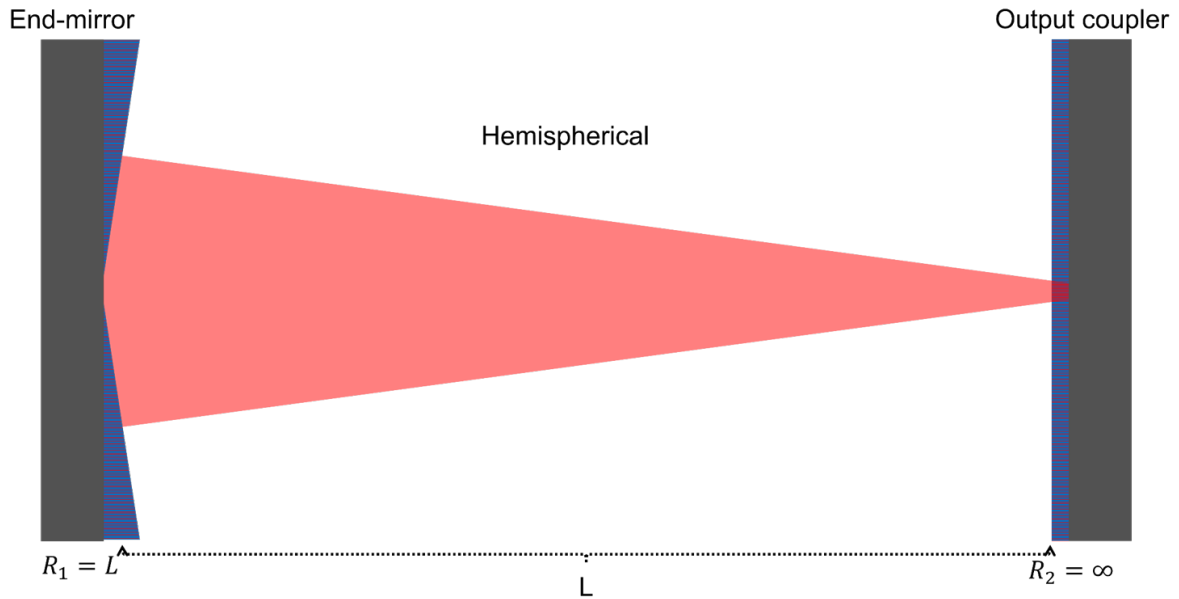


(c) Resonator consist of two spherical mirrors of the same radius R and separated by a distance L such that the mirror centres of curvature are coincident.



(d) Resonator consist of two spherical mirrors of with one mirror having a negative radius R separated by a distance L .

Figure 1.7 Different geometries of optical laser resonators.



(e) Resonator consists of two mirrors with one spherical of radius R and another plane mirror and separated by a distance L such that the beam waist is the smallest on the flat mirror.

Figure 1.7 Different geometries of stable optical laser resonators.

Most stable resonators exhibit a Gaussian beam as the fundamental eigenmode. Furthermore, the radius of curvature is positive for a concave mirror and negative for a convex mirror. The fundamental mode (Gaussian) discussed in Subsection. 1.2.2 has the beam radius as a function of the distance inside the resonator and can be calculated by using the ABCD matrix law [31]. The Gaussian beam radius (w_i) inside the resonator is calculated as follows:

$$w_i^2 = \frac{\lambda L}{\pi} \sqrt{\frac{g_j}{g_i(1 - g_i g_j)}}, \quad ij = 1, 2; \quad i \neq j. \quad (1.59)$$

In addition, the amount of power produced by the laser resonator heavily depends on the volume of the active medium that is occupied by the laser mode. The stored energy can only be extracted from the gain medium by the mode through induced emission.

1.4 Introduction to the Digital Laser

The world's first digital laser was developed at the CSIR and reported by Ngcobo et al. in 2013 [22]. A standard laser consists of two mirrors, a pump and a gain medium. The gain medium changes the frequency of the light to create a laser beam with the perfect characteristics for these different applications. However, in the digital laser, the liquid crystal on silicon (LCOS,

SLM head) acts as one of its mirrors and is fitted at one end of the laser cavity as shown in Fig. 1.8. The LCOS inside the laser can display grey-scale images. When the images change on the LCOS, the properties of the laser beams that exit the device change accordingly. Ngcobo et al. managed to control the size and shape of a laser beam using a computer-generated grey-scale hologram (CGH).

In conventional lasers, the beam is shaped inside the resonator by two mirrors. The curvature of the mirrors determines the size (Eq. 1.59) and shape of the beam. In order to change the shape of a beam inside the laser resonator, one needs to employ different techniques, such as pump shaping, shaping the gain medium, using specialised mirrors, and employing diffractive optical elements (DOE) [32, 33, 34, 35]. However, these methods have proven costly, time-consuming, and the beam shape cannot be replaced or removed.

In this dissertation, we will revisit the digital laser with a view to performance enhancement, mainly in terms of output power, faster switching between modes for pulsing, and frequency conversion. In Chapter 2 we experimentally demonstrate the measurement of thermally induced lensing in Nd: YAG gain medium that is used in the digital laser. Chapter 3 will show the generation of the Laguerre-Gaussian beam using amplitude masks. Chapter 4 demonstrates how to generate the very same modes that we generated in Chapter 3, but using less pump power, while Chapter 5 shows the amplification of these modes using Nd: YAG amplifier. Chapter 6 demonstrates the fast switching of modes continually and by pulsing and in Chapter 7, we will showcase frequency doubling on-demand modes using KTP (The latter is a novel aspect of this work). Finally, we will summarise the findings in Chapter 8, draw pertinent conclusions and discuss possible future work.

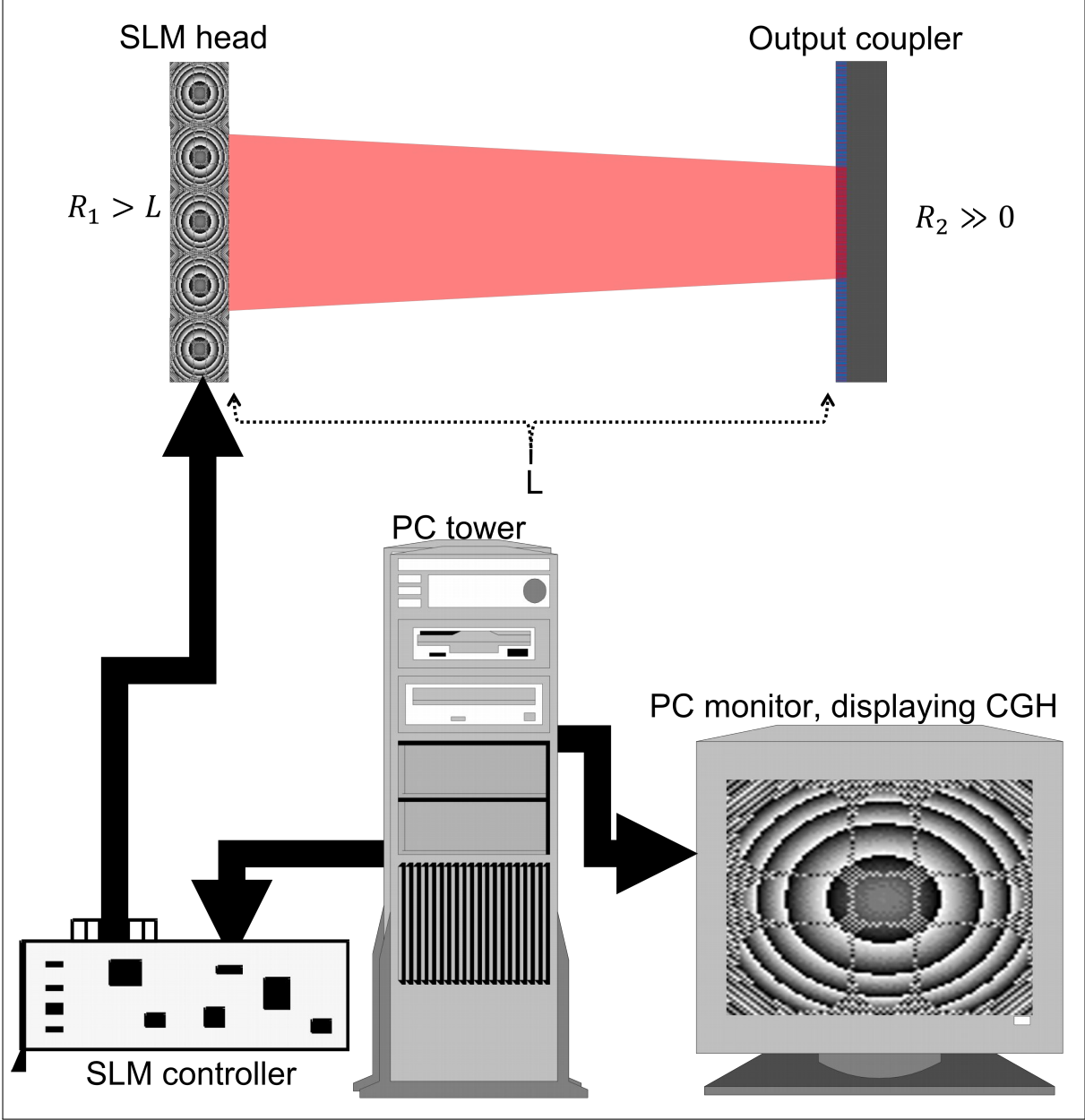


Figure 1.8 Resonator cavity with a digital end mirror that is computer controlled.

Chapter 2

Thermal aberrations in Nd: YAG crystal

In this chapter, we experimentally demonstrate the measurement of thermally induced lensing, using a Shack-Hartmann wavefront sensor (SHWFS). The thermally induced lens was measured from the coefficient of defocus aberration using a SHWFS. As a calibration technique, we infer the focal length of standard lenses probed by a collimated Gaussian beam of wavelength 633 nm. The technique was applied to a Nd: YAG crystal that was actively pumped by a diode laser operating at 808 nm. The results were compared to the results obtained by changing the properties of the end-pumped solid-state laser resonator operating at 1064 nm, where the length of an unstable plane-parallel laser resonator cavity was varied, and the laser output power was measured.

2.1 Introduction

Thermal effects such as thermal aberrations in solid-state lasers have been a subject of interest for over two decades [25, 36, 37]. Solid-state lasers with a wavelength of 1064 nm based on Nd: YAG and Nd: YVO₄ crystals are widely used for marking and micro-structuring processes in the industry [12]. One of the factors that prevent these lasers from reaching maximum potential is the thermal lensing effect, due to a varying thermal gradient [38, 39, 40, 41, 41, 42]. In diode-pumped solid-state lasers, the gain medium (rod-shaped) absorbs the pump energy, resulting in end-face bulging. This creates a thermally induced lensing effect that can be described by the coefficient of defocus aberration [43, 44]. This effect changes the optical path length, thus altering the properties of the selected mode at the output of the laser. The thermal loading of the gain medium such as Nd: YAG crystal causes thermal lensing, and often the crystal starts behaving like a lens [45]. Several methods have been used previously to measure thermal lensing in solid-state laser media [12, 37, 46, 47] – in particular, thermal

lensing behaviour in Nd: YAG [38, 39, 40, 48, 49]. Typically, the radius of curvature of a lens may be described from the coefficient of the defocus aberration, which can be described by a set of orthogonal Zernike polynomials [50].

Defocus aberration can be determined by measuring the change in a phase profile of the probe beam with a wavefront sensing device, such as an interferometer or a wavefront sensor [51]. Calculations of the thermal focal length from the measured defocus will enable one to study the characteristics of the Nd: YAG laser resonator, and thus will provide predictions of the output from solid-state lasers [51]. The defocus coefficient of known lenses was measured using a Shack-Hartmann wavefront sensor (SHWFS) as the calibration technique. We probed a Nd: YAG gain medium with a collimated Gaussian beam operating at 633 nm, and subsequently measured the coefficient of defocus aberration under active pumping at a variety of pump powers. The position of measurement inside the crystal was varied in relation to the end-pumped surface and the resulting focal lengths were compared to typical thermal lens measured data in active end-pumped solid-state lasers.

2.2 Defocus aberration

Since lenses do not produce perfect images, several aberrations are present. Examples are piston, tilt (x-deviation of the light in x-direction and y-deviation of the light in y-direction), defocus, asphericity (due to the increased refraction of light rays when they strike a lens), coma (due to imperfection in the lens), astigmatism (rays that propagate in two perpendicular planes have different focal points), field curvature (uniform brightness), image distortion (loss of image sharpness that can result from spherical lens surfaces).

By definition, defocus is the aberration in which an image is out of focus. Defocus is modelled in a Zernike polynomial format as Eq. 2.1. This corresponds to the parabola-shaped optical path difference between two spherical wavefronts that are tangent at their vertices and have different radii of curvatures [52]. The defocus aberration, $Z_{2,1}$, can be mathematically described as follows:

$$Z_{2,1} = a \times (2r^2 - 1), \quad (2.1)$$

where r is the radial coordinate and a is the Zernike radius. Formally, defocus wavefront aberration results from the image formed by a telescope objective (made using two lenses) being observed not at the location of the Gaussian image point, but at a point longitudinally displaced from it. A modelled solution of Eq. 2.1 is shown in Fig. 2.1, in both two-dimensional and three-dimensional format.

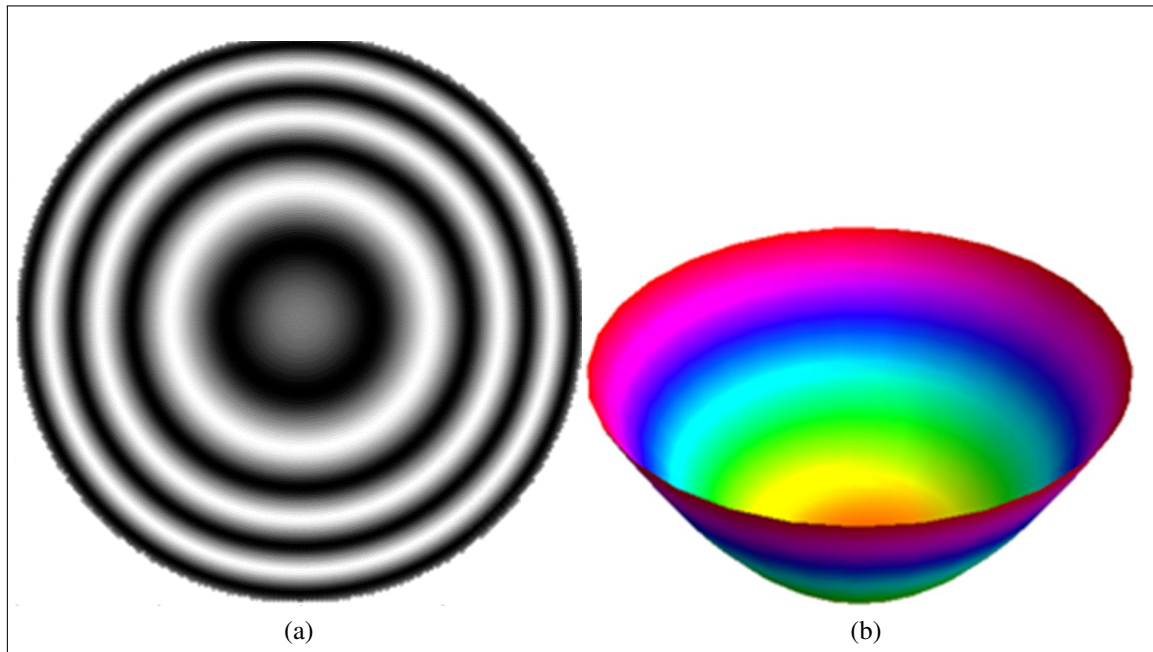


Figure 2.1 Defocus phase variation (a) 2D and (b) 3D.

2.3 Calibration experiment

We developed a calibration technique that was applied to a solid-state gain medium. The wavefront of a helium-neon light source was measured with an SHWFS and the coefficient of defocus aberration was extracted. A Gaussian beam at 633 nm was magnified and collimated with a telescope system made of lenses with focal length of 50 mm and 150 mm. The wavefront was measured at the plane 1 (see Fig. 2.2) and relay imaged with an afocal one to one telescope of lenses with equal focal lengths of 500 mm to plane 2, so as to preserve the wavefront as in Fig. 2.2. At both planes, the ratio of the aperture size over beam size was measured from

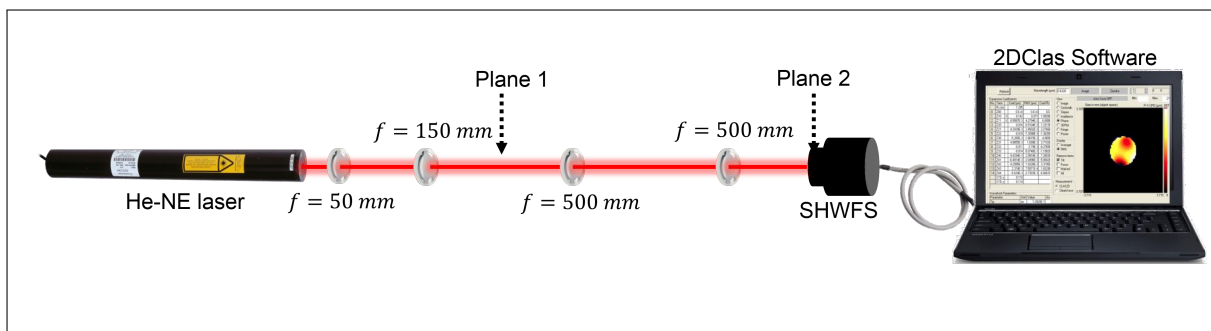


Figure 2.2 Experimental Setup for calibration.

a minimum of 20% to maximum of 100% (see Fig. 2.3). Fig. 2.4 represents a snapshot of

CLAS-2D software (WaveFront Science, Inc), in order to identify where the minimal defocus aberration is experienced. The software is designed to provide thorough and accurate metrology of phase, irradiance, and beam geometry characteristics of laser beams and beams propagating through optical systems. At both planes it is not necessary to capture 100% of the beam size, as only 40% or 60% of the beam already yields a lower defocus coefficient. The results for defocus coefficient at both planes are shown in Fig. 2.4.

2.4 Testing known lenses

A SHWFS was used for measuring the radius of curvature of the incident wavefront with excellent accuracy (real-time wavefront and intensity distribution measurements). In the experiment, we used this device to analyse the focal length of lenses. The radius of curvature R can be calculated based on the wavefront sensor measurement as:

$$R = \frac{-a^2}{4C_{2,1}}, \quad (2.2)$$

where a is the radius of the circle used to calculate the Zernike coefficient, and $C_{2,1}$ is the coefficient for the defocus term. For focal length calculation, $R = f$, Eq. 2.2 can therefore be written as:

$$f = \frac{-a^2}{4C_{2,1}}. \quad (2.3)$$

In determining the focal length of known lenses from the coefficient of defocus aberration, we tested eight known lenses (200, 250, 300, 500, 750 and 1000 mm) that were subsequently positioned at plane 1. The results are shown in Fig. 2.5(a). For a measured focal length of $f= 250$ mm, the results for varying aperture size are illustrated in Fig. 2.5(b). The smallest deviation from the nominal focal length was observed at a ratio of 40% and 60%. This was evident for all nominal lenses used. The system (experimental setup) and manufacturing (of lenses) errors were taken to account when Fig. 2.5b was plotted. System error analysis was conducted by first differentiating Eq. 2.3 with respect to defocus coefficient, and we found the error to be ± 5 mm. According to the manufacturers, the tolerance of the spherical lenses used is 1%.

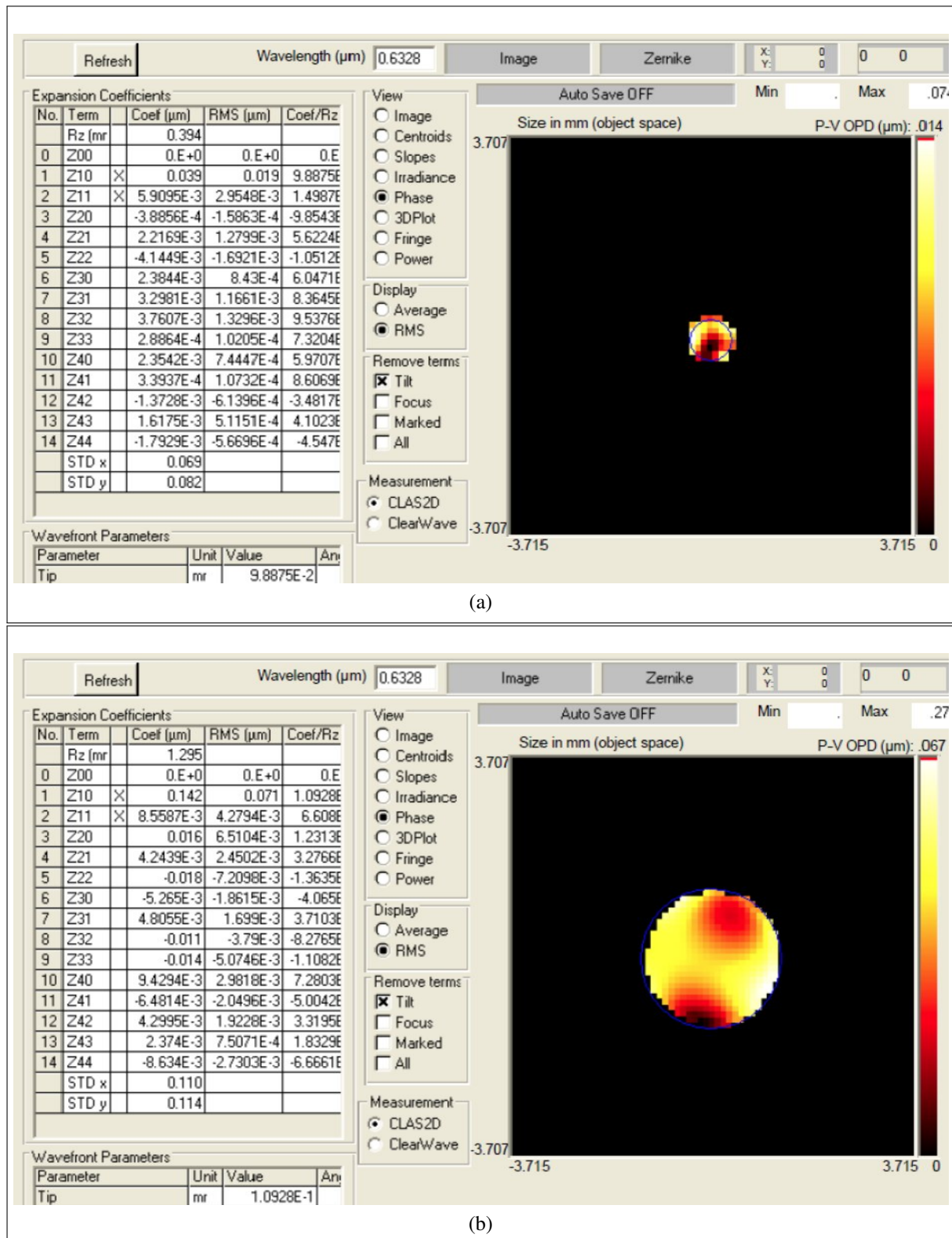


Figure 2.3 CLAS-2D software snapshot varying the beam size from 20% (a) to 100% (b). The CLAS-2D software allowed one to draw an analysis Zernike circle over the Gaussian beam and then computes the Zernike coefficients. In addition, the Zernike coefficients are used to calculate the radius of curvature.

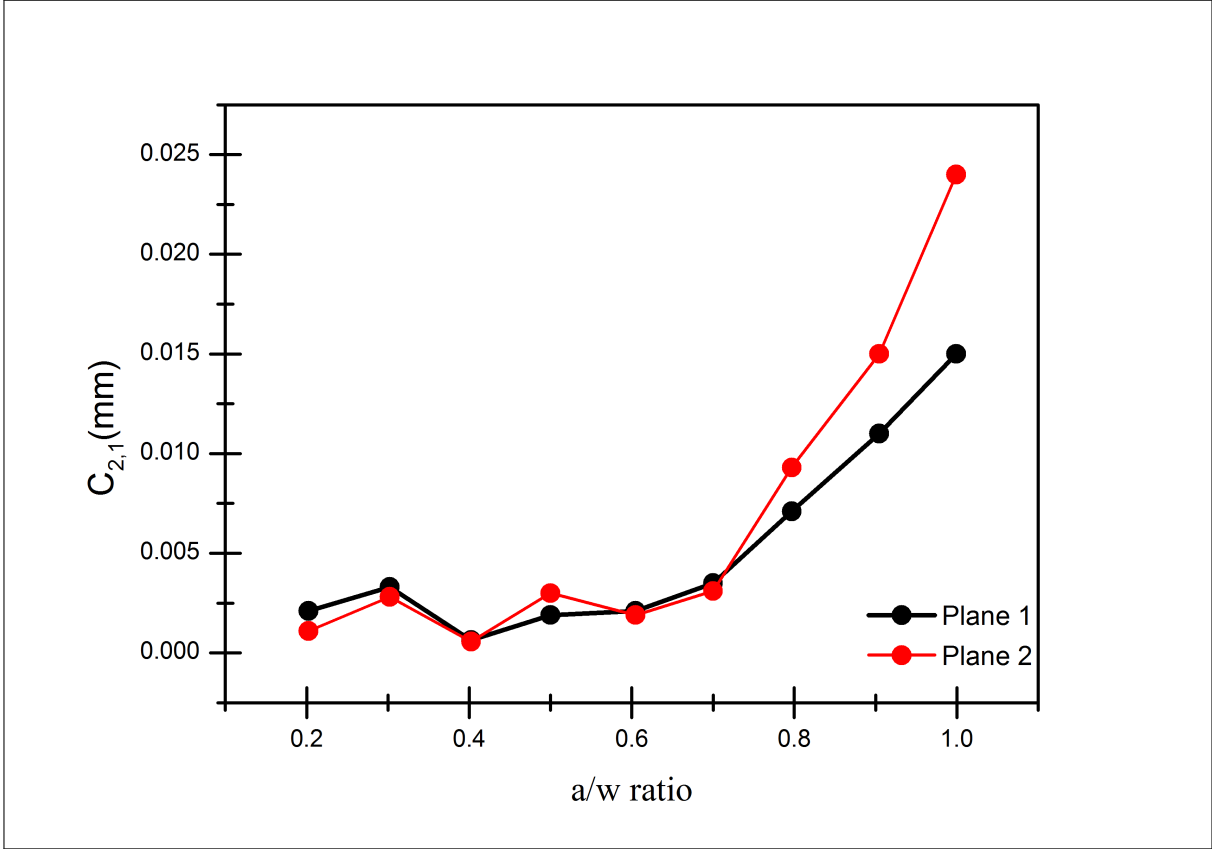


Figure 2.4 The graph of defocus coefficient versus the ratio of Zernike radius (a) over the Gaussian beam radius (w) to determine the lowest defocus coefficient with regard to the ratio.

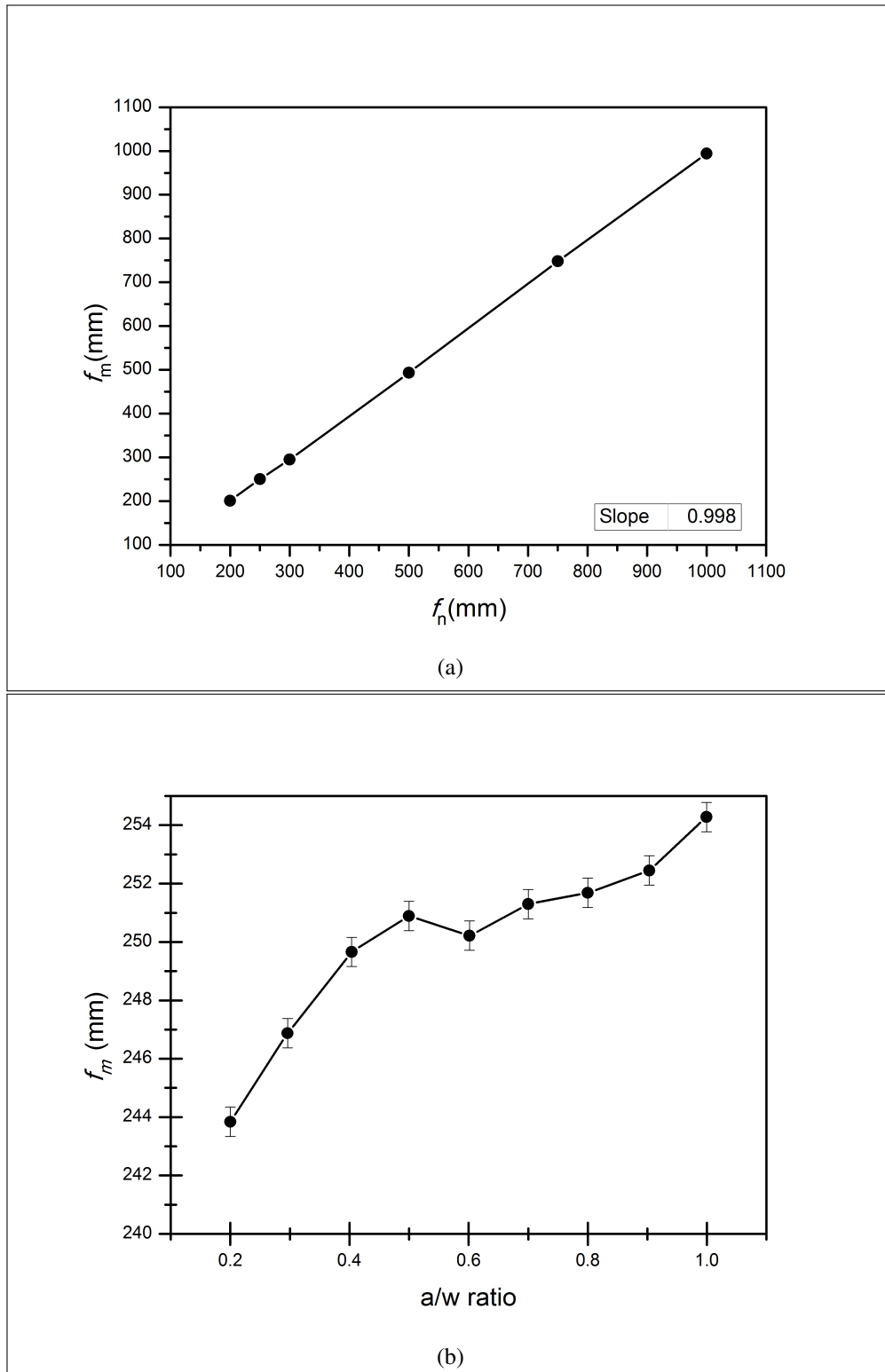


Figure 2.5 (a) Measured focal lengths f_m against the nominal focal lengths f_n . (b) Measured focal length for nominal focal length of $f = 250$ mm as the ratio of radius to beam size increases.

2.5 Thermally induced lensing in Nd: YAG crystal

We used a 1.0% doped Nd: YAG crystal that was 70 mm long, had a diameter of 4 mm at 25 °C, and was pumped at 808 nm. The pump beam was focused (radius of 1.4 mm at the centre of the crystal) within the crystal using a 150 mm lenses as shown in Fig. 2.6. The pump power was varied from 5 W to 55 W, and the transmitted pump power was measured (see Fig. 2.7) to determine the gain saturation point (lasing threshold), which indicated that a strong lensing effect would occur with an increase in the pump power.

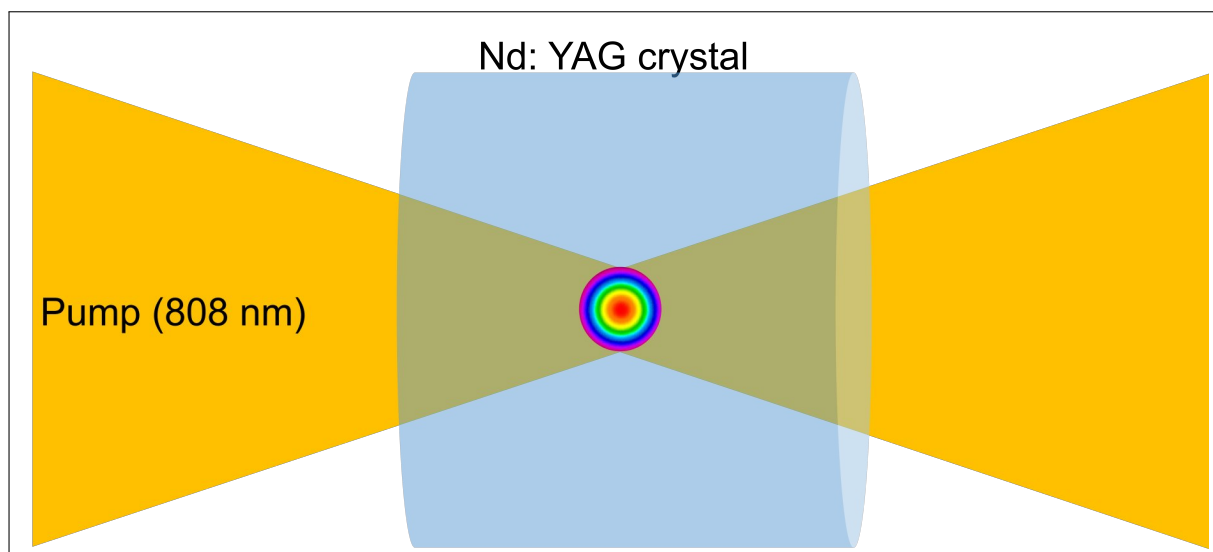


Figure 2.6 The Nd: YAG gain medium pumped by a single-mode diode laser operating with a Gaussian beam at 808 nm (the intensity distribution of the focus pump at the centre of the crystal is also shown).

The thermal lensing in an end-pumped configuration was measured by varying the length of an unstable resonator while measuring the output power (see Fig. 2.8). (We refer to this method as geometrical). L which is the length between the centre of the crystal and the output coupler was varied between 200 mm to 1000 mm in steps of 100 mm. For each length, the power was measured and a drop in power was experienced for different cavity lengths. A power drop is indicative of the fact that the length from the centre of the gain medium to the output coupler is equivalent to the focal length of the thermally induced lens. This, however, is an unreliable measurement, as a power drop may occur more than once at a specific length, which is not anticipated due to a uniform absorption of the pump beam. This unexpected occurrence might be due to inaccurate measurement of the length and aberrations on mirrors.

We thus determined the thermally induced lens based on the calibration technique used in Sec. 3, where we positioned the centre of the gain medium at plane 1 (see Fig. 2.2). Under

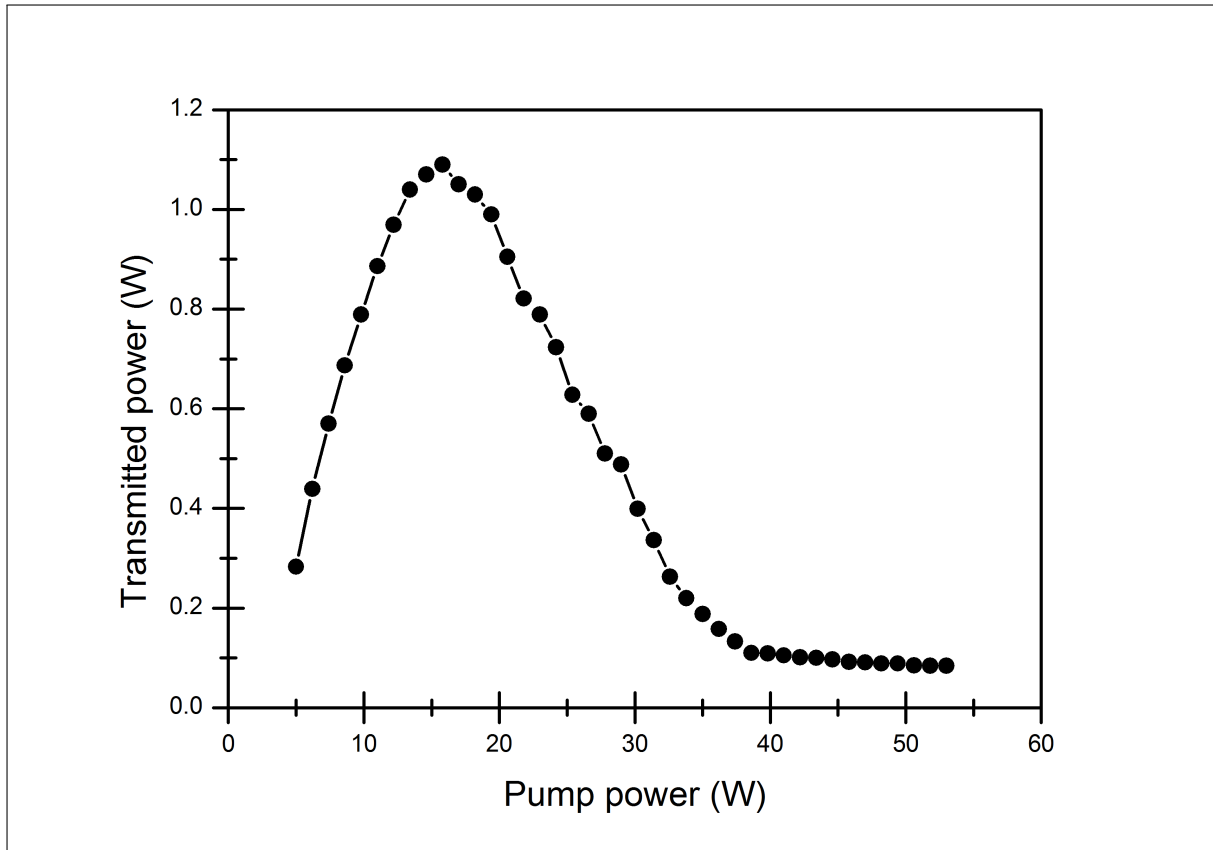


Figure 2.7 Power transmitted against the input pump power to determine the gain saturation. This graph is used to determine if the gain medium is still in good condition and lasing can still occur. In addition, this graph indicates that the gain medium is not damaged, and lasing will start at 17 Amps.

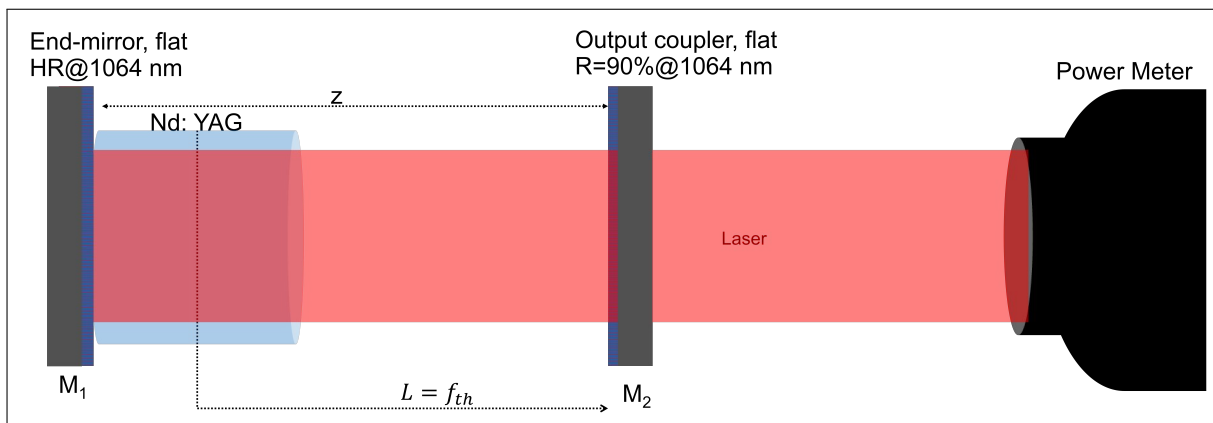


Figure 2.8 Unstable plane-parallel laser resonator used to determine thermally induced lensing.

active pumping, we measured the thermal effect on the collimated probe beam as illustrated in Fig. 2.2. The results in Fig. 2.9, show that the focusing capacity of the thermal lens increases dramatically with an increase in pump power beyond the saturation point and that it is consistent with the uniformity of the pump absorption.

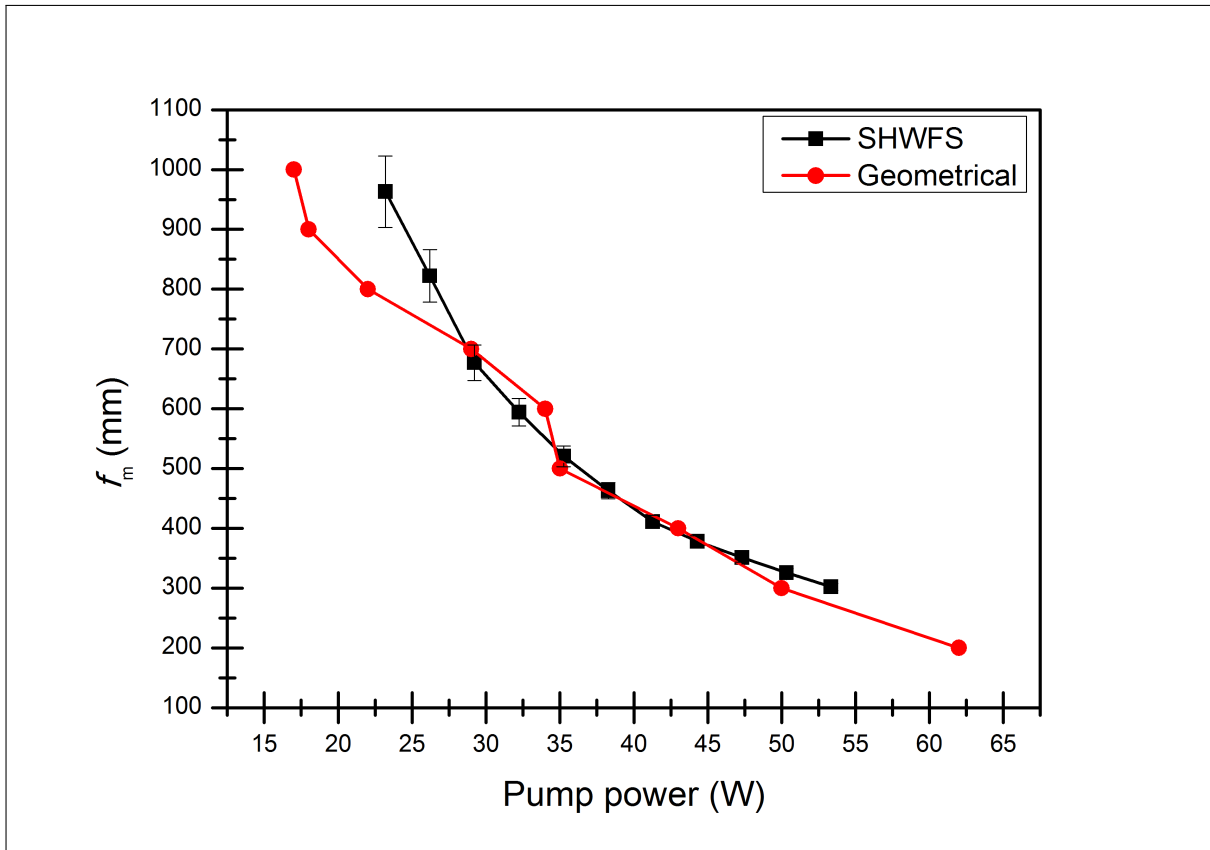


Figure 2.9 The effective focal length of the thermally induced lens as a function of the optical pump power, for two measurement techniques used.

2.6 Summary

A calibration technique was applied to known lenses with high finesse and extended to pumped solid-state gain medium. The measurement of a thermally induced lensing effect with a Shack-Hartmann wavefront sensor in an end-pumped solid-state gain medium was investigated and compared with the thermal lensing measured by varying the length of an unstable resonator while measuring the output power. The SHWFS method was found to be highly consistent with the pump absorption and is considered to be more accurate than a geometrical method.

Chapter 3

Generation of Laguerre-Gaussian modes

In Chapter 1 Section 2, we introduced higher-order laser modes. In this chapter, we will focus on the generation of Laguerre-Gaussian ($LG_{p,l}$) modes using an end-pumped solid-state laser that is able to control the output laser modes. Section 3.1 will focus on the generation of $LG_{0,l}$ modes that have azimuthal order (l) while Sec. 3.2 will focus on generation of $LG_{p,0}$ laser modes that have radial order (p). The results shown in this chapter illustrate the ease of generating $LG_{p,l}$ modes intracavity using DPSSDL.

3.1 Generation of petal-like Laguerre-Gaussian beams

In this section, a solid-state digital laser was used to generate Laguerre-Gaussian modes $LG_{p,l}$ with radial order $p = 0$ and azimuthal order $l = 0$ to $l = 5$. This section demonstrates the fundamental generation of high-order $LG_{0,l}$ modes intracavity.

3.1.1 Introduction

The solid-state digital laser was pumped by a diode laser (808 nm), which was used to improve frequency stability [53]. In the past, diffractive optical elements (DOEs) or computer-generated holograms were used to shape beams, inside or outside the laser resonator [54, 55, 56]. In most cases, the DOEs were designed and manufactured as a phase-and-amplitude optical element that is fixed for beam shaping. We used a phase-only spatial light modulator (SLM) to do amplitude-only beam shaping.

3.1.2 Experimental methodology and concept

We generated Laguerre-Gaussian $LG_{p,l}$ modes (represented by Eq. 1.43 in Chapter 1) by considering a plano-concave solid-state digital laser resonator that is end-pumped with a multi-mode fibre coupled diode, and a Hamamatsu spatial light modulator (SLM) encoded with an amplitude mask [22, 57]. The mask consists of petal-like azimuthal order of $l=0$ to 5. A schematic representation of the experimental setup is presented in Fig. 3.1. The Nd: YAG rod

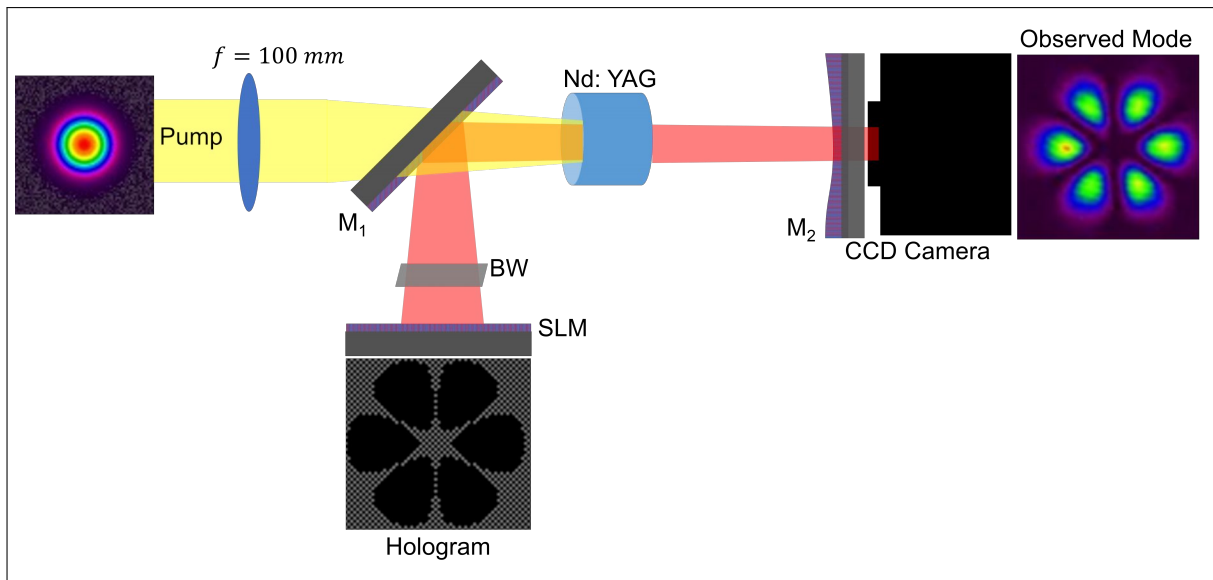


Figure 3.1 Schematic representation of DPSSDL, with the laser mode exiting the laser cavity comprising SLM and M_2 . Diode laser (pump) operating at 808 nm is shown in yellow, while the exciting (1064 nm) beam at the output coupler (M_2) is shown in red.

crystal (length of 25 mm) had a 1.1% neodymium doping concentration and was AR-coated for 808 nm to minimise pump reflections. The laser crystal was mounted inside a 21 °C water-cooled copper block. The diode laser used for end-pumping (Jenoptic, JOLD-75-CPXF-2P) had a maximum output power of 75 Watts at an emission wavelength of 808 nm (at an operating temperature of 25 °C). The pump diode laser output was coupled into a fibre with a core diameter of 400 μm and was focused at the centre of the gain medium that has a radius of 2 mm.

The planoconcave cavity comprised of a phase-only spatial light modulator (SLM), which acted as a flat-end mirror of the cavity with a reflectivity of 95%. The output coupler mirror (M_2) had a radius of curvature of 400 mm and a reflectivity of 90%. The resonator was designed to form an L-shape (to avoid illuminating the SLM with the residual pump light) by including 45° mirrors (M_1) within the cavity that were highly reflective for 1064 nm and highly transmissive

for 808 nm. The beam exiting the output coupler was captured using a CCD camera, and the images were normalised to 1.

3.1.3 Results and discussion

A gray-scale digital computer-generated hologram [57] was encoded to the SLM (see Fig. 3.2) in the form of amplitude masks, by introducing high loss at zero intensity on the selected order. The laser resonator that was used satisfied the ABCD matrix, and it was able to generate a

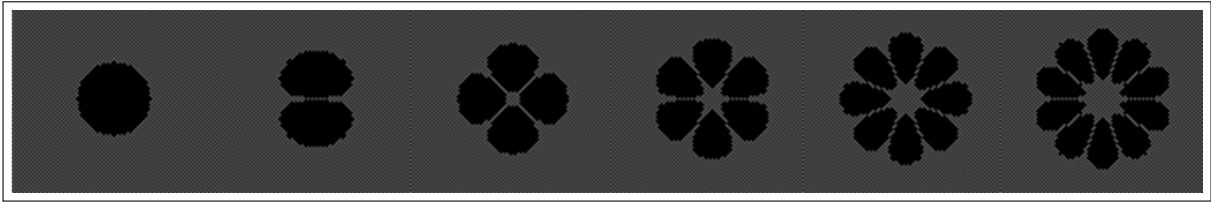


Figure 3.2 Computer-generated hologram (CGH) encoded to the SLM for the generation of $LG_{p,l}$ modes of order $p = 0$ & $l = 0 - 5$.

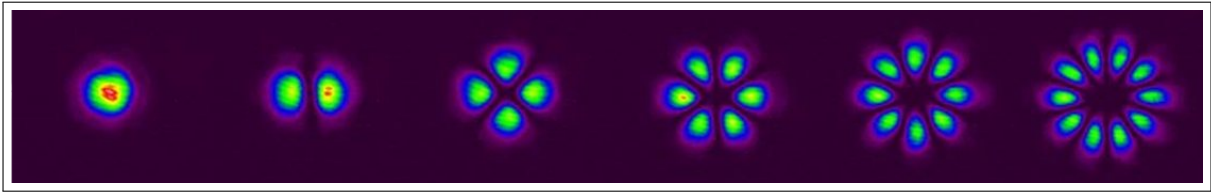


Figure 3.3 Observed intensity profile for $LG_{p,l}$ modes of order $p = 0$ & $l = 0 - 5$, at the output coupler (M_2 on Fig. 3.1).

single mode [58]. Thus, we could analyse the generated laser beams and report the results in Fig. 3.3.

3.1.4 Summary

We have shown that it is possible to generate petal-like Laguerre-Gaussian beams using a diode-pumped solid-state digital laser. Our results show that one can digitally control any order modes by selectively exciting the modes. The results also suggest that a diode-pumped solid-state digital laser can be used as the test tool for manufacturing amplitude masks and DOEs.

3.2 Generation of radial order Laguerre-Gaussian beams using a solid-state digital laser

A digital laser was used to generate high-radial-order Laguerre-Gaussian ($LG_{p,0}$) modes by loading digital holograms on a phase-only spatial light modulator that acts as an end mirror of a diode-end-pumped laser resonator. The digital holograms were encoded with an amplitude ring mask, which contained absorption rings that match the p -zeros of the Laguerre polynomial. In this section, we demonstrate the generation of high-quality $LG_{p,0}$ modes with a mode volume that is directly proportional to the mode order, p , and we propose the potential use of the digital laser as a tool for simulating optical elements that will be used in pursuing high-brightness lasers.

3.2.1 Introduction

Since high-power solid-state lasers are the most dynamic branch of laser science, they have become an increasingly important tool for modern technology [59]. A new design of the solid-state laser in the form of a digital laser was recently discovered by South African researchers [60]. This technology may well introduce a new era in laser manufacturing and the application in industry of the digital laser to be used as a simulation [55] and testing tool [54, 61] in many future laser manufacturing processes.

When the solid-state digital laser is pumped by a diode laser, better frequency stability, higher efficiency, higher brightness and longer operational lifetime are provided [62]. The digital laser comprises of an intra-cavity phase-only spatial light modulator (SLM) that acts as an end mirror of the laser resonator cavity. The SLM is used to introduce a phase mask and/or amplitude mask inside the laser resonator by digitally loading a gray-scale hologram image that represents a mask of interest. The digital laser is limited in the output power it can produce when compared to standard diode-end-pumped solid-state lasers [12, 29, 53] due to low damage threshold of the SLM. Nevertheless, the digital laser is found to be a stable intra-cavity beam-shaping tool that can be used to simulate any desired intra-cavity optical element prior to it being manufactured.

In this section, we show how to generate high-radial-order Laguerre-Gaussian ($LG_{p,0}$) modes from zero up to a radial order of $p = 4$, by selectively encoding and loading amplitude digital hologram masks on a phase-only SLM that contains absorbing rings that match the p -zeros of the Laguerre polynomial. We show that the generated $LG_{p,0}$ modes results are highly consistent with similar previous [56] experimental results there were obtained using a

physical diffractive optical element that had been lithographically engraved with aluminium absorbing rings and inserted inside the resonator cavity. The results obtained in this section are far superior to the results in Ref. [56], due to the better design of the amplitude mask that allows for better mode matching of the laser, the pump and the absorbing rings.

3.2.2 Radial Laguerre-Gaussian modes

The electric field of radial Laguerre-Gaussian modes $LG_{p,0}$ where p is the radial-order geometries, can be mathematically represented by the following equation:

$$U_{p,0} = \sqrt{\frac{2}{\pi}} \times \frac{1}{w} \times L_p^0 \left(\frac{2r^2}{w^2} \right) \times e^{-\frac{r^2}{w^2} - \frac{ikr^2}{2R(z)}} \times e^{-i(2p+1)\arctan\left(\frac{z}{R}\right)}. \quad (3.1)$$

$U_{p,0}$ consists of a central peak that is surrounded by p concentric rings. The Laguerre polynomial ($L_p(X)$, let $X = 2r^2/w^2$) for the rings is defined in Tab. 3.1:

Table 3.1 Laguerre polynomials and their roots.

p	$L_p(X)$	r_i/w			
0	1	1			
1	1-X	0.707106			
2	$X^2/2 - 2X + 1$	0.541195	1.306562		
3	$-X^3/6 + 3X^2/2 - 3X + 1$	0.455946	1.071046	1.773407	
4	$X^4/24 - 2X^3/3 + 3X^2 - 4X + 1$	0.401589	0.934280	1.506090	2.167379

The spot size w_0 in Eq. 3.2 only defines the size of the fundamental Gaussian beam $LG_{0,0}$, where the radial-order $p = 0$ Laguerre-Gaussian $LG_{p,0}$ modes have intensity distribution profiles that contain a peak at the centre, surrounded by p concentric rings of bright and dark rings. The intensity profile of the dark concentric rings of the ($LG_{p,0}$) modes matches the Laguerre polynomial p -zeros. The intensity profile of the $LG_{p,0}$ modes is defined by the absolute square of Eq. 3.1 and the $LG_{p,0}$ beam width, w , which is based on a second moment, the radius is given as:

$$w = w_0 \sqrt{2p+1}, \quad (3.2)$$

and the propagation factor M^2 of such modes is given as:

$$M^2 = 2p+1. \quad (3.3)$$

To force the laser to generate $LG_{p,0}$ modes, masks containing p absorbing rings with a geometry that closely follows the location of the Laguerre polynomial p -zeros (see Tab. 3.1) were digitally encoded to the SLM of the digital laser [22]. This would allow for the generation of such $LG_{p,0}$ modes.

3.2.3 Experimental methodology and concept

To generate radial-order Laguerre-Gaussian $LG_{p,0}$ modes, we considered a planoconcave solid-state digital laser resonator end-pumped with a multi-mode fibre-coupled diode laser, where the Hamamatsu spatial light modulator (SLM 1) was encoded with an amplitude mask that would function as an end mirror of the resonator. The amplitude mask was encoded to have p absorbing rings of varying width/thickness that would match 98% of each null of the $LG_{p,0}$ mode, for radial order $p = 1 - 4$. A schematic representation of the experimental setup is presented in Fig. 3.4.

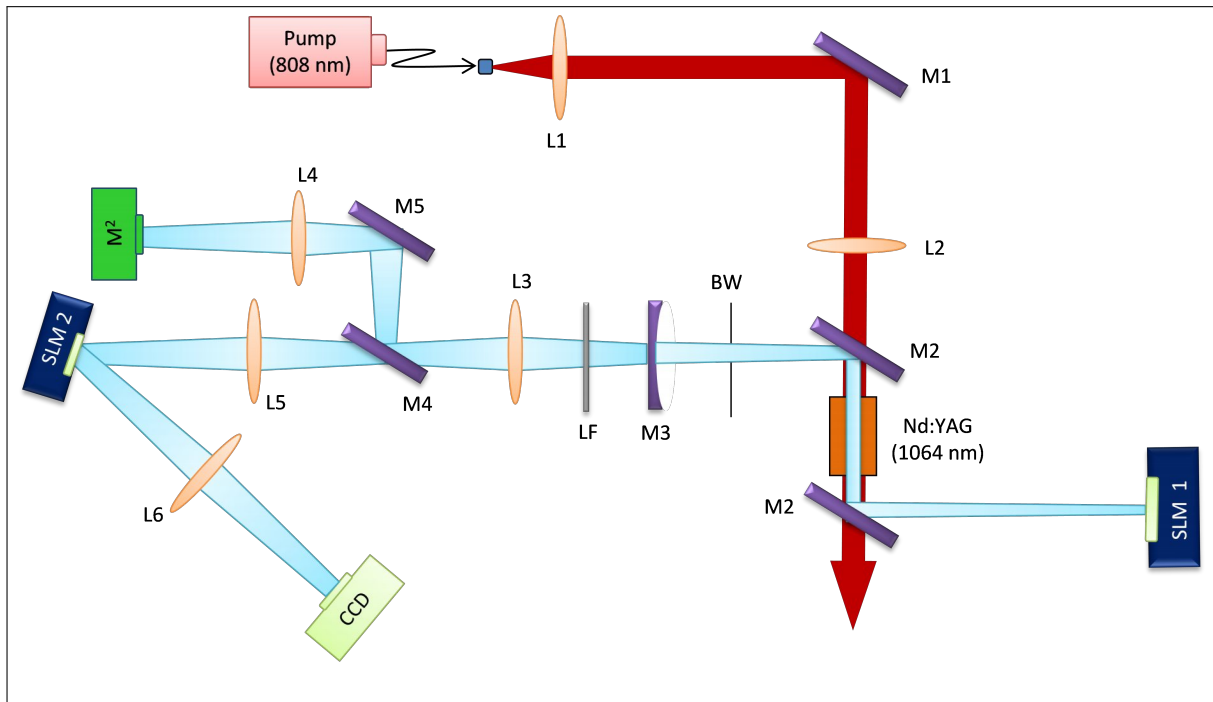


Figure 3.4 Schematic representation of the DPSSDL, with the laser mode exiting the at the output coupler mirror (M3). Diode laser operating at 808 nm is shown in red, while the excited beam is shown in blue.

The crystal used in Fig. 3.1 is the same as the crystal used in Fig 3.4. In addition, it was pumped the same. The resonator was designed to form a Z-shape (to avoid illuminating the SLM with the residual pump light) by including 45° mirrors (M2) within the cavity that were

highly reflective for 1064 nm and highly transmissive for 808 nm. The Brewster window (BW) was used as polarizer since the SLM was polarisation sensitive. The Brewster window (BW) positioned at Brewster's Angle ($\approx 56.3^\circ$) so that the P-polarised component of the light could enter and exit the window without reflection losses, while the S-polarised component was partially reflected. The resonator length was chosen to be 173 mm and the Nd: YAG crystal centre was positioned 120 mm from the SLM 1.

The Line Filter (LF) was introduced to transmit only 1064 nm and block the 808 nm pump. The laser beam was transmitted out of the cavity through an output coupler mirror (M3 in Fig. 1) and it was 1:1 relay-imaged, using two 125 mm lenses (L3 and L4) to a Photon ModeScan Meter for measuring the beam quality factor M^2 . The emitted beam was also 1:1 relay-imaged using two 125 mm lenses (L3 and L5) to the Meadowlark optics spatial light modulator (SLM 2). The aim was to perform modal decomposition [63, 64] into the Laguerre-Gaussian basis. The measurement of the signal at the origin of the Fourier plane using a 125 mm lens (L6) was captured using a CCD camera (Spiricon, LBA-USB).

3.2.4 PC run numerical simulations

We perform a numerical calculation of the fundamental mode of the resonator that will contain an intra-cavity amplitude mask. The simulation is based on the expansion of the resonant field on the basis of the eigenmodes of the empty cavity (without any diffracting object). This method is described elsewhere for the case of a planoconcave cavity including an absorbing ring on the plane mirror [65]. The modelling given in Ref. [65] can be easily adapted to the case of an amplitude mask made up of concentric absorbing rings, just by evaluating the overlapping integral (Eq. A10 of Ref. [65]) upon all the regions of transparency of the mask.

The width of the absorbing rings is simulated to be a 98% match of the $LG_{p,0}$ mode p -zero nulls that will be oscillating inside the resonator. This allows for better mode selection since each absorbing ring's width will be tailor-designed to match the oscillating $LG_{p,0}$ mode p -zero nulls inside the resonator (see Fig. 3.5). The simulated $LG_{p,0}$ modes of $p = 1 - 3$ cross-section profiles are also shown in Fig. 3.5.

The thickness of the absorbing rings for the $p=3$ mode increases from the inner ring to the outer ring. The minimum thickness of the ring is $20 \mu\text{m}$, which corresponds to the pixel pitch of the SLM 1 in Fig. 3.4.

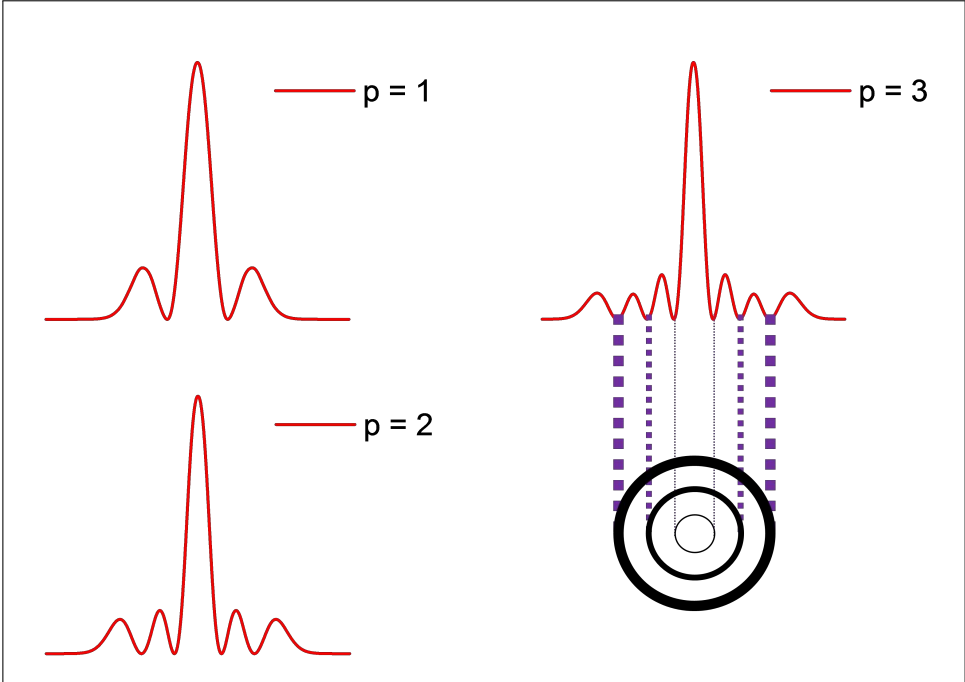


Figure 3.5 Intensity cross-section of numerically simulated lowest-loss eigenmodes for $p=1$ to 3, when a mask containing an absorbing p ring is inserted inside the resonator. The mask is inserted in such that the high-loss absorbing ring coincides with the intensity p -zero nulls. For an example, we looked at $p = 3$ Laguerre-Gaussian mode.

3.2.5 Results and discussion

The intensity profiles for selected $\text{LG}_{p,0}$ modes with appropriate gray-scale masks that contain p -absorbing rings are shown in Fig. 3.6a and Fig. 3.6b. The gray-scale images in Fig. 3.6a, also termed the digital holograms that contain p -absorbing rings and aperture, were encoded on the SLM using complex amplitude modulation [57]. Since the generated high-order $\text{LG}_{p,0}$ modes come from a stable resonator cavity, their beam sizes w and beam propagation factor M^2 are known analytically, and they can be compared to experimental results as summarised in Fig. 3.6c and 3.7a. It is evident that the cavity selects desired modes with appropriate beam sizes and beam propagation factors, all of which are in good agreement with the theory. The modal decomposition [64, 66] was performed to determine the mode purity of the generated high-order $\text{LG}_{p,0}$ modes. In Fig. 3.7b the mode purity is greater than 90% for modes $p = 0$ to $p = 2$, and then it drops to just below 90% to 75% for $p = 3$ and $p = 4$.

The output power from a laser is defined to be linearly proportional to the mode volume, V_p , where the volume of the p^{th} radial mode is determined from:

$$\begin{aligned} V_p &= \int_0^{l_0} \pi W^2(z) dz \\ &= \pi w_0^2 l_0 (2p + 1) \left(1 + \frac{l_0^2}{3z_r^2} \right) \\ &= V_0 M^2 \left(1 + \frac{l_0^2}{3z_r^2} \right), \end{aligned} \quad (3.4)$$

where l_0 is the length of the gain medium and V_0 is the mode volume of the $p = 0$ (Gaussian) mode. In the limit that the length of the crystal is much smaller than the Rayleigh range of the beam, then Eq. 3.4 can be simplified to $V_p = M^2 V_0$. The results of the output power versus input power for the $\text{LG}_{0,0}$ mode and $\text{LG}_{4,0}$ mode are shown in Fig. 3.8a, while those for slope efficiency and the pump threshold of the generated $\text{LG}_{p,0}$ modes of $p = 0 - 4$ are shown in Fig. 3.8b.

The output power is also inversely proportional to the round-trip losses. This suggests that the higher-order radial modes have an output power that may be expressed by Eq. 3.5 (see Fig. 3.8b):

$$\frac{P_p}{P_0} = (2p + 1) \times \frac{\sigma_0}{\sigma_p}, \quad (3.5)$$

where the subscripts p and 0 refer to the radial mode orders and the round-trip losses are denoted by σ . It is clear that higher-order modes extract more power compared to a mode order of $p=0$, due to an increase in mode volume, as shown in Eq.3.4. To increase mode volume the

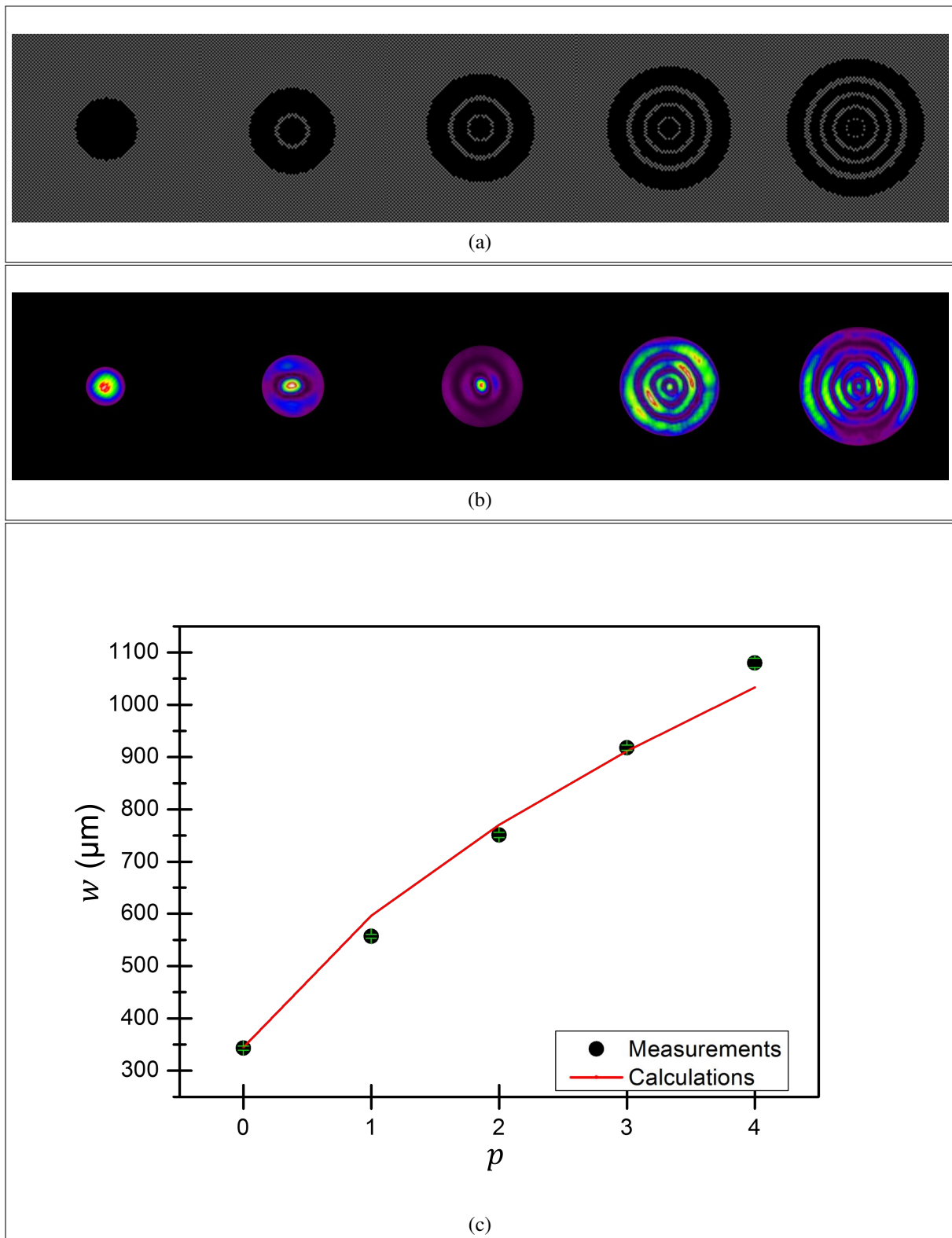


Figure 3.6 (a) Gray-scale (0 to 2π) holograms with amplitude modulation in the form of a checkbox. (b) Observed intensity profiles (normalised to 1) of the Laguerre-Gaussian modes of order $p = 0 - 4$ at the output coupler. (c) Beam width at the output coupler as a function of mode order, with theoretical (Eq. 3.2) results represented by a solid red line.

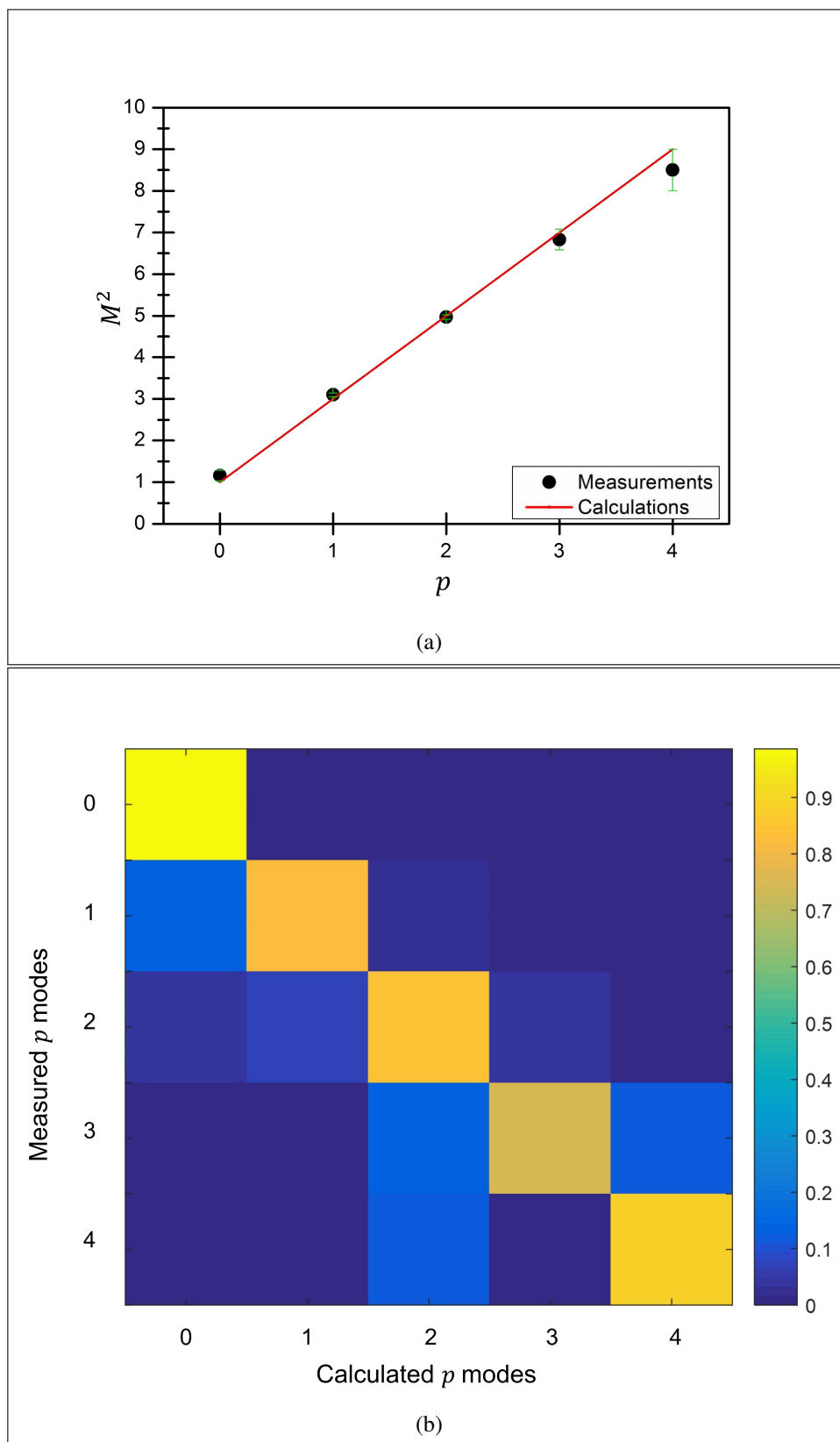


Figure 3.7 (a) Beam propagation factor as a function of mode order, with theoretical (Eq. 3.3) results represented by a solid line. (b) The plot of modal decomposition results with intensity normalised to 1, for $p = 0 - 4$.

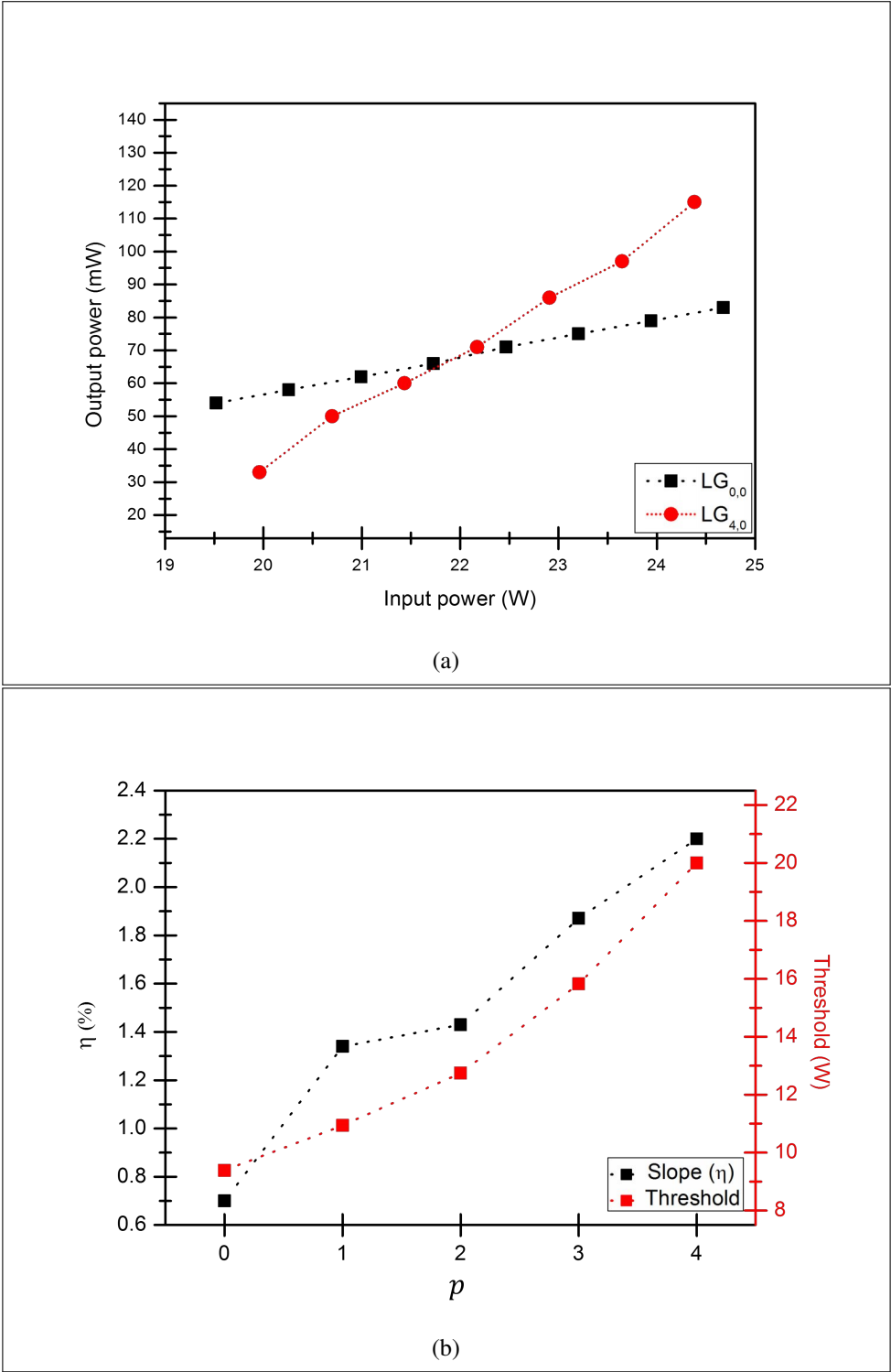


Figure 3.8 (a) Power extraction (output power) for $p = 0$ and $p = 4$, as the function of the diode pump power (input power). (b) Slope efficiency (η) and pump threshold as a function of mode order.

round-trip losses can be kept to a minimum (compared to the extracted gain), as shown in Eq. 3.5. Fig. 3.8a shows a graph of the output power versus input power of the $LG_{0,0}$ and $LG_{4,0}$ modes, at a pump power of above 22 watts. The power extracted from $LG_{p,0}$ mode of order $p = 4$ exceeds that of the fundamental Gaussian mode, $p = 0$, despite the fact that the $LG_{4,0}$ mode has a higher loss. This loss results from the fact that the extra gain compensates for the extra losses when the laser resonator generates the $LG_{4,0}$ mode. The results show that it is possible to select a higher-order $LG_{p,0}$ mode of very high beam quality factor and mode purity, with the aim of extracting more power within a laser resonator that contains an intra-cavity SLM encoded with an amplitude absorbing rings mask that operates as an end mirror of the resonator.

3.2.6 Summary

We have shown that it is possible to selectively excite high radial order LG modes of $p = 0 - 4$ that are in high agreement with the theoretically expected results for the beam profiles, sizes and quality factor. Our results show that one can digitally excite a single high-order $LG_{p,0}$ mode by loading a gray-scale digital hologram that represents the mode of interest, in an attempt to extract more power from the laser gain medium. We have shown that by generating $LG_{4,0}$ mode, we can extract more power from the digital laser gain medium than when generating the lowest order $LG_{0,0}$ mode and using an amplitude mask introduced on an intra-cavity SLM, which acts as an end mirror of the resonator. Our findings also suggest that a digital laser can be used as a simulation test tool for manufacturing amplitude masks to develop a high-brightness laser that will operate by selective excitation of a single higher-order $LG_{p,0}$ laser mode above the critical input power.

Chapter 4

Radial Laguerre-Gaussian mode generation using incomplete amplitude mask

In this chapter, we experimentally demonstrate selective excitation of high-radial-order Laguerre-Gaussian (LG_p or $LG_{p,0}$) modes with radial order, $p = 1-4$ and azimuthal order, $l = 0$, using a diode-pumped solid-state laser (DPSSL) that is digitally controlled using a spatial light modulator (SLM). An amplitude with p -absorbing rings, of various incompletenesses (segmented), using gray-scale computer-generated digital holograms (CGDHs), was displayed on an SLM that acted as an end mirror for the diode-pumped solid-state laser. The various incomplete p -absorbing rings were digitally encoded to match the zero intensity nulls of the desired LG_p mode. We illustrate that the creation of LG_p , for $p = 1$ to $p = 4$, only requires an incomplete circular p -absorbing ring of $\approx 37.5\%$, which causes the DPSSL resonator to have a lower pump threshold power, while maintaining the same laser characteristics (such as beam propagation properties).

4.1 Introduction

High-order Laguerre-Gaussian ($LG_{p,l}$) beams are used in many applications employed in industry, medicine, the military and communications [67, 68, 69, 70]. Applications such as optical trapping [71], which are also termed optical tweezers, have been shown to be inconceivable without higher-order Laguerre-Gaussian ($LG_{p,l}$) beams. This is especially the case for those applications that contain only the azimuthal order (l) component, as they can

transfer orbital momentum (OM) to a trapped particle (this is mainly used for manipulating biological cell). A vortex field is created around the particle, thereby “forcing” the particle to rotate around the optical axis of the beam and trapping the cell [72]. Over the years, interest in $LG_{0,l}$ beams that have only the azimuthal index has led to the optical tweezers becoming known as optical vortices [73].

The current demand of high brightness lasers, especially in military and applications that require high brightness laser, has sparked a revived interest from the researchers to study further high order LG beams, especially those that have only the radial order, p , index. The notion is to intra-cavity generate LG_p mode to be a fundamental mode that will have high energy [74]. Over the years it has been shown that LG_p modes can be created using extra-cavity and intra-cavity methods [22, 75, 76]. The major disadvantage of LG_p modes in many applications has been using the laser that produces the fundamental Gaussian beam.

As previously discussed in Chpt. 3, we already shown that LG_p modes can be generated by inserting of a mask made-up of p -absorbing rings having a radii coinciding with the zeros of the desired LG_p mode within the cavity [56]. However, doing that introduces supplementary losses and consequently increases the laser threshold. In this chapter, we will show that it is possible to force the fundamental mode of the laser to be a single high-order LG_p mode by using incomplete absorbing rings allowing the reduction of inserting losses [77, 78]. It is worthwhile to recall that an LG_p beam is made up of a central peak surrounded by p -rings of light separated by a p -zeros of intensity. The laser resonator that we opted to use was a diode-end-pumped system due to the ease of controlling the pump spot size, the wavelength of the pump, the divergence and incident angle of the pump beam onto the gain medium [12, 30, 79].

Forcing the fundamental mode to be an LG_p mode can offer some advantages:

- An improved energy extraction from the laser medium due to a great lateral extent compared to the usual Gaussian beam. The LG_p mode can be transformed in the focal plane of a lens into a single-lobed beam by using a binary diffractive optical element playing the role of the rectifier [80].
- A simple diaphragm can transform a LG_1 beam into an optical bottle beam [81] or a flat-top intensity profile [82]

4.2 Radial-order Laguerre-Gaussian modes

Since the propagation of the Gaussian beam is well-known and can be derived analytically [83], one can transfer this knowledge to higher-order modes. Radial Laguerre-Gaussian (LG_p) beams have an intensity distribution that is made up of the central bright lobe and concentric rings, thus the mathematical representation can be written as follows [15]:

$$I = \frac{2}{\pi} \times \frac{1}{w_p^2} \times \left[L_p^0 \left(\frac{2r^2}{w_p^2} \right) \right]^2 \times e^{-\frac{2r^2}{w_p^2}}, \quad (4.1)$$

where r is the radial coordinates and L_p^0 is the Laguerre polynomial. All other parameters have their usual meaning as defined in respect of a Gaussian beam [15].

The maximum intensity occurs at a central peak while the intensity associated with the ring is lower. The intensity patterns of the LG_p beams broaden as the radial order index p increases, which defines the width (w_p), using second-moment radius (see Eq. 3.2 in Chpt. 3). In addition, the propagation properties of LG_p beams are defined by the propagation factor (M^2) that is defined by Eq. 3.3. The propagation factor (M^2) is used to measure the beam quality of the laser beam according to ISO Standard 11146 [84].

We numerically analysed LG_p propagation by starting with Laguerre polynomial (part of Eq. 4.1), and taking radial order as $p = 1 - 4$. The Laguerre polynomial ($L_p(X)$) considering that $X = 2r^2/w^2$, and the position of the zeroes of intensity, r_i , are given in Tab. 3.1. More examples can be found in mathematical handbooks [17]. To force the laser to generate LG_p modes, a digital mask containing p -absorbing rings – with a geometry that closely follows the location of the Laguerre polynomial p -zeros as illustrated in Tab. 3.1 (column 3) – was digitally encoded to the SLM of the digital laser [22], which subsequently allowed for the generation of such LG_{p,0} modes.

4.3 Experimental methodology and concept

The experimental methodology and concept are the same as in Chpt. 3 SubSec. 3.2.3.

4.4 A PC run numerical simulations for incomplete ring

From Fig. 3.4 in Chpt. 3, the plano-concave cavity has been shown to have a length (L) of 173 mm, and the concave mirror (M3) has a radius of curvature $R = 400$ mm. The focus is on the generation of LG_p mode imposed by the insertion of a single absorbing ring of radius r_A .

The ring is set against the plane mirror (SLM 1 of Fig. 3.4) and a diaphragm of radius r_0 is set against the plane mirror (SLM 1 of Fig. 3.4). The p -absorbing ring diaphragm is also encoded

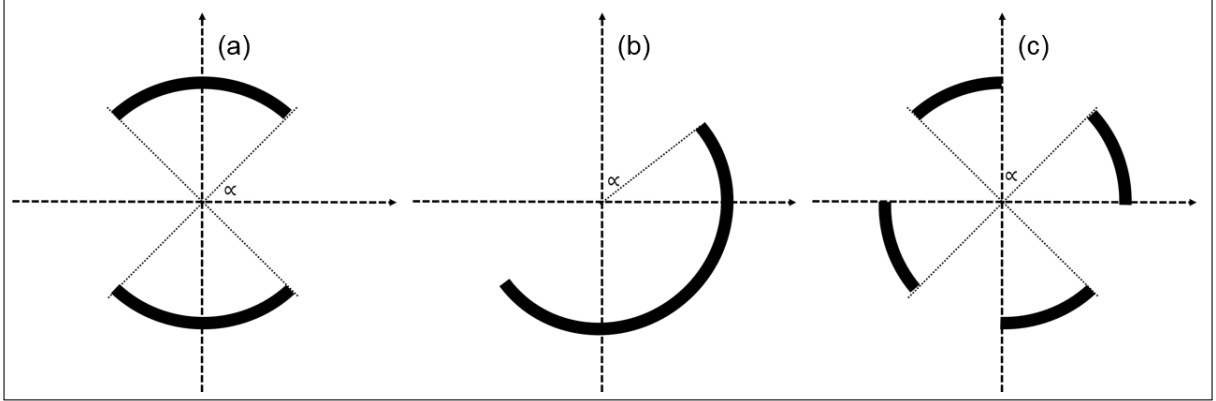


Figure 4.1 Schematic diagram illustrating a 50% complete p -absorbing ring, regardless of the symmetry.

to the SLM. Since part of the fundamental mode loss level is due to the circular absorbing ring mask, we intend to reduce such losses by using an incomplete absorbing ring mask (see Fig. 4.1).

The losses associated with the incompleteness of the absorbing ring do not depend on how many times the absorbing ring has been segmented (see Fig. 4.1). The losses of the laser depend on the overall effect of each incomplete absorbing ring, i.e. for a full ring, $\alpha = 0$, the fundamental mode of the resonator is expected to be Laguerre-Gaussian mode of radial order $p = 1$ (LG_1), with a beam propagation factor of $M^2 = 3$ (by choosing $p = 1$ and $l = 0$ in Eq. 3.3 of Chpt. 3 SubSec. 3.2.3). The ring is almost non-existent, at $\alpha > 0.95\pi/2$, thus the Gaussian mode will oscillate. However, the LG_p of order $p=1$ will oscillate, provided that the angle α of the absorbing ring is kept at less than $0.95\pi/2$ (see Fig. 4.2a). The propagation factor M^2 of the fundamental mode will not change from 3 (see Fig. 4.2b), up until the moment that the angle α is close to $\pi/2$. The laser resonator will then select $p=0$ mode and the M^2 will become 1.

The losses of the fundamental mode, δ , are indicated in Fig. 4.3a, as a function of the beam truncation ratio Y_c for different values of angle α . When α is equal to $\pi/2$, the cavity is expected to generate a Gaussian fundamental mode of $p = 0$, since the cavity losses will be lowest (see Fig. 4.3a). When $\alpha = 0$, the cavity is expected to generate a $p = 1$ as its fundamental mode, since the ring will be complete and the losses will be highest (see Fig. 4.3b).

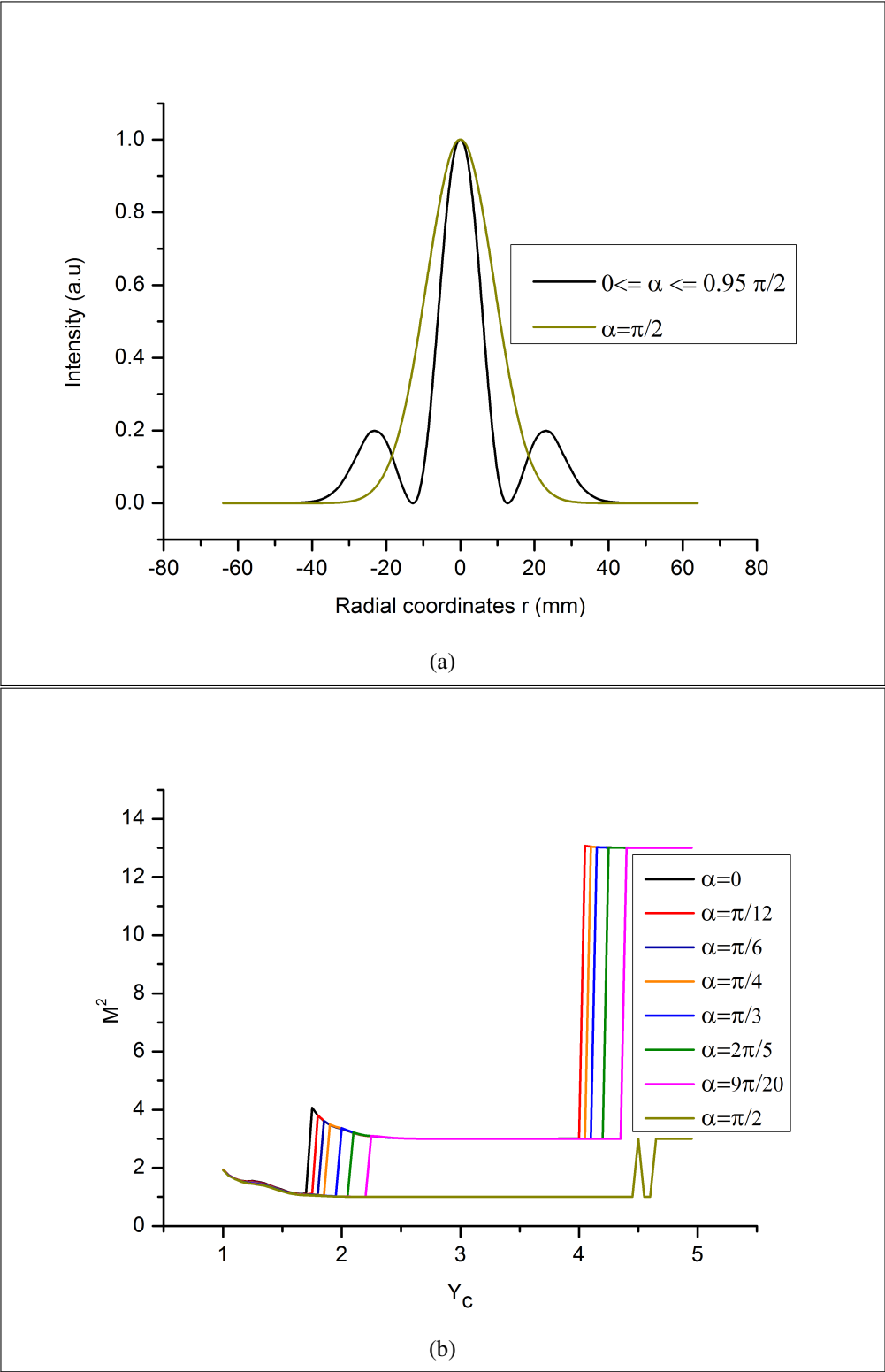


Figure 4.2 (a) Numerically simulated fundamental mode shape at the far-field. (b) Numerically simulated propagation factor M^2 as a function of truncation ratio $Y_c = r_0/w$ (r_0 is the aperture radius, while w is the beam width).

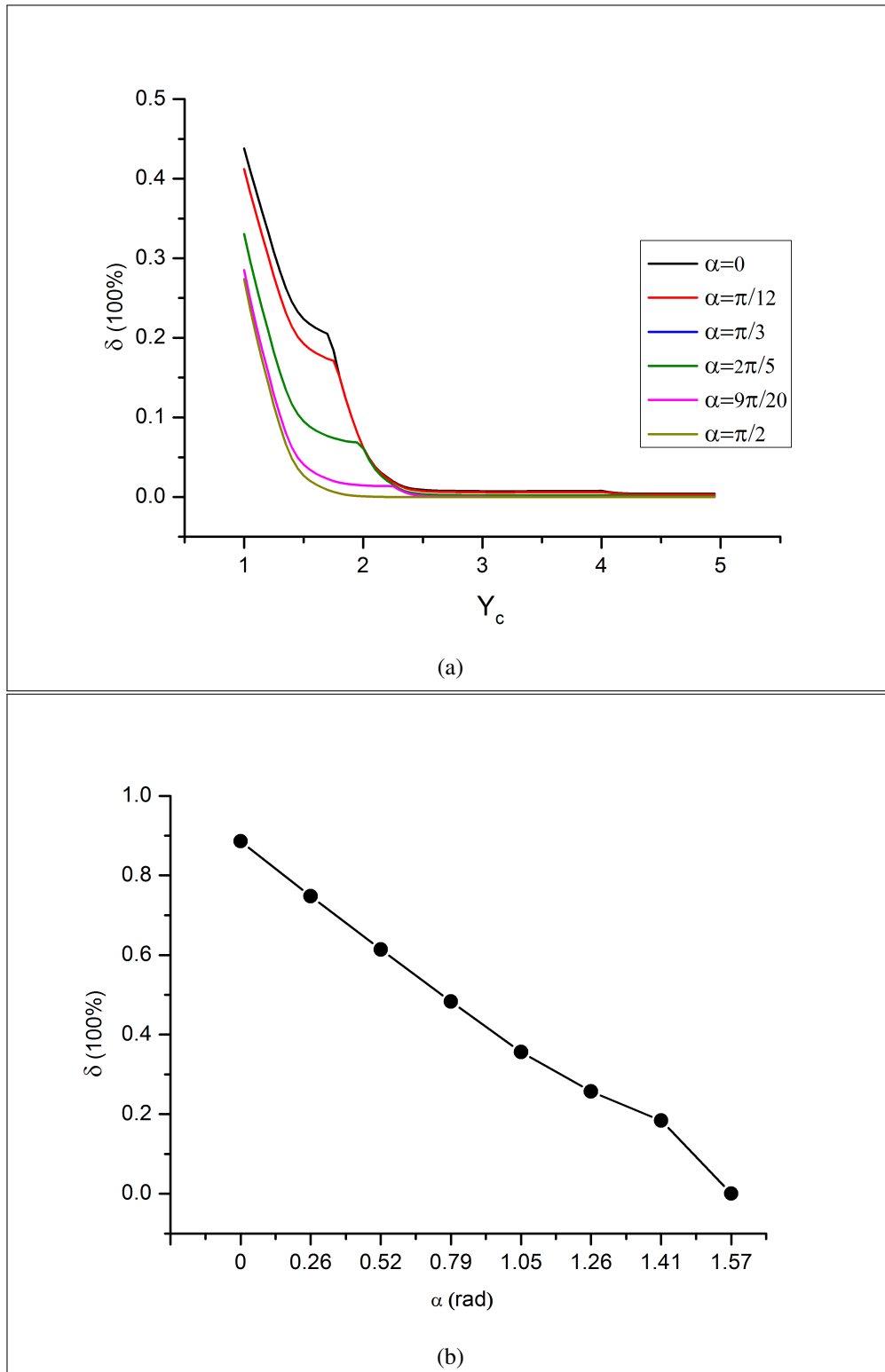


Figure 4.3 (a) Numerically simulated intra-cavity losses (δ) of the fundamental mode as the function of the beam truncation ration (Y_c). (b) Numerically simulated intra-cavity losses (δ) of the fundamental mode as the function of ring incompleteness (α).

The simulation of the losses of the laser resonator as a function of the absorbing ring completeness angle (α) is shown in Fig. 4.3b. The simulation shows that for varying angle (α) from a full ring of 100% completeness of $\alpha = 0$, to $\alpha = 1.4 = 0.88\pi/2$, the cavity will select $p = 1$ mode as the fundamental mode of the cavity. In addition, between $\alpha = 1.4$ and $\alpha = 1.6 = \pi/2$, the simulation shows that the losses will be decreasing at a fast rate towards zero and the laser resonator will then select $p = 0$ as the Gaussian fundamental mode. The concept is tested by varying the completeness of the ring, by changing α on the computer-generated digital holograms (CGDHs). The experimental results are shown in Section 4.5, where we measured the pumping threshold, ε_{th} , the propagation factor M^2 , the generated LGp beam width, w_p , and the slope efficiency, η_p , of the output LGp beams.

4.5 Results and discussion

The results of the mode selection by the laser resonator, with varying completeness of the p -absorbing ring, are shown in Fig. 4.4. The absorbing ring completeness varied between 12.5% to 100%. Exciting the modes from the cavity was achieved by employing CGDH amplitude masks, which were encoded as pixelated grey images and displayed onto an SLM that also acted as a flat-end mirror of the resonator of the DPSSL resonator [22]. The CGDH amplitude masks contained p -absorbing rings of varying circular completeness and their corresponding intensity profiles are shown in Fig. 4.4 for different orders. From the intensity profiles, it is clear that the desired modes are generated when the completeness is above 37.5%.

The results in Fig. 4.5a show that when the completeness of the ring is less than 37.5%, the cavity is not generating LG $_p$ mode, but different laser beams with varying propagation factor M^2 values. The results further confirm that when the completeness of the ring is greater than or equal to 37.5%, the resonator produces the expected LG $_p$ modes with the expected propagation factor M^2 values that are consistent with the theoretical values when using Eq. 3.3 in Chpt. 3, for all generated LG modes from $p = 1$ to $p = 4$. Since the resonator used was stable and conforms to the ABCD matrix [30], the theoretical predictions can be applied, where the generated LG $_p$ mode width, w_p , follow closely the theory given in Eq. 3.2 in Chpt. 3. The results are shown in Fig. 4.5b.

The output power from the laser resonator is defined to be linearly proportional to the mode volume, V_p , where the volume of the p^{th} radial mode is given as:

$$V_p = V_0 M^2 \left(1 + \frac{l_0^2}{3z_r^2} \right), \quad (4.2)$$

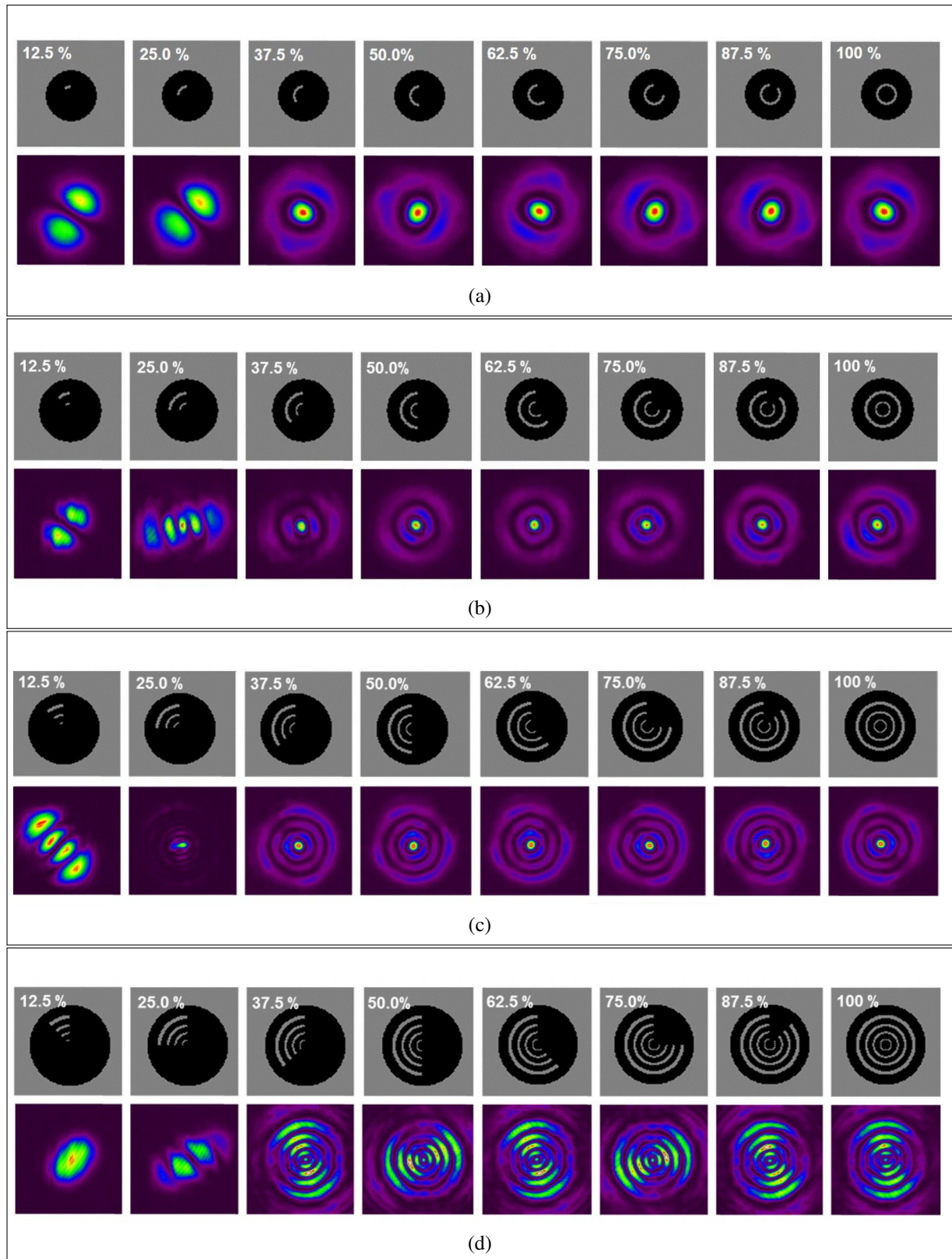


Figure 4.4 Top row of (a)-(d) shows computer-generated digital holograms encoded as pixelated gray-scale images where the completeness of the p absorbing ring varies from 12.5% to 100% for $p = 1 - 4$. Bottom row of (a)-(d) shows the generated intensity profiles from the laser for the different corresponding p -absorbing ring digital holograms.

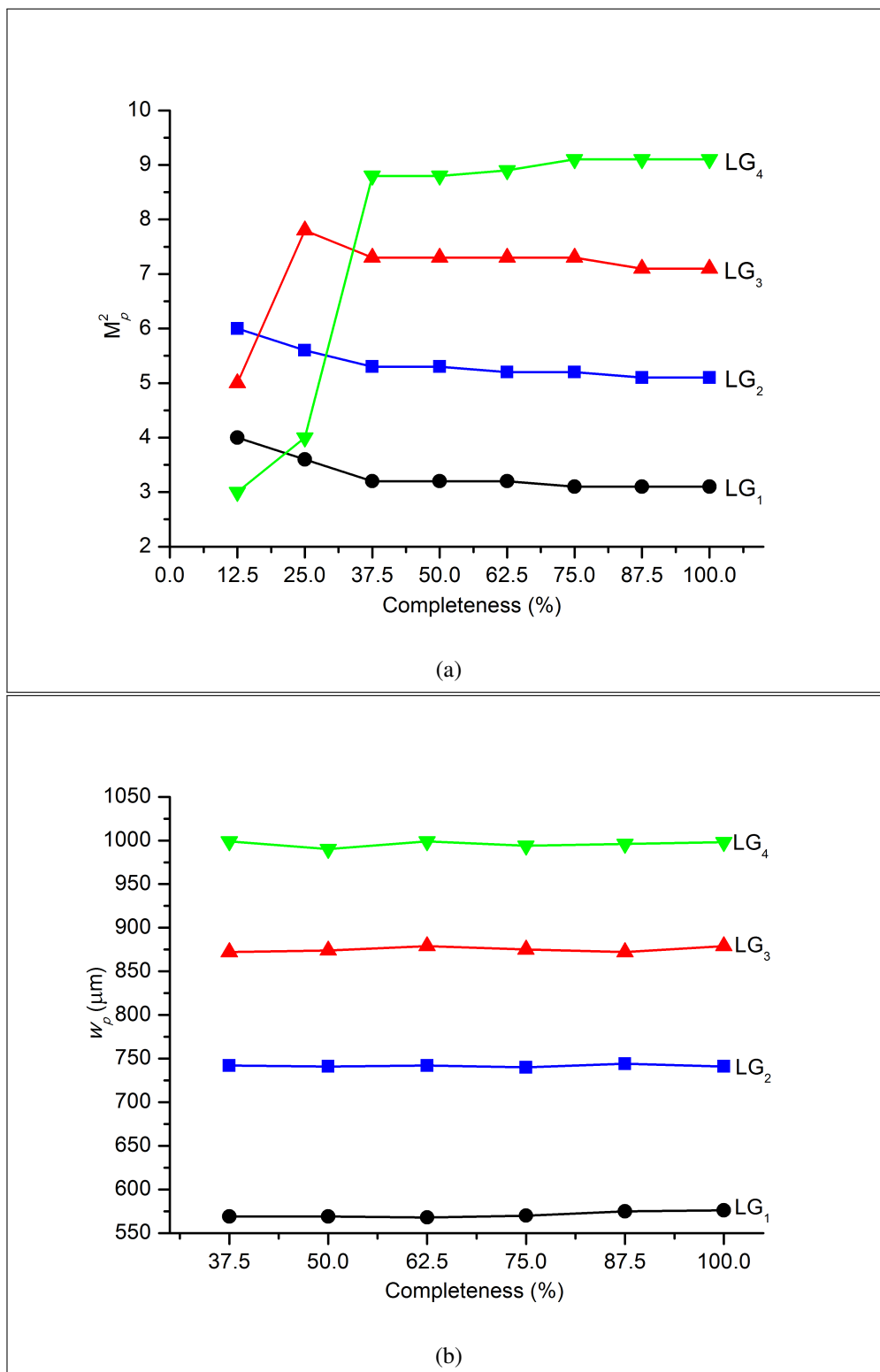


Figure 4.5 (a) Beam propagation factor, M_p^2 , and (b) beam radius, w_p , at the output coupler for LG modes of $p = 1 - 4$ with varying completeness of the absorbing rings.

where l_0^2 is the length of the gain medium and V_0 is the mode volume of the Gaussian mode. From Eq. 4.2 it is clear that the mode volume, V_p , is directly proportional to the propagation factor, M^2 , of the fundamental LG_p mode. Therefore we can deduce that the output power extracted from the laser is also directly proportional to both the mode volume, V_p , and the propagation factor, M^2 , of the oscillating LG_p mode [56, 85].

The experimental results are shown in Fig. 4.6a confirm that when the ring is less than 37.5% complete, the laser resonator produces unexpected laser beams. This causes the slope efficiency of the laser to be “random”. In addition, once the completeness of the ring is greater than or equal to 37.5%, the laser resonator begins producing the expected single fundamental LG_p laser mode of $p = 1 - 4$. This is evident in Fig. 4.6a, where the slope efficiency of the laser is constant for each LG_p laser mode. Furthermore, the threshold of the laser resonator with respect to the pump power, p_ε , and the absorbed pump power, $p_{abs,\varepsilon}$, can be mathematically described as follows: [12]:

$$P_\varepsilon = \frac{\pi h \nu_\varepsilon}{4 \eta_{(\varepsilon-q)} \sigma_{em} \tau} (w_p^2 + w_\varepsilon^2) (T + L) \quad \text{and}; \quad (4.3)$$

$$P_{abs,\varepsilon} = \eta_{(\varepsilon-q)} \frac{\nu_l T + L}{\nu_\varepsilon T}, \quad \text{for } w_\varepsilon < w_p, \quad (4.4)$$

where w_p and w_ε are the laser LG_p mode radius and pump radius; ν_l and ν_ε are the laser and pump frequencies; σ_{em} is the effective stimulated-emission cross-section; τ is the lifetime of the laser transition; $\eta_{(\varepsilon-q)}$ is the pump quantum efficiency (i.e. the average number of ions in the upper manifold created per absorbed pump photon); T is the output coupler transmission; and L is the laser resonator losses caused by scattering, absorbing rings, and aberrations due to thermal effects. The laser resonator absorbing rings constituted the only major resonator loss, L , that we were interested in studying.

The slope efficiency, η_p , of the laser resonator for each LG_p mode generated is given as:

$$\eta_p = \eta_{(\varepsilon-q)} \frac{\nu_l}{\nu_\varepsilon}. \quad (4.5)$$

Using Eq. 4.4, then η_p can be represented as:

$$\eta_p = P_{abs,\varepsilon} \frac{T}{T + L}. \quad (4.6)$$

It is important to note that Eq. 4.3 and Eq. 4.4 are only valid for $T \ll 1$ and $L \ll 1$, otherwise T must be replaced with $-\ln(1 - T)$, and $L = \sum L_i$, where L_i are all the separate cavity losses other than the output coupler (which in our case will be absorbing ring losses, δ , for each LG_p

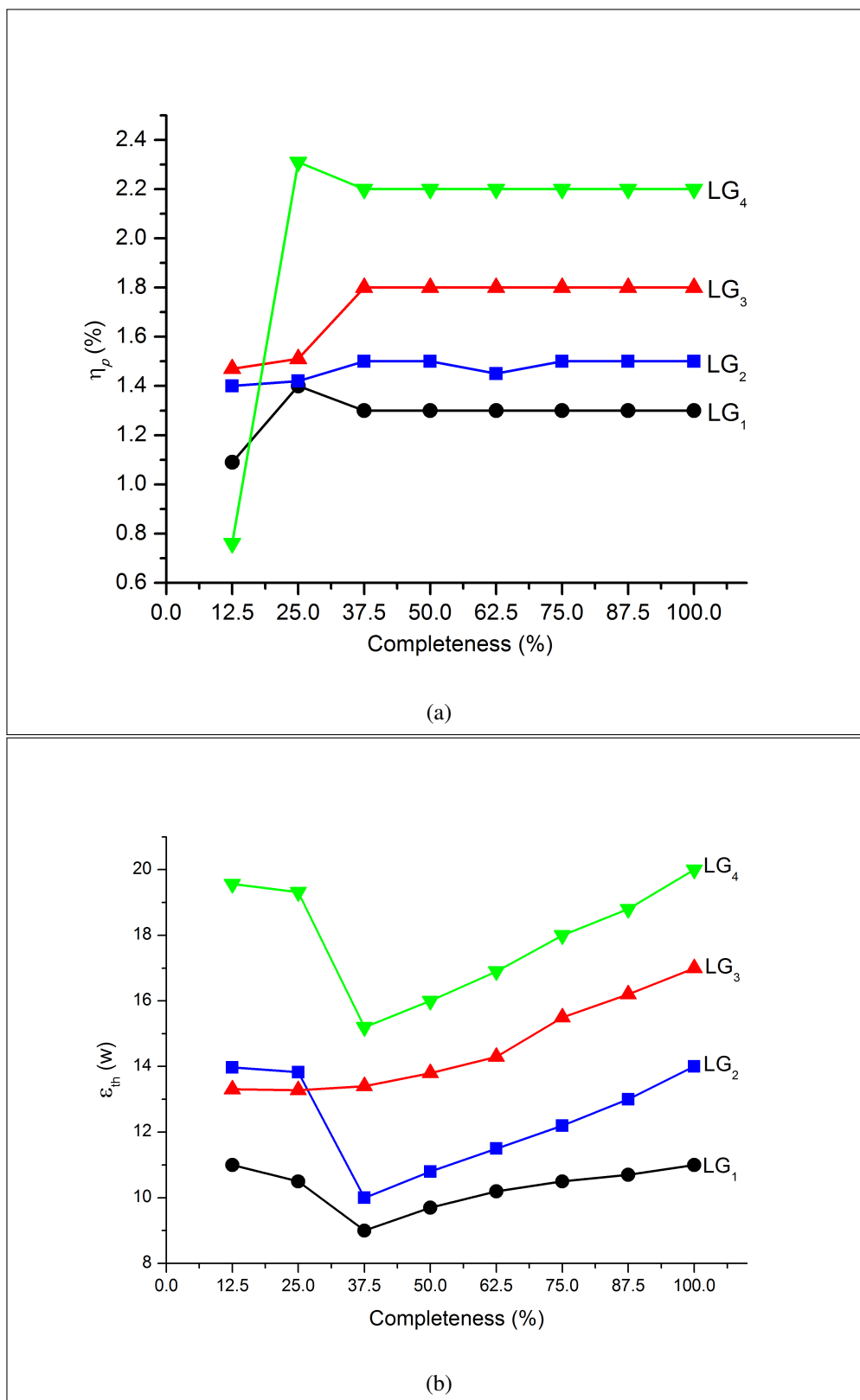


Figure 4.6 The figure shows the slope efficiency, (a) η_p , and the pump power threshold, (b) ε_p , for LG_p modes of $p = 1 - 4$ with varying completeness of the absorbing circular ring.

mode. However, up to few percent loss the transmission approximations are very good, i.e. ($-\ln(1 - T) = 0.051$ for $T = 0.050$ and $-\ln(1 - T) = 0.105$ for $T = 0.100$). Therefore, when inserting Eq. 4.6 into Eq. 4.3 and Eq. 4.4 and solving for slope efficiency, η_p , the equation will become:

$$\eta_p = \frac{\pi h \nu_l}{4 \sigma_{em} \tau} \times \frac{(w_p^2 + w_\varepsilon^2)}{P_\varepsilon} \times (T + L). \quad (4.7)$$

From Eq. 4.7, it is also clear that the slope efficiency, η_p , is directly proportional to the LG_p mode volume, V_p ($V_p = \pi w_p^2 l_0$), since the absorbing ring losses L and the pump power, p_ε , cancel one another for each LG_p amplitude mask as they always increase simultaneously. This effectively makes the slope efficiency, η_p , to be constant (see Fig. 4.6a) for various ring completenesses, from ring completeness equal to or greater than $\approx 37.5\%$, when the laser resonator is generating LG_p modes.

The graph in Fig. 4.6b clearly shows that the pump threshold, ε_{th} , is “random” for absorbing rings that are less than $\approx 37.5\%$ complete, since the laser resonator was generating non-expected LG_p laser beams. At a ring completeness of $\approx 37.5\%$ onwards, the pump threshold, ε_{th} , is shown to increase linearly as the absorbing ring completeness or losses increase, for each LG_p mode. The lowest pump threshold, ε_{th} , for the generation of LG_p modes is shown to occur when the completeness of the absorbing rings is at $\approx 37.5\%$ and this is $\alpha = 1.3 = 0.81\pi/2$ (see Fig. 4.6b). These results agree 93% (1.3 rad/1.4 rad) with the simulation shown in Fig. 4.3b where the simulation shows that the laser starts operating on high LG_p mode when $\alpha > 1.4$ rad ($0.88\pi/2$).

4.6 Summary

Forcing the fundamental mode of a laser to be an LG_p mode can be obtained by inserting a mask made up of p -absorbing rings having radii coinciding with the zeros of the desired radial Laguerre-Gaussian mode. However, doing that increases the loss level and the laser threshold. In this work, we have experimentally demonstrated that it is possible to reduce the additional losses by using a mask having a completeness equal or greater than 37.5%. The better results in terms of the laser threshold are obtained for a completeness of 37.5%. We have successfully demonstrated that high radial order Laguerre-Gaussian, LG_p , modes can be generated using circular absorbing rings that are $\approx 37.5\%$ to 100% complete. The results also indicate that we can digitally excite high radial order LG_p modes with the lowest excitation pump threshold, ε_{th} , when the absorbing rings are $\approx 37.5\%$ complete or when $\alpha = 1.3 = 0.81\pi/2$, while

maintaining all the other resonator characteristics such as the generated LG_p mode size, w_p , beam quality factor, M_p^2 , and the slope efficiency, η_p , of the laser.

Chapter 5

Discrete excitation of mode pulses using a diode-pumped solid-state digital laser

In this chapter, we report on how we efficiently generated on-demand laser modes using a single-mode solid-state digital laser. Laguerre-Gaussian mode of azimuthal order $l=(0, 1, 2)$ with zero radial order ($p = 0$) was generated and discretely pulsed using a digital hologram that acted as a “Q-Switch”. Pulses of duration ≈ 200 ns and intensities as high as ≈ 1 mW with repetition speed of 60 Hz were produced at $1 \mu\text{m}$. The maximum peak power conversion efficiency measured was $\approx 1.3\%$.

5.1 Introduction

Pulse-pumped excitation, Q-switching and mode locking are three of the general methods of generating laser pulses by modulating the resonator losses [86, 87, 88, 89]. However, for real-world application, the latter two – Q-switching and mode locking – are the preferred methods of generating controlled laser pulses [90, 91]. The pulses may be long and/or short, depending on the method used. Q-switching is the method opted for when one wishes to obtain laser pulses in nanosecond order. It can be obtained by various methods, ranging from active Q-switching using an acoustic-optic shutter, to passive Q-switching using saturable absorbers [92, 93, 94]. However, Q-switched pulses are generally limited to the order of a few nanoseconds, due to finite cavity lifetime [95, 96]. In order to obtain shorter pulses, mode-locking techniques can be used [96]. Mode locking can be achieved by various methods such as active mode locking, passive mode locking and Kerr lens mode locking [97, 98, 99].

One must also note that the pulse energy is equal to the average power over the repetition rate. High pulse energy can be achieved by decreasing the rate of pulses. For example, a cell

can be destroyed if it is heated over a very short period, whereas injecting the energy steadily would allow for the heat to be absorbed into the majority of the cell parts over a period of years. Moreover, another application utilises the peak pulse power to obtain a non-linear optical effect. In fact, many pulse lasers are used for the ablation of biological, metallic, ceramic, and semiconducting materials [100, 101].

Generally, pulsed lasers use a Gaussian beam profile, even though for mode locking a high number of modes can oscillate inside the cavity, and a certain number of modes can lase. However, the lasing mode will not be discrete. We will be showing how to lase a discrete mode and pulse it at the same time, or how to pulse different modes in a single-mode solid-state laser resonator. Section 5.2 deals with the general concept associated with laser pulses, especially Q-switched pulses. Our method of pulsing resembles the Q-switching method. Section 5.3 will highlight the method we used to generate Laguerre-Gaussian beams and introduce the concept of pulsing the modes. Finally, we will show and interpret our results in Sec. 5.4, and draw conclusions in Sec. 5.5 based on an interpretation of our results.

5.2 Q-switching using a spatial light modulator

As stated in Sec. 5.1, there are different methods of achieving pulse lasers. In this section, the focus is more on active Q-switching, since our method of using digital holograms is similar to Q-switching. However, due to the speed of the SLM, the width of pulses will not reach nanoseconds, but only milliseconds. In this section we may answer the following questions:

1. How does active Q-switching work?
2. What is needed for Q-switching?

First, we need to understand the quality factor Q of a resonator. The quality factor is defined as the ratio of the frequency of a mode to its width and it can be mathematically written as follows:

$$\begin{aligned}
 Q &= 2\pi\mu\tau_c \\
 &= \frac{2\pi\mu}{c\gamma} \\
 &= \frac{2\pi\mu}{c\sigma N_{2,th}}.
 \end{aligned} \tag{5.1}$$

Equation 5.1 shows that the threshold population inversion $N_{2,th}$ is inversely proportional to Q . Furthermore, active Q-switching is required in order to be able to switch so fast that the

population inversion remains the same. The Q of the laser cavity can be changed by introducing a shutter inside the laser resonator, for instance, an electro-optic shutter or an acoustic-optic shutter.

When we look firstly at how the electro-optic shutter works, it is clear that two optical elements may be used, namely a pocket cell and polarizer. The polarizer can be oriented to allow transmissions of only one polarisation. This is similar to our case where we used an SLM, and we used a Brewster window to select the correct polarisation to match the SLM polarisation. The second element that was used was the pocket cell that rotates the polarisation of the light when a voltage is applied. We used a gray-scale image on our SLM to perform this function. The Q-switching process took place when a high voltage was applied, and the quick setting of the applied voltage to zero switched Q from low to high. This was similar to our technique, where we applied a certain voltage to the liquid crystals (LC) of the SLM to do Q-switching.

Q-switching can also be achieved by using an acoustic-optic shutter. For this method, a transparent crystal is introduced into the resonator cavity. Acoustic waves at high intensity are generated and they create a periodic variation of the refractive index. In addition, the light gets diffracted, and the resonator cavity loss decreases Q . An SLM can also be used to create an unstable laser resonator, which will stop lasing since Q will be very low.

5.3 Methodology

In order to generate on-demand modes and discretely pulse them, we used the DPSSDL shown in Fig. 5.1. The stable DPSSDL had an effective length of 180 mm, with the circular aperture digitally encoded directly to the computer-generated hologram that was SLM. The SLM was used as both a curved ($R = 200$ mm) end mirror and as a mask to generate – intra-cavity – on-demand modes.

The laser beam from Fig. 5.1 is transmitted using output coupler mirror M_2 , and the 50:50 beam splitter (BS) was used to direct the beam to the CCD Camera and Oscilloscope. The output coupler mirror (M_1) had a radius of curvature of $R = \infty$. The digital oscilloscope (Tektronix-TBS1000) was used to record the signal of the on-demand-generated laser modes, in both continuous and pulsing mode.

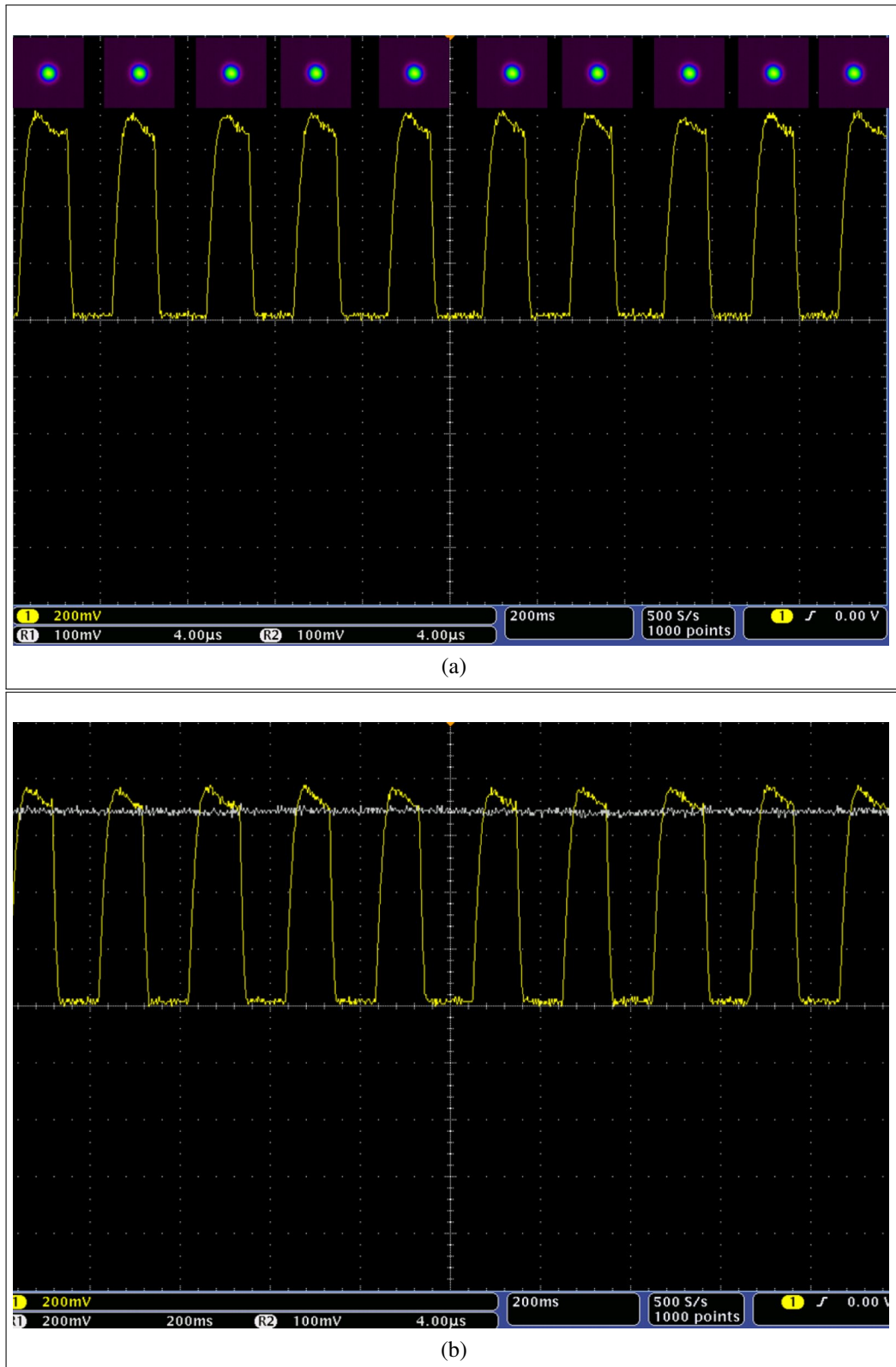


Figure 5.2 (a) Oscilloscope image displaying pulsed voltages for Gaussian mode in 200 ms. (b) Oscilloscope image displaying pulsed and continuous (solid straight line) voltage for Gaussian mode in 200 ms.

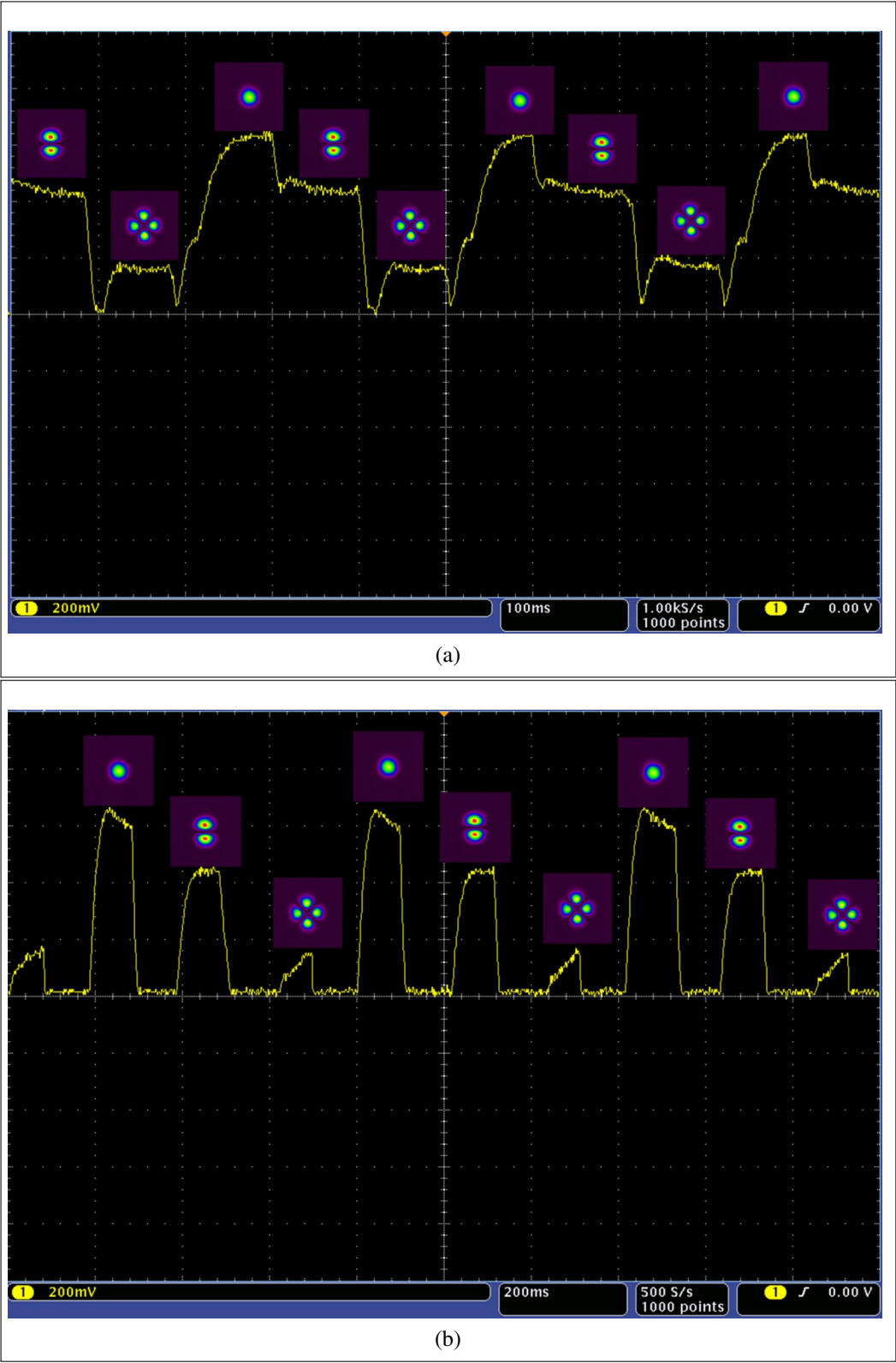


Figure 5.3 (a) Oscilloscope image displaying pulse voltage for on-demand modes in 200 ms, continuously. (b) Oscilloscope image displaying pulse voltage for on-demand modes in 200 ms, discretely.

We decreased Q of the laser cavity between each mode generated after 200 ms, as explained above. The results that were observed from the oscilloscope are shown in Fig. 5.3b and they confirm that we can discretely generate a pulse for on-demand modes using the digital laser.

5.5 Summary

We successfully developed a laser that is able to generate on-demand laser pulses of various shapes. The laser pulses generated for the Laguerre-Gaussian mode of radial order $p=0$ and azimuthal-order $l=(0, 1, 2)$ had a pulse length of 200 ms and repetition rate of 60 Hz. The Gaussian mode had an average power of 1.36 mW, and pulse energy of 6.8 μJ . According to the results shown in Fig. 5.3b the azimuthal order modes have lower average power per pulse compared to Gaussian mode. However, results shown in Fig. 3.8b show that radial order modes have higher output power.

Chapter 6

Solid-state digital laser mode amplification using extra-cavity Nd: YAG amplifier

In this chapter, we demonstrate experimentally how the laser output power of the higher-order $LG_{p,l}$ modes generated from a digital laser is amplified by using an extra-cavity Nd: YAG amplifier. The DPSSDL generates fundamental higher-order modes by encoding and displaying digital holograms on a phase-only SLM that acts as an end mirror of the laser resonator cavity. The Nd:YAG master oscillator power amplifier (MOPA) was configured to boost the output power of the laser mode, since the laser mode would experience higher gain, which would translate to increasing the power of the mode when it is transmitted through the MOPA. Amplification of as high as 42% was realised for $LG_{2,0}$, and only 9% was realised for $LG_{2,2}$ due to pump mismatch.

6.1 Introduction

As previously explained DPSSDL has attracted widespread attention due to its ability to generate on-demand laser modes [22, 77, 78]. The diode laser is a preferred pump for high-power lasers, due to its better frequency stability, higher efficiency, higher brightness and long operational lifetimes [12, 30]. Diode-pumped solid-state lasers (DPSSL) are usually compact, more stable, and have a lower cost, which makes them more practical for a larger number of applications [30, 56]. Higher-order radial Laguerre-Gaussian ($LG_{p,0}$) modes have applications in industry such as in medicine, the military and communications [69, 71, 73].

DPSSDLs have power limitations since the end mirror of the resonator is a spatial light modulator (SLM) [22]. The lasers use this SLM in order to avoid using intra-cavity phase elements (IPEs) to generate modes, as it is inconvenient to use IPEs when the mode order has to be changed. Due to the SLM's efficiency and low damage threshold, the output beam of the digital laser is also restricted in power. A need was consequently identified to increase the power output of the beam. In this work, we made use of diode-pumped Nd: YAG crystal to amplify the output beam. The gain medium Nd: YAG rod crystal that is 1.1% doped, has an energy storage capacity higher than other solid-state crystals. The Nd: YAG crystal operates at 1064 nm and, pumped at 808 nm, it was sufficiently doped to ensure maximum absorption. We planned to selectively excite higher-order $LG_{p,l}$ laser mode [56], for radial order (p) and azimuthal order (l), $p, l=0$ to 2, using a DPSSDL. Furthermore, we sought to amplify the generated mode through a diode-pumped Nd: YAG crystal. The amplified laser mode would have the same wavelength as the seed laser mode (1064 nm). The output power would be compared to the input power of the seed laser, which would allow us to determine the amplification percentage [102].

6.2 Experimental setup and methodology

The SLM of the DPSSDL shown in Fig. 6.1 displayed a CGH shown in Fig. 6.2 which represent a digital curvature of 400 mm + desired on-demand mode. The laser beam transmitted out of the cavity through an output coupler mirror (M_2 partially reflecting 90% and transmitting 10% of 1064 nm) was relay-imaged to the external Nd:YAG crystal that was used as an amplifier. The external Nd:YAG crystal have the same properties as the one use for the laser and the pumping system is the same. In addition, a beam profiler was used to observe the amplified $LG_{p,l}$ beam and a power meter was used to measure the amplified $LG_{p,l}$ beam power.

6.3 Results and discussion

The transverse intensity distribution profiles of input seed laser $LG_{p,l}$ modes are shown in Fig. 6.3a. In comparison, the intensity distribution profiles for amplified modes are illustrated in Fig. 6.3b. These profiles show a high degree of similarity, and they are in good agreement with the Fig. 1.5a shown in Chpt. 1.

Furthermore, we studied the operational parameters of the Nd: YAG amplifier such as the laser diode power dependence on slope efficiency and amplification percentage. The results are shown in Fig. 6.4a, Fig. 6.4b and Fig. 6.5b. The highest amplification was experienced at 60

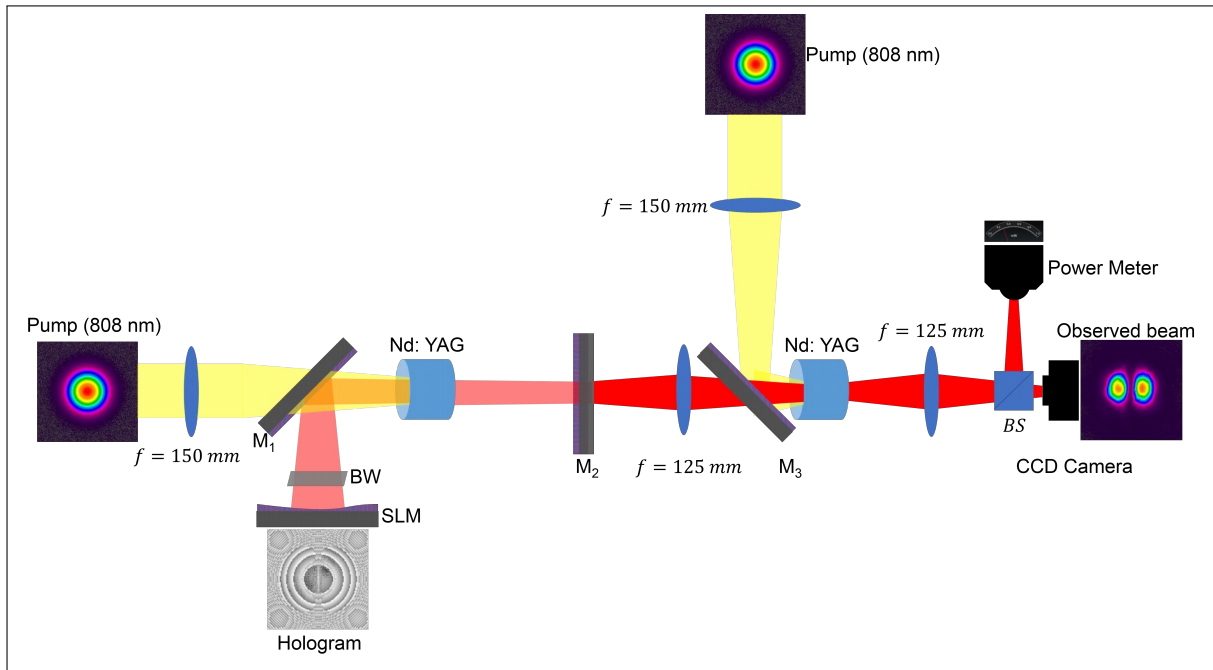


Figure 6.1 Schematic of DPSSDL with a single-pass Nd: YAG amplifier.

W (shown by the red rectangle) in Fig. 6.4a, thus we used 60 W pump power for all our seed beams.

6.4 Summary

In this chapter, we have shown the amplified higher-order $LG_{p,l}$ laser using an extra-cavity Nd: YAG amplifier (single pass), by matching the pump size and the seed laser modes. The highest power amplification was 42% for $LG_{2,0}$. For $LG_{2,2}$, the seed laser was mismatched to the pump, and as a result, the intensity profile of the seed laser differed from that of the amplified seed laser mode to some degree. In future, we will use seed laser beams that allow for larger extraction of the power and convert them to a Gaussian mode for higher brightness lasers.

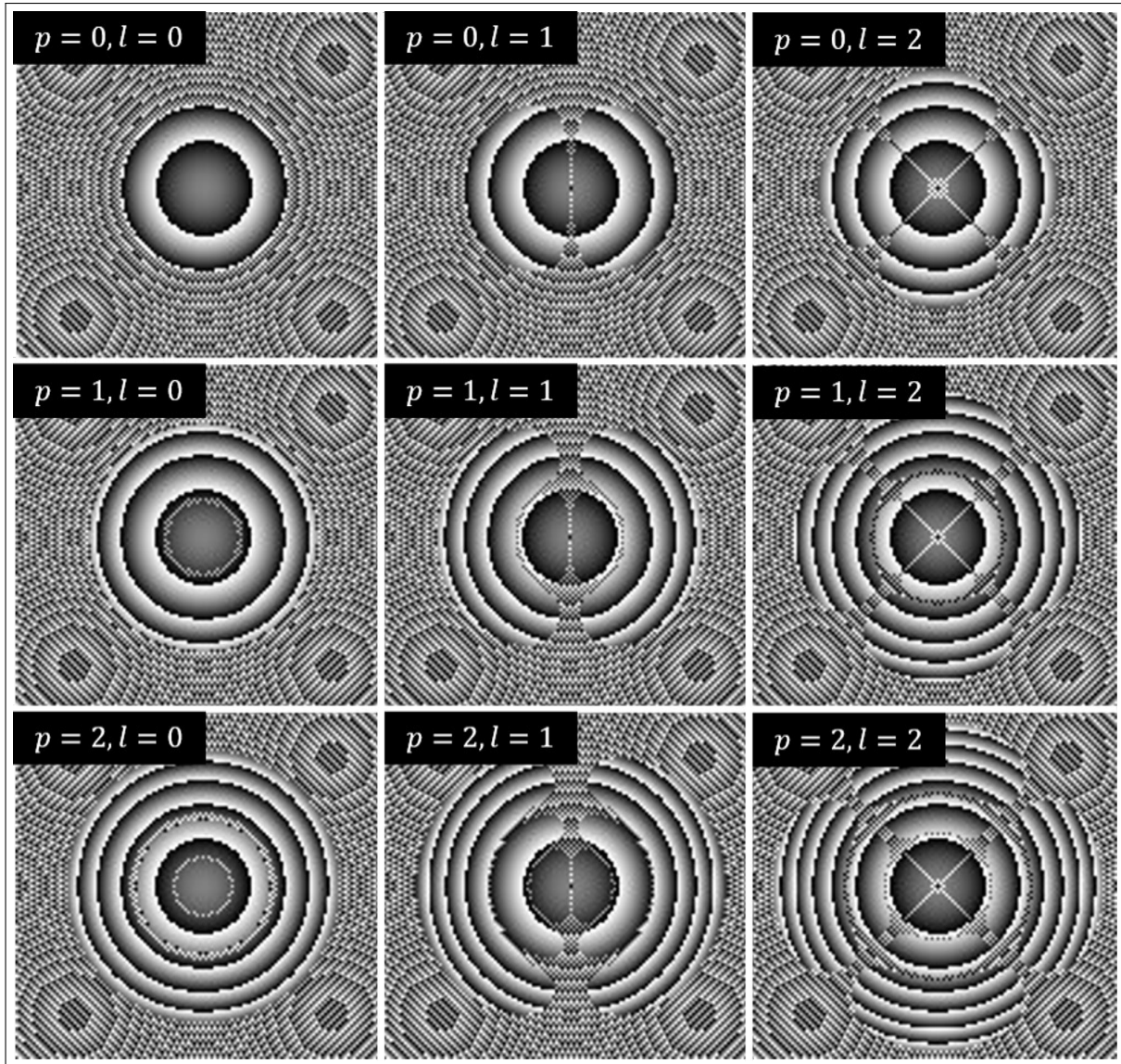


Figure 6.2 Computer-generated holograms (CGH) encoded as pixelated gray-scale for generating $LG_{p,l}$. Rows represent $p=0$ to 2, and columns represent $l=0$ to 2.

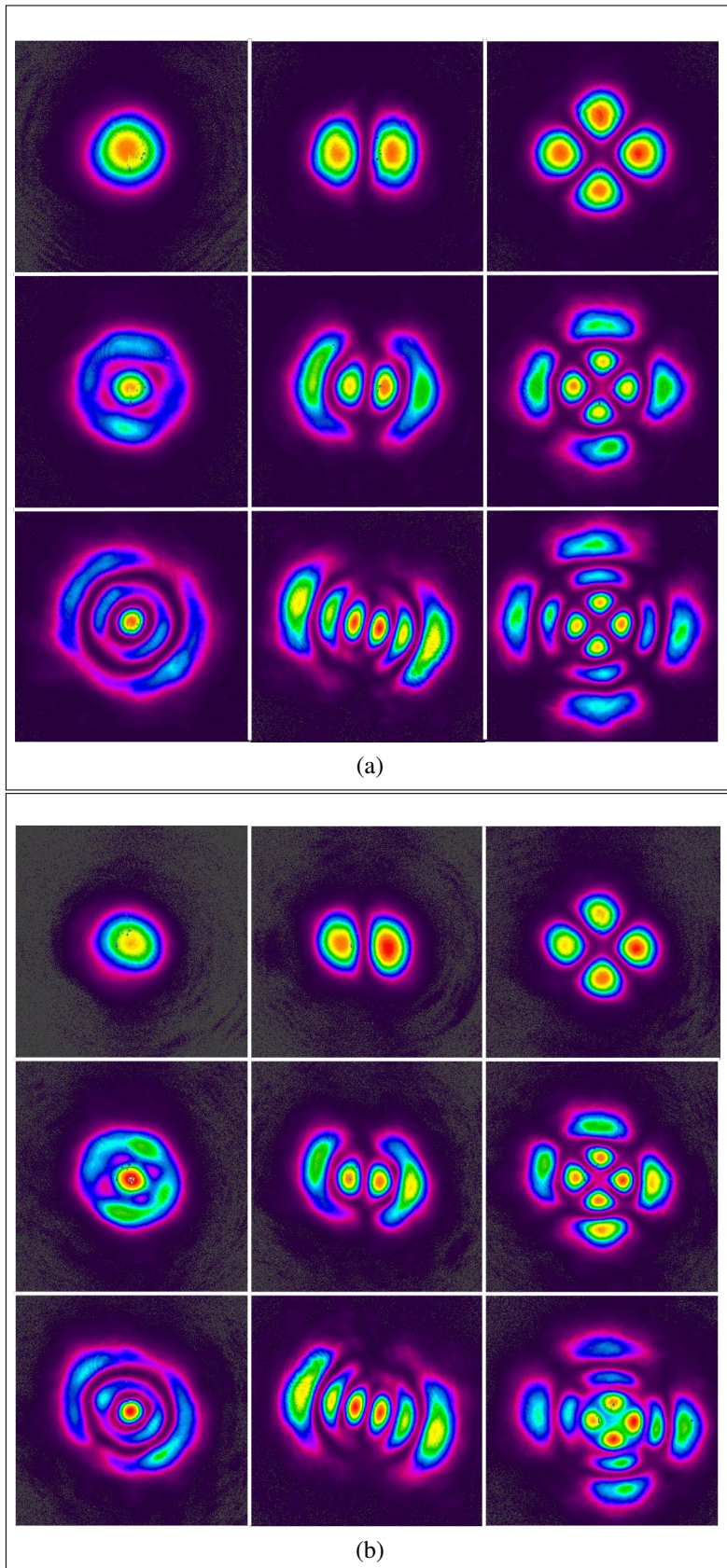


Figure 6.3 (a) Observed intensity profiles of the seeded beams focused on the external Nd:YAG laser crystal. (b) Observed intensity profile of the amplified beams. Intensity profiles were recorded using a CCD camera; rows represent LG modes of order $p=0$ to 2 , and columns represent LG modes of order $l=0$ to 2 .

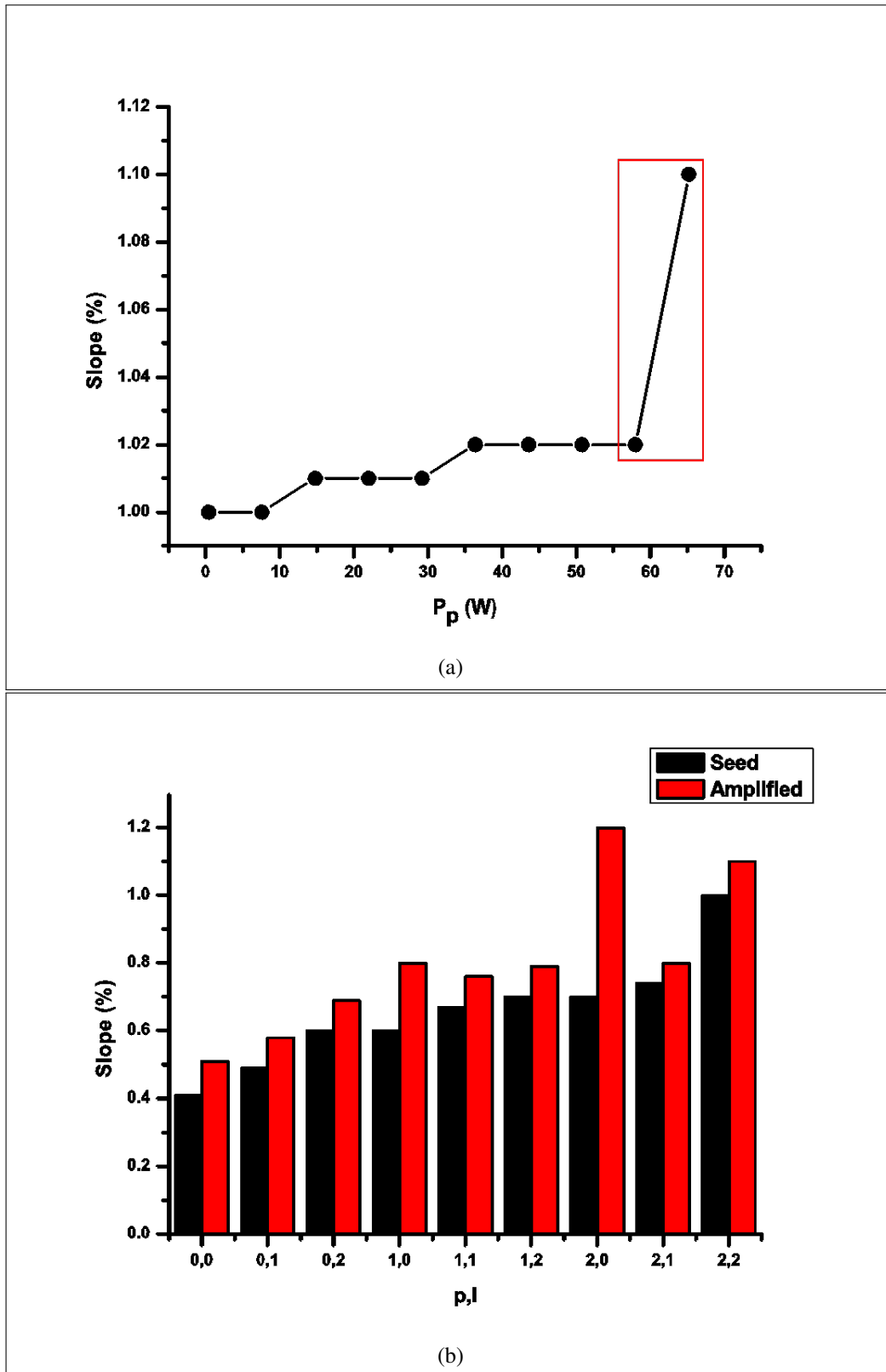


Figure 6.4 (a) The graph of the slope efficiency versus pump power to determine the pump power (shown by red rectangle) that should be used for amplification. (b) The graph of the slope efficiency graph versus the mode order p, l amplified using a 60 W pump power.

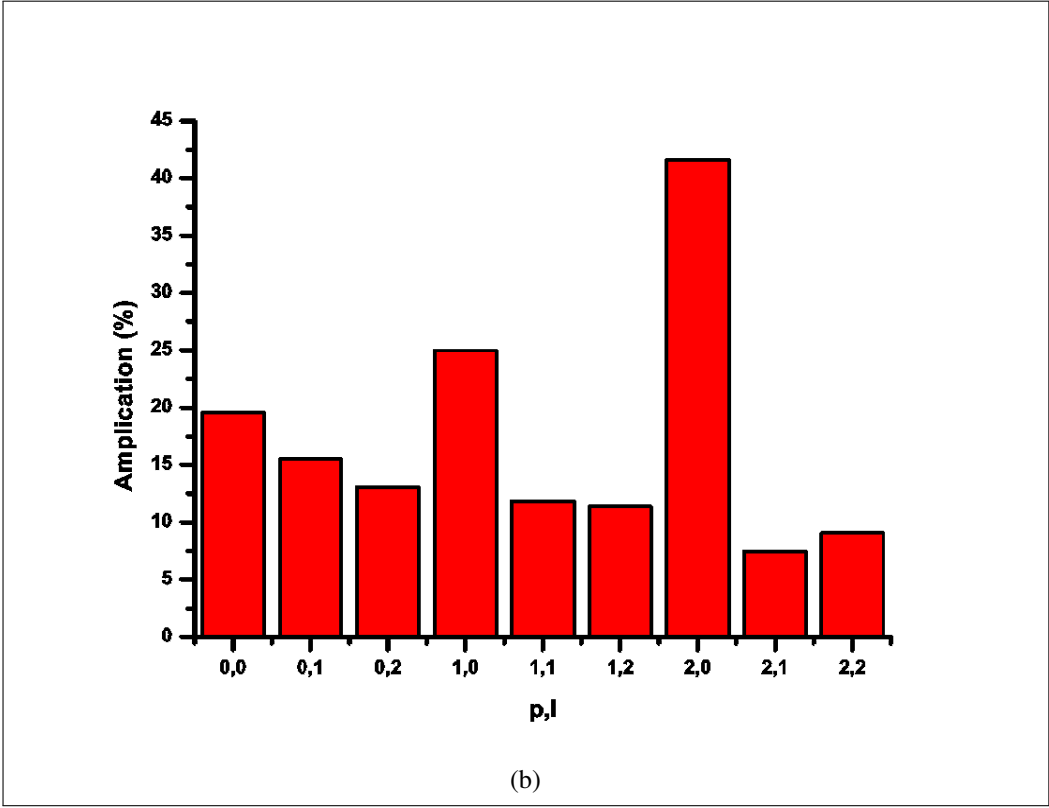
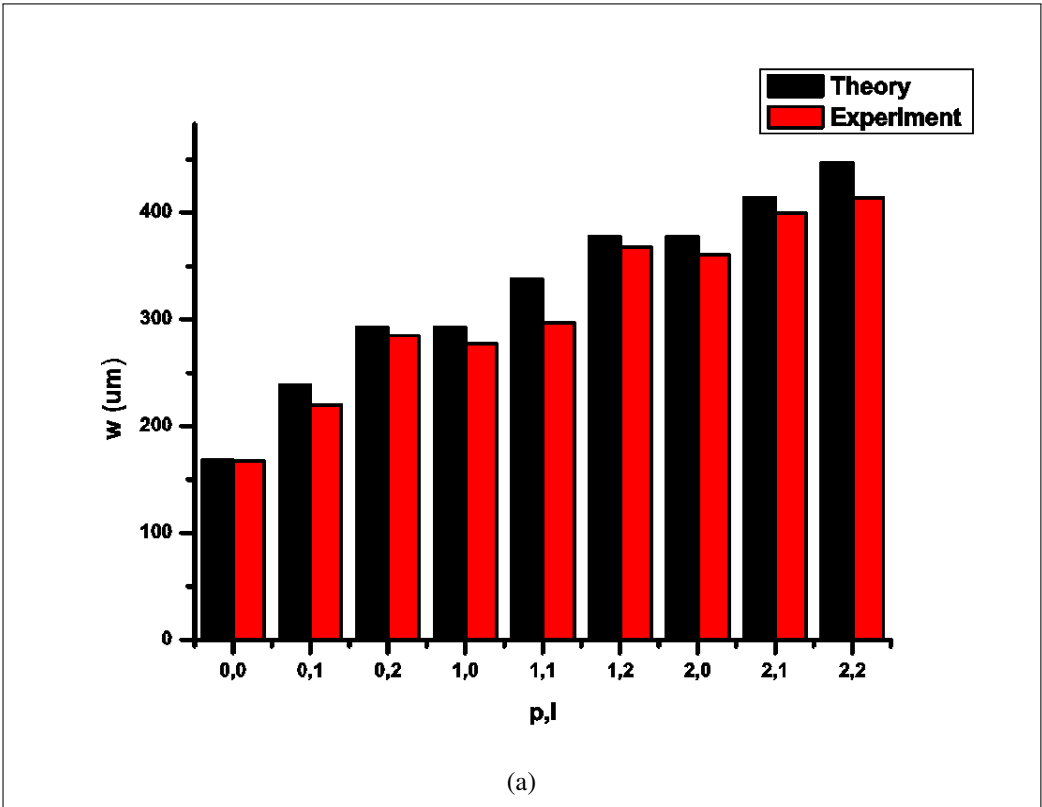


Figure 6.5 (a) The graph of the $LG_{p,l}$ beam width versus the mode order p,l . (b) The graph showing the amplification percentage against the mode order p,l .

Chapter 7

Intracavity second harmonic generation for higher-order modes

In this final technical chapter, higher-order modes were generated using an DPSSDL operating at 532 nm (visible) wavelength. We inserted a non-linear crystal inside the diode-end-pumped solid-state digital laser operating at 1064 nm (Near-IR) and used a non-linear crystal consisting of potassium titanyl phosphate ($KTiOPO_4$ or KTP). The KTP was pumped using the higher-order modes generated by the 1064 nm solid-state digital laser. We generated Laguerre-Gaussian modes and Hermite-Gaussian modes inside a cavity. The laser modes were characterised by analysing the intensity distribution. To the best of our knowledge, this is the first laser to generate higher-order modes inside the cavity at the visible (green) wavelength of 532 nm.

7.1 Introduction

Green lasers generated by means of frequency doubling (FD) – also known as second harmonic generation (SHG) technique – have been used extensively in laser detection, laser ranging, ocean exploration, medicine and applications in the military [103, 104, 105, 106]. We made use of the newly developed diode-end-pumped solid-state laser that operates at 1064 nm [60], to generate a 2nd harmonic wave from it. Nonlinear optics was used to explore the birefringence of the potassium titanyl phosphate (KTP) crystal, by inserting the nonlinear medium inside the laser resonator and pumping it with 1064 nm. Frequency doubling or second harmonic generation using KTP enables one to convert the 1064 nm output from Nd: YAG lasers to visible light, with wavelengths of 532 nm (green) [107, 108]. Other media that are commonly used apart from KTP (potassium titanyl phosphate) are BBO (β -barium borate), KDP (potassium dihydrogen phosphate), $LiNbO_3$ (lithium niobate), and LiB_3O_5 (lithium triborate) [109, 110].

These mediums have the necessary properties such as being strongly birefringent, being transparent for both the impinging laser light and the frequency-doubled wavelength, having specific crystal symmetry, as well as having a high damage threshold [111, 112, 113].

One of the main reasons that we chose KTP crystal as our crystal of choice for frequency conversion was the fact that the crystal is a superior nonlinear optical material [114]. For a standard diode-end-pumped Nd-YAG laser of 1064 nm wavelength, the second harmonic generation effect of KTP is far better, compared to any other type of crystal [115].

As previously explained that DPSSDL contains an intracavity phase-SLM that performs as an end mirror of the main laser resonator cavity. In addition, we inserted the KTP that was pumped by the oscillating mode inside the cavity operating at a laser mode size of 1064 nm. The laser mode size was taken into account for pumping the KTP crystal to match the active medium of the KTP. We digitally loaded a gray-scale (0 to 255) hologram image that represented a digital mask of Laguerre-Gaussian [85] and Hermite-Gaussian modes [60] of order $p, l=0, 1, 2$ and $m, n=0, 1, 2$, respectively.

The following section briefly covers basic theories related to intracavity frequency doubling or second harmonic generation.

7.2 The second harmonic generation from 1064 nm to 532 nm

Frequency doubling is generated by the second susceptibility, if one considers a vector field $\mathbf{E} = (E_x, E_y, E_z)$. The second order dielectric polarisation $\mathbf{P}^{(2)}$ can be written as follows:

$$M = \begin{bmatrix} P_x^2 \\ P_y^2 \\ P_z^2 \end{bmatrix} = \begin{bmatrix} d_{11} & d_{12} & d_{13} & d_{14} \\ d_{21} & d_{22} & d_{23} & d_{24} \\ d_{31} & d_{32} & d_{33} & d_{34} \end{bmatrix} \begin{bmatrix} E_x^2 \\ E_y^2 \\ E_z^2 \\ 2E_yE_z \\ 2E_xE_z \\ 2E_xE_y \end{bmatrix}. \quad (7.1)$$

The dielectric constant is $\epsilon_0 = 8.85 \times 10^{-12} \text{As}/(\text{Vm})$, and d_{ij} is known as nonlinearity coefficient. Furthermore, for loss-free materials, only 10 out of 18 nonlinearity coefficients are independent, but depending on the symmetry of the crystal. The number of the independent coefficients is considerably reduced so that most frequency-doubling crystals have only two or three independents, and non-zero coefficients remains. In the case of KTP, the remaining

nonlinearity coefficients are shown in Tab. 7.1: If a field $\mathbf{E}^{(1)}$ at the fundamental frequency ω_1

Table 7.1 Non-zero nonlinearity coefficient d_{mn} for KTP.

d_{mn} ($\times 10^{-12}$ m/V)	wavelength λ (nm)
$d_{15} = d_{31} = \pm(6.5 \pm 0.5)$	1064
$d_{24} = d_{32} = \pm(5.0 \pm 0.5)$	1064
$d_{33} = 13.8$	1064

is incident onto the crystal, a field $\mathbf{E}^{(2)}$ at the second harmonic frequency $\omega_2 = 2\omega_1$ is generated at the expense of the fundamental wave. If we consider the propagation in the z -direction only, the transformation of the fields and electric polarisation into the complex notations is as follows:

$$\mathbf{E}^{(1)} = \frac{1}{2} \left(\mathbf{A}^{(1)} e^{i(\omega_1 t - k_1 z)} + C \right) \quad (7.2)$$

$$\mathbf{P}^{(1)} = \frac{1}{2} \left(\mathbf{P}_c^{(1)} + \mathbf{P}_c^{*(1)} \right). \quad (7.3)$$

The electric field \mathbf{P} acts as the source for both fields $\mathbf{E}^{(1)}$ and $\mathbf{E}^{(2)}$, which means that the propagation of each wave is described by the following wave equation:

$$\frac{\delta^2 \mathbf{E}^{(1)}}{\delta z^2} - \frac{1}{c^2} \frac{\delta^2 \mathbf{E}^{(2)}}{\delta t^2} = -\frac{1}{\epsilon_0} \frac{\delta^2 \mathbf{P}}{\delta t^2}, \quad (7.4)$$

where c_0 is the speed of light in the medium. The electric field polarisation \mathbf{P} is given by the sum of the field $\mathbf{E}^{(1)} + \mathbf{E}^{(2)}$. From Eq. 7.1, the amplitude \mathbf{A} for the second harmonic and the fundamental waves is as follows:

$$2ik_1 \frac{\delta A^{(1)}}{\delta z} = \frac{\omega_1^2}{\epsilon_0 c_0^2} P_c^{(2)}(\omega_1) e^{[i(k_1 z - \omega_1 t)]}, \quad (7.5)$$

$$2ik_2 \frac{\delta A^{(2)}}{\delta z} = \frac{\omega_2^2}{\epsilon_0 c_0^2} P_c^{(2)}(\omega_2) e^{[i(k_2 z - \omega_2 t)]}, \quad (7.6)$$

where $\mathbf{P}_c^2(\omega)$ represents the components of \mathbf{P}_c^2 that oscillate at the frequency ω . The amplitude A only increases significantly for $\Delta k = 0$, which is also known as phase matching. If we consider frequency doubling as the transformation of two photons with energy $\hbar\omega_1$ into one photon with energy $\hbar\omega_2$, the phase-matching condition is equivalent to the conservation of momentum:

$$\hbar k_1 + \hbar k_1 = \hbar k_2. \quad (7.7)$$

Since the wave number is related to the frequency and the speed of light using $k = \omega/c$, this relation means that the fundamental wave and the second harmonic wave must propagate with the same speed to avoid destructive interference of the second harmonic along the propagation directions. In addition, it is possible to split the fundamental wave into an extraordinary wave and an ordinary wave to attain phase matching.

For a nonlinear crystal with refractive index n , the intensities I_1 and I_2 of the fundamental wave and the second harmonic wave are given as follows:

$$I_2(z) = I_1(0) \tanh^2 \left[\sqrt{\frac{d_{eff}^2 \omega_1^2 I_1(0)}{n^3 2 \epsilon_0 c_0^3}} z \right] = I_1(0) \tanh^2 \left[\frac{z}{L} \right] \quad (7.8)$$

$$I_1(z) = I_1(0) - I_2(z), \quad (7.9)$$

where d_{eff} is the effective nonlinear coefficient. The conversion efficiency is defined as the fraction of the fundamental beam power that is converted into the second harmonic:

$$\eta_{SHG} = \tanh^2 \left[\frac{z}{L} \right], \quad (7.10)$$

where z is the crystal separation and L is the length of the crystal. From Eq. 7.10, at the distance $z = L$ about 57% of the fundamental beam power can be converted into the second harmonic beam. For a KTP crystal of length 10 mm, the fundamental beam intensity $I_1(0)$ that is required to convert 57% of the fundamental power into the second harmonic for the fundamental wavelength of 1064 nm is 0.026 GW/cm^2 , and the damage threshold is 0.8 GW/cm^2 [116, 117].

In circular symmetry, the power P_ω of the Gaussian beam with beam radius w and peak intensity I_0 is given by:

$$\begin{aligned} P_\omega &= I_0 2\pi \int_0^\infty e^{[-2(r/w)^2]} r dr \quad \text{when } w^2 > 0 \\ &= I_0 \pi \frac{w^2}{2}. \end{aligned} \quad (7.11)$$

It also must be noted that increasing the fundamental beam intensity will influence the mode structure. The structure will become less pronounced, since wings of the beam are converted more efficiently. This will result in the intensity of the second harmonic field not being Gaussian, thus the power can be expressed as follows:

$$P_{2\omega} = I_0 2\pi \int_0^\infty e^{[-2(r/w)^2]} \tanh^2 [z/Le^{(-r/w)}] r dr. \quad (7.12)$$

Due to the high intensity level of the beam inside the laser resonator compared to the beam intensity outside, the KTP crystal is placed inside the laser resonator to generate a doubled frequency, as shown in Fig.7.1. From the chosen mirrors in Fig. 7.1, the conversion efficiency

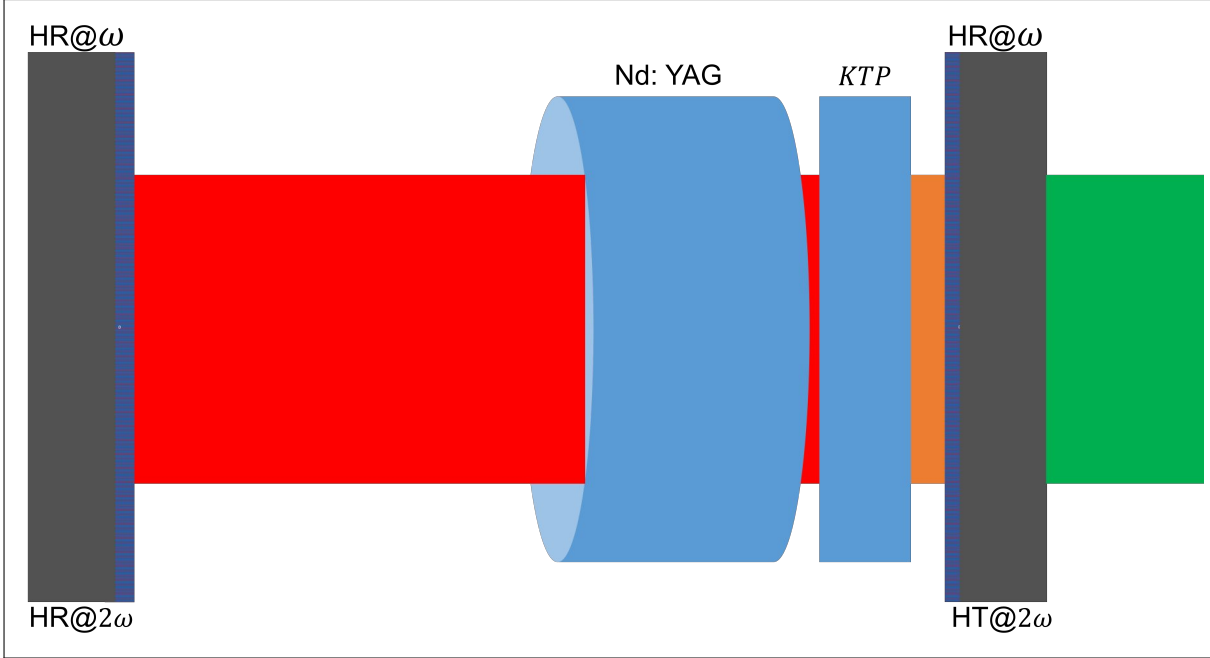


Figure 7.1 Laser resonator model for intra-cavity frequency doubling from 1064 nm to 532 nm.

of the KTP acts as the output coupling loss of the laser resonator. If one considers fundamental beam power, P_ω , incident on the KTP crystal and the power of the second harmonic wave generated to be $P_{2\omega}$, then the effect of the KTP crystal on the fundamental beam can be described by reflectance R as follows:

$$R = 1 - \frac{P_{2\omega}}{P_\omega} \quad (7.13)$$

$$= 1 - \eta_{SHG}. \quad (7.14)$$

Thus, the average intensity I of the fundamental beam inside the Nd: YAG crystal can be calculated using steady-state conditions per round trip [118]

$$R' = e^{[(2g_0l)/(1+2I/I_s)+2\alpha_0l]}, \quad (7.15)$$

where I_s is the saturated intensity, g_0l is the small-signal gain and the α_0l is the loss per transit. This steady-state condition is only valid for low signal gain and high reflectance R , because the z -dependence of the fundamental wave intensity inside the KTP crystal is neglected. The

second harmonic wave output power is given as follows:

$$P_{w\omega} = A_1 I_s \alpha_0 l \left(\sqrt{\frac{g_0 l}{\alpha_0 l}} - 1 \right), \quad (7.16)$$

where A_1 is the cross-sectional area of the fundamental beam in the Nd: YAG. One must also keep in mind that even if all the fundamental beam power is converted into the second harmonic, the conversion efficiency of the KTP crystal may be extremely low. Typically, for diode-pumped Nd: YAG lasers with efficiency 48%, the conversion efficiency can be as low as 9.5% [119].

7.3 Experimental methodology and concept

For the generation of high-order Laguerre-Gaussian ($LG_{p,l}$) and high-order Hermit-Gaussian ($HG_{m,n}$) modes, a KTP was inserted into DPSSDL close to the output coupler. The non-linear crystal, KTP, was pumped with the laser mode generated by the digital laser. A schematic of the experimental setup is presented in Fig. 7.2. The gray-scale (0-255) digital holograms were

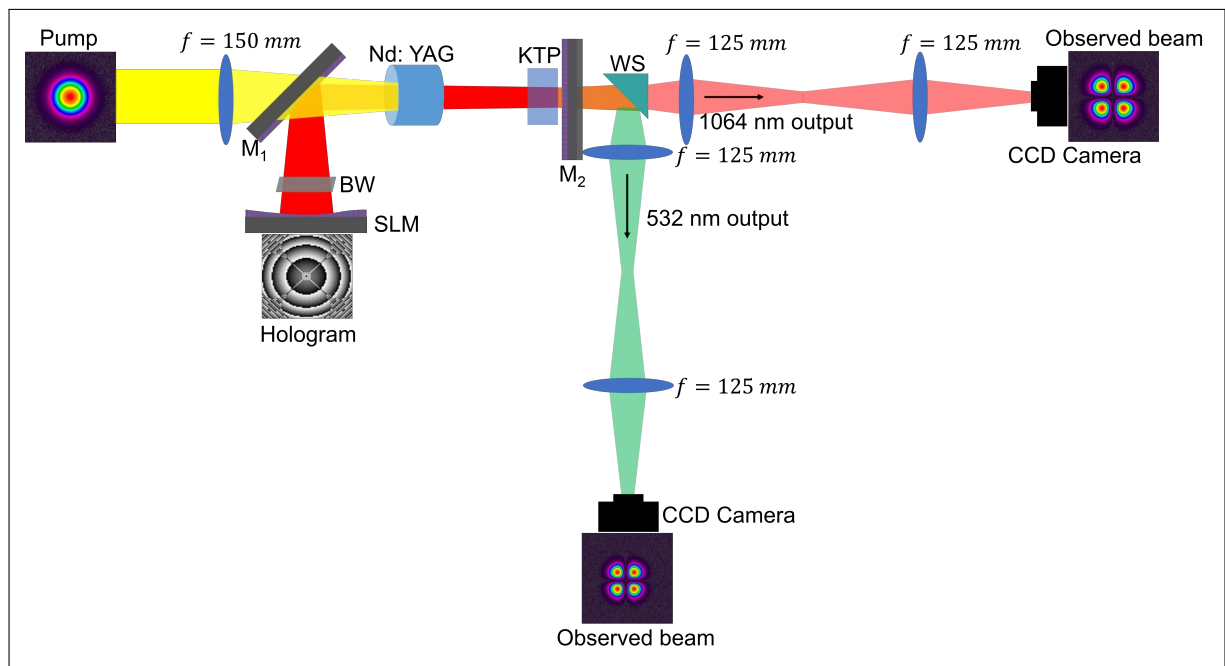


Figure 7.2 Schematic of the Nd: YAG crystal digital laser with a nonlinear crystal (KTP) against the output coupler of the resonator.

encoded to have varying width/thickness that would be a 98% match to each null of the $LG_{p,l}$ and $HG_{m,n}$ mode, for order $p, l = 0, 1, 2$ and $m, n = 0, 1, 2$.

The nonlinear crystal (KTP) rod of $3 \text{ mm} \times 3 \text{ mm} \times 5 \text{ mm}$ in volume was pumped with a Nd: YAG laser operating at 1064 nm. The KTP crystal was mounted inside a copper block that was not heat regulated. The digital laser was able to deliver output power up to $\approx 1.9 \text{ W}$ at an emission wavelength of 1064 nm (at room temperature).

The SLM of the DPSSDL was encoded with a digital hologram that varied the curvature from 200 mm to 500 mm with a step size of 50 mm, in order to easily control the size of the 1064 nm beam. A flat output coupler mirror (M_2) with a reflectivity of 90% was used. Since the SLM is a phase-only device, many of the desired holograms require both amplitude and phase change to the field. In order to achieve this, we made use of the well-known method of complex amplitude modulation [57, 120], as it is suitable for implementation on the SLM. The resonator was designed to form an L-shape (to avoid illuminating the SLM with the residual pump light) by including a 45° mirror (M_1) within the cavity. The mirror was highly reflective for 1064 nm and highly transmissive for 808 nm. The resonator length was chosen to be 190 mm.

Both 1064 nm and 532 nm beams exit the output coupler mirror (M_2) in parallel to each other. We used a beam splitter that acted as a wavelength separator (WS), with the result that 1064 nm and 532 nm wavelengths were separated. Two lenses with equal focal length of 125 mm were used to relay image the plane of the output coupler for 1064 nm. Furthermore, another pair of lenses with equal focal length of 125 mm were used to relay image the plane of the output couple for 532 nm to the CCD cameras for the characterisation of the laser mode.

7.4 Results and discussions

The modes were excited from the cavity by employing computer-generated hologram amplitude masks that had been encoded as pixelated grey (0-255) images and were displayed onto an SLM that also acted as a curved end mirror DPSSDL [60]. The results of the observed intensity distribution profiles for Laguerre-Gaussian modes and Hermit-Gaussian modes operating at along 1064 nm (ω) are shown in Fig. 7.3a and 7.3b, respectively. The two figures show similar intensity profiles to the one's discussed in Chpt. 1 shown by Fig. 1.5. These 2D-intensity distribution profiles that are shown were captured at the output coupler of the laser resonator. However, they remained the same as the propagation was varied from near to far field. This suggests that the generated laser modes were pure and lost neither quality nor purity as they propagated (see Ref. [85]).

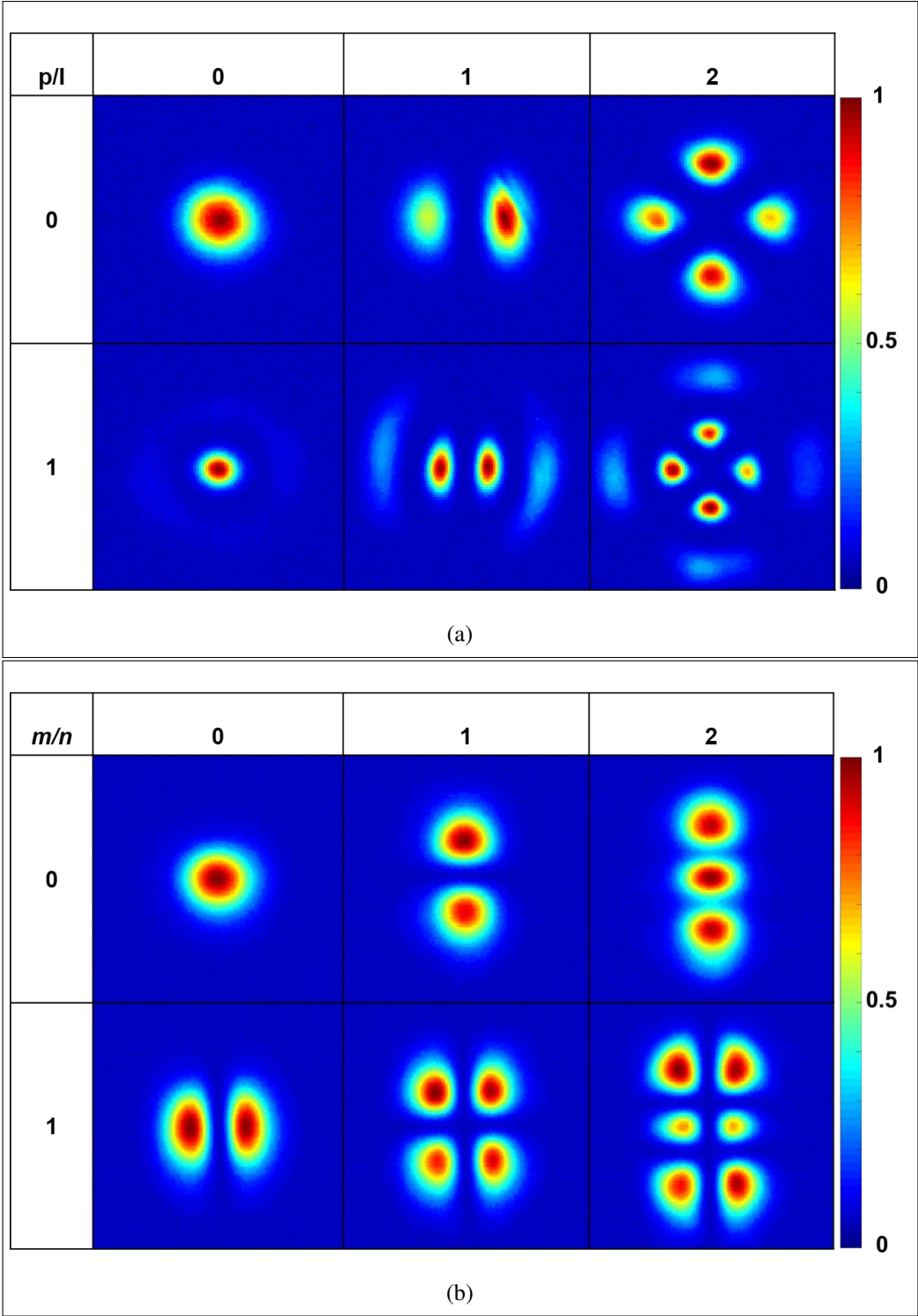


Figure 7.3 (a) The observed 2D intensity profiles for LG_{p,l} operating at 1064 nm. (b) The observed 2D intensity profiles HG_{m,n} operating at 1064 nm.

Furthermore, 2D-intensity distribution profiles for SHG laser modes were captured and are shown in Fig. 7.4a, 7.4b, 7.5, 7.6a and 7.6b. First we showed the results (Fig. 7.4a, 7.4b and 7.5) for when the Gaussian beam of 1064 nm is out of phase with the KTP. The concept of “out of phase” means that the conversion efficiency is low. The conversion efficiency depends on the intensity of the second harmonic wave that is proportional to the intensity of the converted wave, as shown in Eq. 7.8. The converted mode intensity depends on both the power and the size of the mode. This concept is evident in the far-field since the mode will start losing shape. When the doubled frequency 2ω propagates, the observed intensity profile does not match the predicted profile. In layman’s terms, the generated 2ω loses its quality, and the purity of these modes subsequently deteriorates. The intensity distribution has additional intensity loops between the predicted loops. This is mainly due to the size of the fundamental mode mismatching the nonlinear KTP crystal and the inputted power to the KTP crystal.

It is evident from the Fig. 7.6a and 7.6b we finally solved the low conversion efficiency problem since DPSSDL can able to display rewritable holograms to the SLM (see Fig. 7.2). In addition, the pump power was correctly adjusted to the lasing threshold to have sufficient intensity to excite 2ω . This concept is known as in-phase or phase matching of a Gaussian beam of ω with the intracavity crystal, KTP.

Phase matching is done by changing the curvature of the digital end mirror from 200 mm to 500 mm. With a step size of 50 mm, we found that at the radius of curvature equal to or above 400 mm, the Gaussian beam will be in-phase with the nonlinear crystal, KTP, when the Nd:YAG crystal shown in Fig. 7.2 is pumped above the pump threshold shown in Ref. [85]. Since the cavity length of 184 mm and the radius of curvature of 400 mm were chosen, the beam size of the Gaussian mode that pumps the KTP is about ≈ 260 mm. For a Gaussian beam that is in phase with the nonlinear crystal, the intensity profiles observed in the far field and near field are the same as predicted. The additional intensities between the loops or between the rings or the peak disappear in both near field and far field. Thus, the 2ω generated becomes pure and of high quality.

Furthermore, since the excited higher-order $LG_{p,l}$ and $HG_{m,n}$ modes were generated by a stable resonator cavity [121], the beam radius w of the modes is known analytically. We compared analytical results to the experimental results as summarised in Fig. 7.7a, 7.7b, 7.8a and Fig. 7.8b. Please note that in size, the modes for 2ω can be calculated by dividing Eq. 1.45, 1.46 and 1.47 by $\sqrt{2}$. From the beam size results, it is evident that the cavity is choosing anticipated modes with appropriate beam sizes. However, some experimental errors are evident in the results. These errors include the aperture used to measure the beam size since we didn’t use the cross-section of the beam and fit it. Furthermore, B-coated lenses (shown in Fig. 7.2)

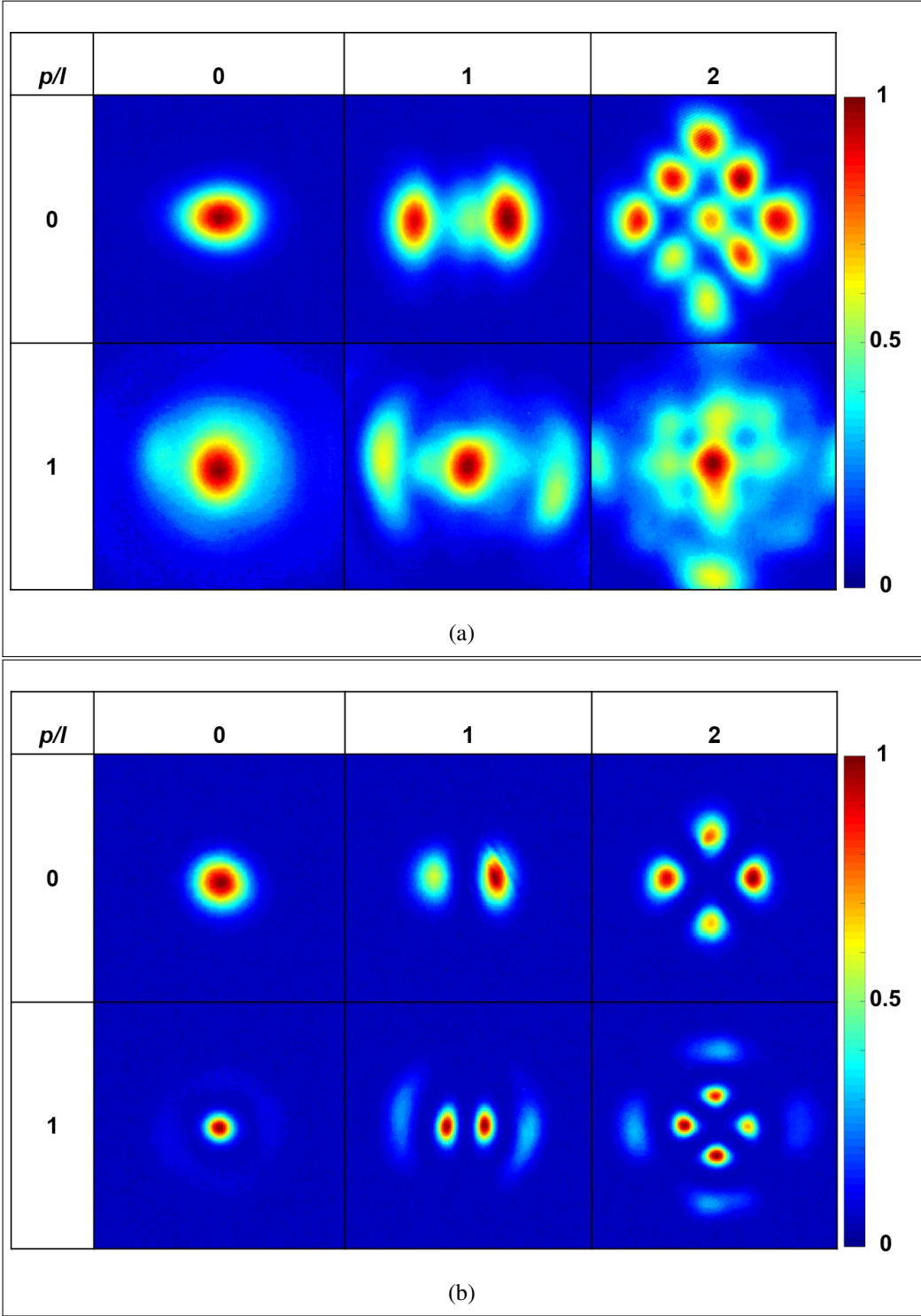


Figure 7.4 (a) The observed 2D intensity profiles for $LG_{p,l}$ operating at 532 nm at the far-field with pump out of phase with KTP. (b) The observed 2D intensity profiles for $LG_{p,l}$ operating at 532 nm at the near-field with pump out of phase with KTP.

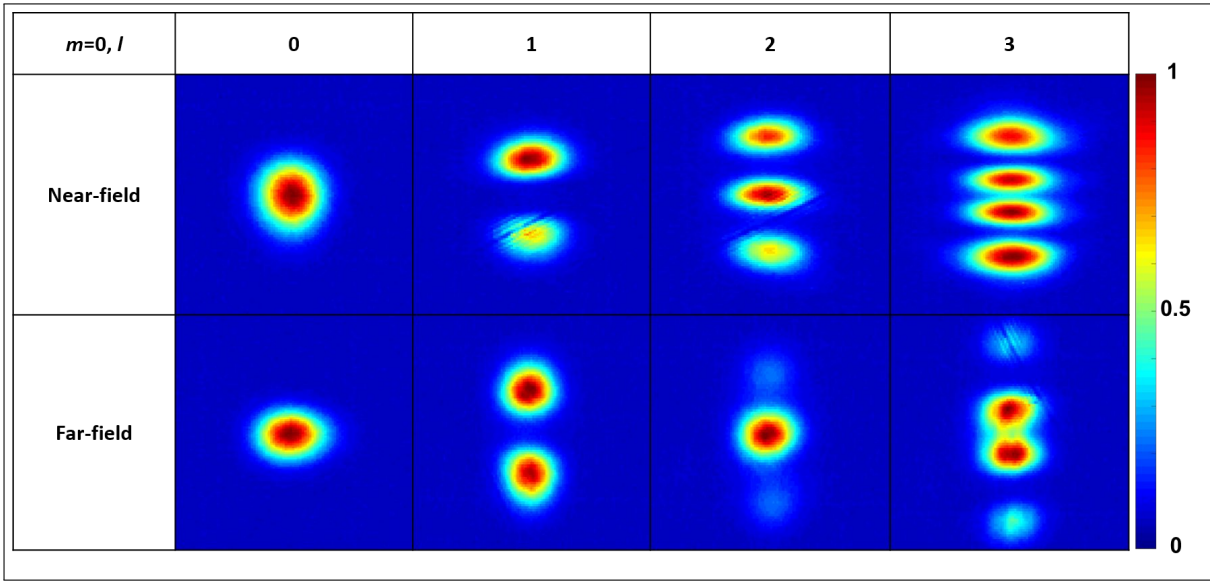


Figure 7.5 The observed 2D intensity profiles for $HG_{0,n}$ operating at 532 nm at the far-field and near-field with pump out of phase with KTP.

were used for both wavelengths, for relay imaging of the laser beam to the CCD cameras. In addition, errors that could be contributed to the entire experiment included the KTP crystal that we were using, the fact that the crystal was not well cleaned and had some minor scratches. However, the results are all in good agreement with the theory.

7.5 Summary

We successfully converted the higher-order Laguerre-Gaussian modes and Hermite-Gaussian modes operating at 1064 nm to higher-order Laguerre-Gaussian modes and Hermite-Gaussian modes operating at 532 nm. The length of the nonlinear crystal (KTP) that was used was only 3 mm. The fundamental beam intensity $I_1(0)$ that was required to convert fundamental power into the second harmonic was 0.0078 GW/cm^2 , which is in line with the theory presented in Sec. 7.2. We realised that if we wished to achieve a higher conversion efficiency and generate other higher-order modes, we would have to use a longer KTP with a bigger volume.

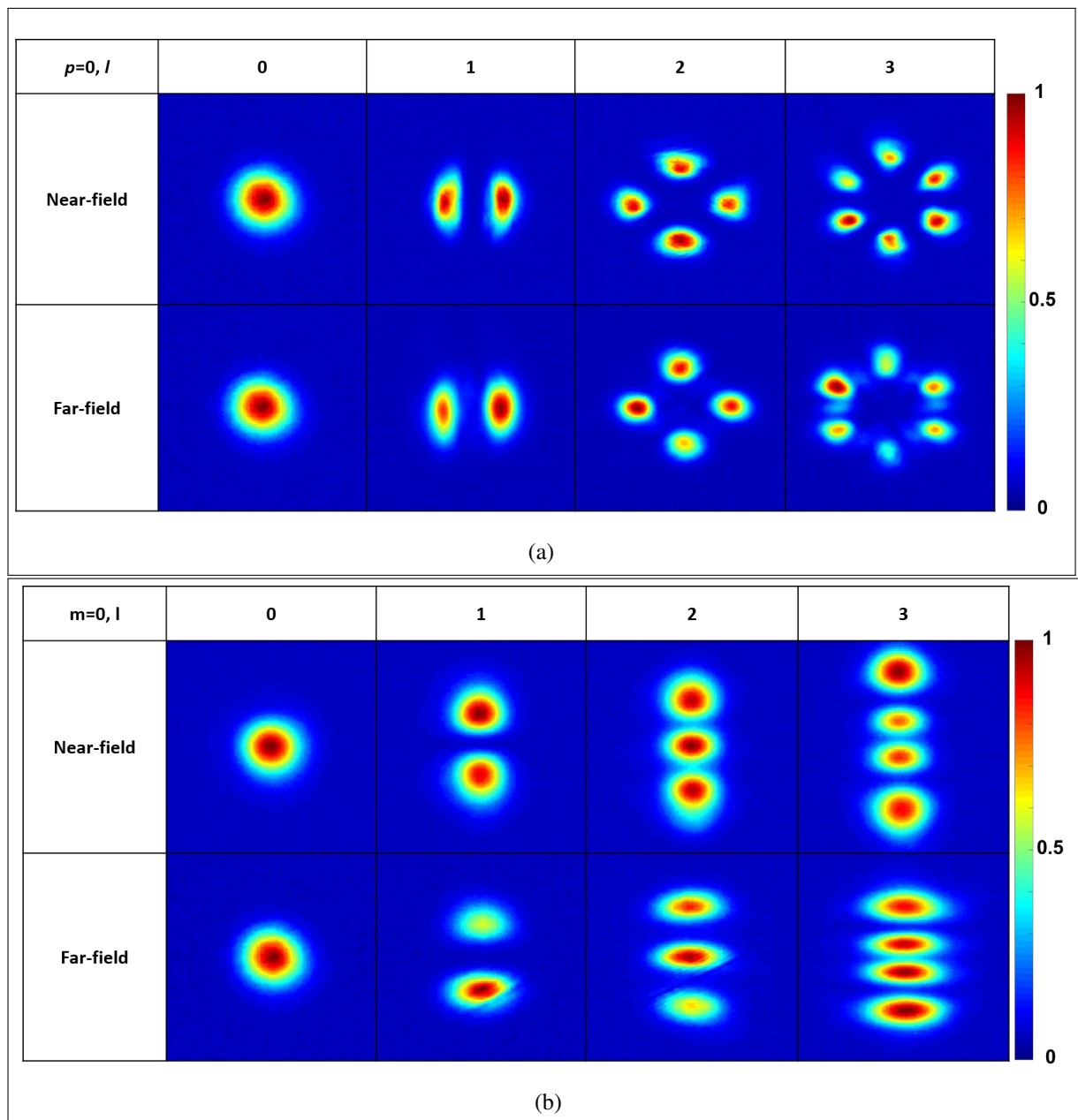


Figure 7.6 (a) The observed 2D intensity profiles for $LG_{p,l}$ operating at 532 nm with pump in phase with KTP. (b) The observed 2D intensity profiles for $HG_{p,l}$ operating at 532 nm with pump in phase with KTP.

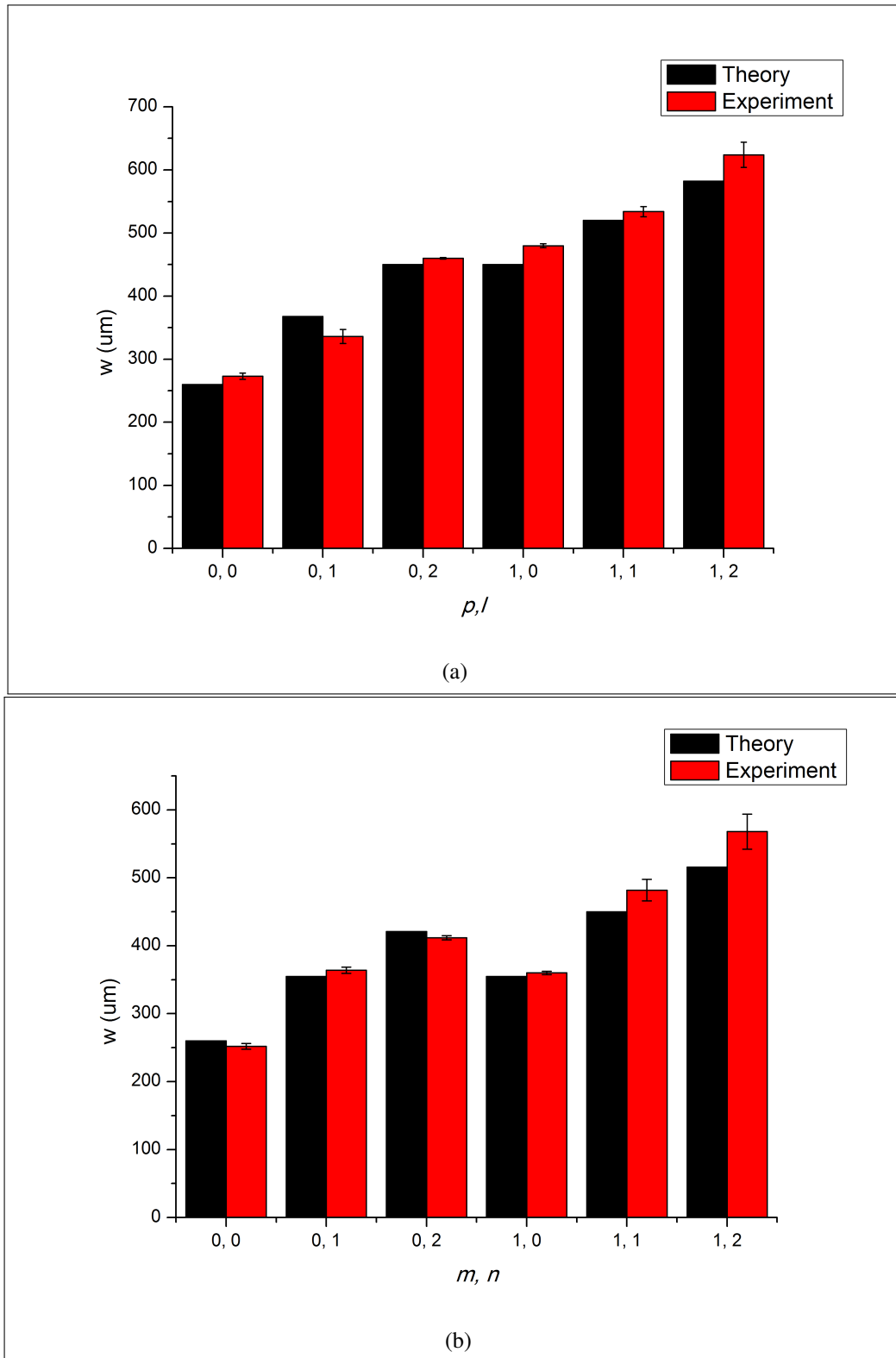


Figure 7.7 (a) The size (w) of the LG _{p,l} laser beams operating at 1064 nm as the function of mode order at the output coupler. (b) The size (w) of the HG _{m,n} laser beams operating at 1064 nm as the function of mode order at the output coupler.

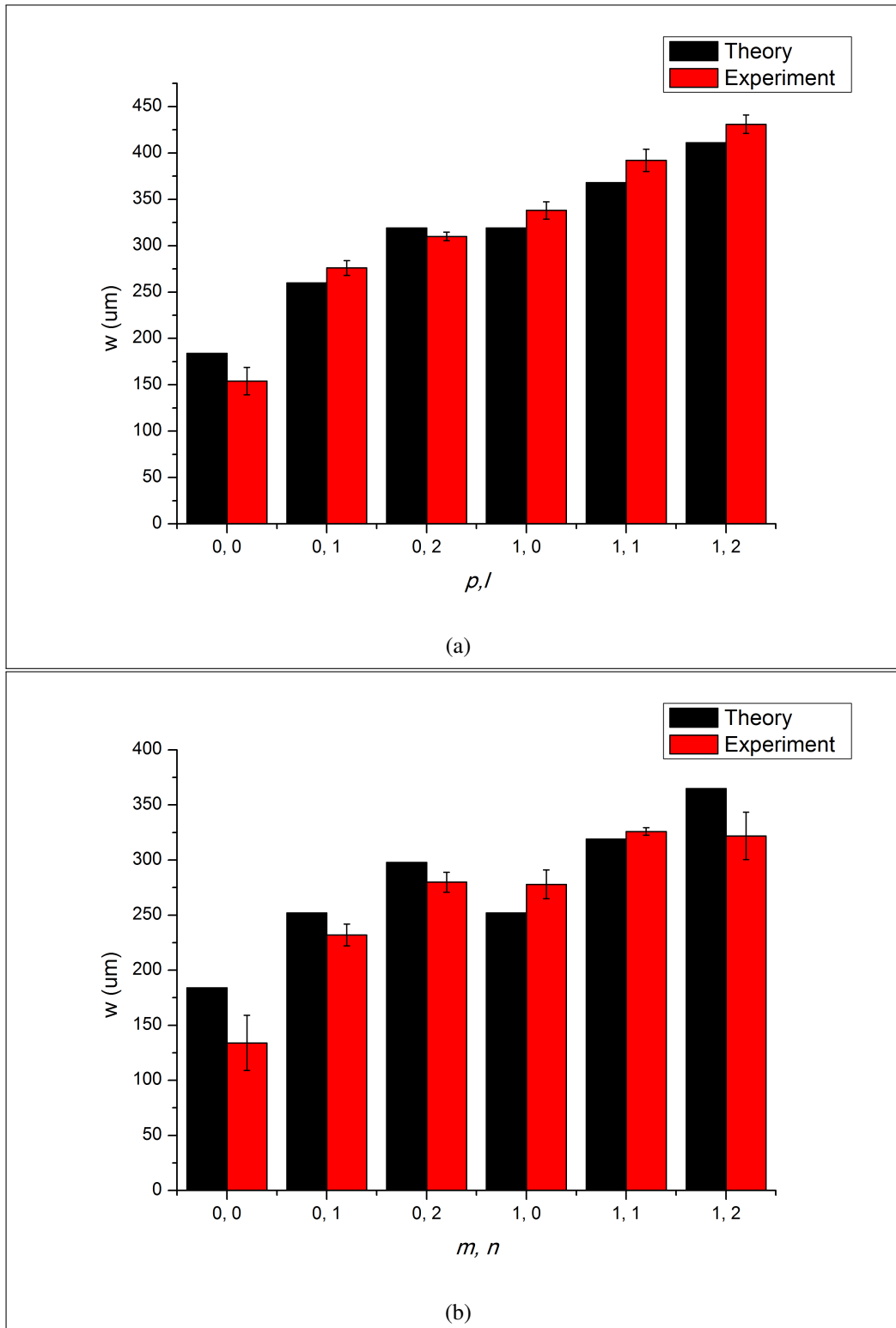


Figure 7.8 The size (w) of the LG _{p,l} laser beams operating at 532 nm as the function of mode order at the output coupler. (b) The size (w) of the HG _{m,n} laser beams operating at 532 nm as the function of mode order at the output coupler.

Chapter 8

Conclusion remarks and future perspective

In Chapter 1, we introduced basic optics, mode selection, resonator configurations, mode sections inside the laser resonator, and finally the “new” way of selecting modes using the digital laser. All the introduced concepts were carefully considered when experiments were conducted to be reported on in this dissertation. In Chapter 2, we investigated the relationship between the absorbed pumped power and transmitted pump power. Furthermore, we also examined how the refractive index of the gain medium would influence the quality of the beam if one had to pump at high power (max of 75 W). When the gain medium was pumped until end bulging was experienced, the gain medium started acting like a lens at that point. We employed a calibration technique to known lenses with high finesse, tested several lenses and extended the technique to a pumped solid-state gain medium. We investigated the measurement of a thermally induced lensing effect with a Shack-Hartmann wavefront sensor in an end-pumped solid-state gain medium and compared the results with those of thermal lensing measured by varying the length of an unstable resonator. The output power on the unstable laser resonator was also measured for verification of thermal lensing effect. The SHWFS method was found to be highly consistent with the pump absorption as well as more accurate than a geometrical method to alleviate irregularities in the geometrical method.

Based on the findings in Chapter 2 we confirmed that thermal aberration, in particular, defocuses aberration, would not affect the generation of modes inside the laser resonator – the aberration would be minimal. We then showed that it was possible to generate Laguerre-Gaussian beams for both radial and azimuthal order by using a diode-pumped solid-state digital laser. Our results showed that one can digitally control any order modes by selectively exciting the modes. Furthermore, we also showed that it was possible to selectively excite high radial

order LG modes of $p = 0 - 4$ that are in very good agreement with the theoretically expected results for the beam profiles, sizes and quality factor. The results showed that one can digitally excite a single high-order $LG_{p,0}$ mode by loading a gray-scale digital hologram that represents the mode of interest and aims to extract more power from the laser gain medium. We showed that through generating an $LG_{3,0}$ mode, we can extract more power from the digital laser gain medium than through generating a lowest-order $LG_{0,0}$ mode when using an amplitude mask that was introduced on intra-cavity SLM that acted as an end mirror of the resonator. The results further suggested that a digital laser could be used as a simulation test tool for manufacturing amplitude masks to develop a high-brightness laser that can operate by selective excitation of single higher-order $LG_{p,0}$ laser modes above the critical input power.

However, since high losses are still experienced when it comes to generating these radial-order Laguerre-Gaussian modes, we constructed digital holograms that can minimise the losses. The gray-scale digital hologram was constructed by using circular absorbing rings from 50% to 100% completeness. Our results indicated that we could digitally excite higher-order modes while maintaining a lower excitation threshold if we used a 50% complete p -absorbing amplitude mask. We also successfully demonstrated that high radial order Laguerre-Gaussian LG_p modes could be generated using circular absorbing rings that were 37.5% to 100% complete. The results furthermore indicated that we were able to digitally excite high radial order LG_p modes with the lowest excitation pump power threshold, ϵ_p . This was possible when the absorbing rings were 37.5% complete or when $\alpha = 1.3 = 0.81\pi/2$, and when all the other resonator characteristics such as the generated LG_p mode size, w_p , beam quality factor, M_p^2 , and the slope efficiency, η_p , of the laser, were maintained.

Once we were able to minimise the losses, we saw that it was necessary to laser pulses using on-demand laser modes, so as to increase power and generate the pulse of different shapes for different applications in one go. In Chapter 5, we successfully developed a laser that was able to generate on-demand laser pulses of various shapes. The laser pulses generated for the Laguerre-Gaussian mode of radial order $p=0$ and azimuthal-order $l=(0, 1, 2)$ had a pulse length of 200 ms and a repetition rate of 60 Hz, while the Gaussian mode had an average power of 1.36 mW and pulse energy of 6.8 μ J.

We managed to decrease losses inside the cavity and were able to create pulses. However, the digital laser still had power limitations. Thus, in Chapter 6, we successfully amplified higher-order $LG_{p,l}$ laser by using an extra-cavity Nd: YAG amplifier (single pass), and by matching the pump size and the seed laser modes. The highest power amplification was experienced at 42% for $LG_{2,0}$. For $LG_{2,2}$, the seed laser mismatched the pump, with the result

that the intensity profile of the seed laser was not quite similar to that of the amplified seed laser mode.

In Chapter 7, we successfully converted the higher-order Laguerre-Gaussian and Hermite-Gaussian modes operating at 1064 nm to higher-order Laguerre-Gaussian and Hermite-Gaussian modes operating at 532 nm. The length of the non-linear crystal KTP that was used, was only 3 mm. The fundamental beam intensity $I_1(0)$ required to convert fundamental power into the second harmonic was 0.0213 GW/cm^2 , which agreed well with the theory. It was noted that if we wished to achieve a higher conversion efficiency and be able to generate other higher-order modes, we should use a longer KTP with a bigger area. Nevertheless, to the best of our knowledge, our experimental findings on the generation of higher-order modes for 2ω have never before been reported.

In future studies for amplification of laser modes we plan to use seed laser beams that will allow for larger extraction of the power and convert them to a Gaussian mode for high brightness lasers. In addition, we intend to decrease the pulse length to 1 ns and increase the repetition rate to 1 kHz. This will be done by controlling the SLM with LabVIEW and changing its speed. Furthermore, one could use this laser to model optics such as diffractive optical elements (DOE) for high-powered lasers, and DOE for high brightness lasers. The latter have huge potential for use in the military and in communications. In addition, this laser is able to generate higher-order modes of high quality and purity in both 1064 nm and 532 nm. Moving forward, we will consider prototyping this laser in order to eventually make it a device that can be commercialised.

Bibliography

- [1] J. C. Maxwell, *The Scientific Letters and Papers of James Clerk Maxwell: 1846-1862*, vol. 1. CUP Archive, 1990.
- [2] J. D. Jackson, *Classical electrodynamics*. Wiley, 1999.
- [3] A. E. Siegman, "New developments in laser resonators," in *OE/LASE'90, 14-19 Jan., Los Angeles, CA*, pp. 2–14, International Society for Optics and Photonics, 1990.
- [4] R. Hibst and U. Keller, "Experimental studies of the application of the er: Yag laser on dental hard substances: I. measurement of the ablation rate," *Lasers in Surgery and Medicine*, vol. 9, no. 4, pp. 338–344, 1989.
- [5] E. Mester, A. F. Mester, and A. Mester, "The biomedical effects of laser application," *Lasers in surgery and medicine*, vol. 5, no. 1, pp. 31–39, 1985.
- [6] F. Schwarz, A. Aoki, J. Becker, and A. Sculean, "Laser application in non-surgical periodontal therapy: a systematic review," *Journal of clinical periodontology*, vol. 35, no. s8, pp. 29–44, 2008.
- [7] F. H. Loesel, M. H. Niemz, J. Bille, and T. Juhasz, "Laser-induced optical breakdown on hard and soft tissues and its dependence on the pulse duration: experiment and model," *IEEE Journal of Quantum Electronics*, vol. 32, no. 10, pp. 1717–1722, 1996.
- [8] M. Halbwx, T. Sarnet, P. Delaporte, M. Sentis, H. Etienne, F. Torregrosa, V. Vervisch, I. Perichaud, and S. Martinuzzi, "Micro and nano-structuration of silicon by femtosecond laser: application to silicon photovoltaic cells fabrication," *Thin solid films*, vol. 516, no. 20, pp. 6791–6795, 2008.
- [9] A. Hofstetter, F. Frank, E. Keiditsch, and R. Böwering, "Endoscopic neodymium-yag laser application for destroying bladder tumors.," *European urology*, vol. 7, no. 5, pp. 278–282, 1980.
- [10] W. Welford, "Principles of lasers," *Journal of Modern Optics*, vol. 24, no. 3, pp. 282–283, 1977.
- [11] N. Barnes, "Diode-pumped solid-state lasers," *Journal of Applied Physics*, vol. 44, no. 1, pp. 230–237, 1973.
- [12] T. Y. Fan and R. L. Byer, "Diode laser-pumped solid-state lasers," *IEEJ. Quant. Electron*, vol. 24, no. 6, pp. 895–912, 1988.

- [13] R. Keyes and T. Quist, "Injection luminescent pumping of $\text{CaF}_2: \text{U}^{3+}$ with gas diode lasers," *Applied Physics Letters*, vol. 4, no. 3, pp. 50–52, 1964.
- [14] B. Aull and H. Jenssen, "Vibronic interactions in Nd: Yag resulting in nonreciprocity of absorption and stimulated emission cross sections," *IEEE Journal of Quantum Electronics*, vol. 18, no. 5, pp. 925–930, 1982.
- [15] H. Kogelnik and T. Li, "Laser beams and resonators," *Applied optics*, vol. 5, no. 10, pp. 1550–1567, 1966.
- [16] H. E. Salzer and R. Zucker, "Table of the zeros and weight factors of the first fifteen laguerre polynomials," *Bulletin of the American Mathematical Society*, vol. 55, no. 10, pp. 1004–1012, 1949.
- [17] M. Abramowitz, I. A. Stegun, *et al.*, "Handbook of mathematical functions," *Applied mathematics series*, vol. 55, p. 62, 1966.
- [18] H. E. Salzer, R. Zucker, and R. Capuano, *Table of the zeros and weight factors of the first twenty Hermite polynomials*. US Government Printing Office, 1952.
- [19] W. Koechner and M. Bass, *Solid-State Lasers: A Graduate Text*. Springer Science & Business Media, 2003.
- [20] W. T. Welford and R. Winston, "Nonconventional optical systems and the brightness theorem," *Appl. Opt.*, vol. 21, no. 9, pp. 1531–1533, 1982.
- [21] T. Johnston, "M2 concept characterizes beam quality," *Laser Focus World*, vol. 26, no. 5, pp. 173–183, 1990.
- [22] S. Ngcobo, I. Litvin, L. Burger, and A. Forbes, "A digital laser for on-demand laser modes," *Nat.*, vol. 4, 2013.
- [23] B. Bouma, M. Ramaswamy-Paye, and J. Fujimoto, "Compact resonator designs for mode-locked solid-state lasers," *Applied Physics B: Lasers and Optics*, vol. 65, no. 2, pp. 213–220, 1997.
- [24] V. Magni, G. Valentini, and S. De Silvestri, "Recent developments in laser resonator design," *Optical and quantum electronics*, vol. 23, no. 9, pp. 1105–1134, 1991.
- [25] M. Innocenzi, H. Yura, C. Fincher, and R. Fields, "Thermal modeling of continuous-wave end-pumped solid-state lasers," *Applied Physics Letters*, vol. 56, no. 19, pp. 1831–1833, 1990.
- [26] B. Neuenschwander, R. Weber, and H. P. Weber, "Determination of the thermal lens in solid-state lasers with stable cavities," *IEEE journal of quantum electronics*, vol. 31, no. 6, pp. 1082–1087, 1995.
- [27] V. Magni, "Resonators for solid-state lasers with large-volume fundamental mode and high alignment stability," *Applied optics*, vol. 25, no. 1, pp. 107–117, 1986.
- [28] T. Bell, D. Naidoo, S. Ngcobo, and A. Forbes, "Thermal lensing measurement from the coefficient of defocus aberration using shack-hartmann wavefront sensor," in *SPIE LASE*, pp. 97271L–97271L, International Society for Optics and Photonics, 2016.

- [29] N. Hodgson and H. Weber, *Laser Resonators and Beam Propagation: Fundamentals, Advanced Concepts, Applications*, vol. 108. Springer, 2005.
- [30] W. Koechner, *Solid-state laser engineering*, vol. 1. Springer, 2013.
- [31] P. Bélanger, “Beam propagation and the abcd ray matrices,” *Optics Letters*, vol. 16, no. 4, pp. 196–198, 1991.
- [32] K. Ballüder, M. Taghizadeh, H. McInnes, and T. Bett, “Diffractive optical elements for intra-cavity beam-shaping of laser modes,” *Journal of Modern Optics*, vol. 47, no. 13, pp. 2421–2435, 2000.
- [33] E. Cagniot, M. Fromager, T. Godin, N. Passilly, M. Brunel, and K. Ait-Ameur, “Variant of the method of fox and li dedicated to intracavity laser beam shaping,” *JOSA A*, vol. 28, no. 3, pp. 489–495, 2011.
- [34] I. A. Litvin and A. Forbes, “Intra-cavity flat-top beam generation,” *Optics express*, vol. 17, no. 18, pp. 15891–15903, 2009.
- [35] J. Leger, *Laser beam shaping*. Taylor & Francis, London, 1997.
- [36] U. O. Farrukh, A. M. Buoncristiani, and C. E. Byvik, “An analysis of the temperature distribution in finite solid-state laser rods,” *Quantum Electronics*, vol. 24, no. 11, 1988.
- [37] C. Pfistner, R. Weber, H. Weber, S. Merazzi, and R. Gruber, “Thermal beam distortions in end-pumped Nd:YAG, Nd:GSGG, and Nd:YLF rods,” *Quantum Electronics*, vol. 30, no. 7, pp. 1605–1615, 1994.
- [38] I. Freitag, A. Tünnermann, and H. Welling, “Power scaling of diode-pumped monolithic Nd:YAG lasers to output powers of several watts,” *Optics Communications*, vol. 115, no. 5, pp. 511–515, 1995.
- [39] M. MacDonald, T. Graf, J. Balmer, and H. Weber, “Reducing thermal lensing in diode-pumped laser rods,” *Optics Communications*, vol. 178, no. 4, pp. 383–393, 2000.
- [40] G. Cerullo, S. De Silvestri, V. Magni, and O. Svelto, “Output power limitations in CW single transverse mode Nd:YAG lasers with a rod of large cross-section,” *Optical and Quantum electronics*, vol. 25, no. 8, pp. 489–500, 1993.
- [41] J. Foster and L. Osterink, “Thermal effects in a Nd:YAG laser,” *Journal of Applied Physics*, vol. 41, no. 9, pp. 3656–3663, 1970.
- [42] P. Hardman, W. Clarkson, G. Friel, M. Pollnau, and D. Hanna, “Energy-transfer upconversion and thermal lensing in high-power end-pumped Nd:YLF laser crystals,” *Quantum Electronics*, vol. 35, pp. 647–655, Apr 1999.
- [43] J. D. Mansell, J. Hennawi, E. K. Gustafson, M. M. Fejer, R. L. Byer, D. Clubley, S. Yoshida, and D. H. Reitze, “Evaluating the effect of transmissive optic thermal lensing on laser beam quality with a shack-hartmann wave-front sensor,” *Applied optics*, vol. 40, no. 3, pp. 366–374, 2001.

- [44] H. Erickson and A. Klug, "Measurement and compensation of defocusing and aberrations by fourier processing of electron micrographs," *Philosophical Transactions of the Royal Society B: Biological Sciences*, vol. 261, no. 837, pp. 105–118, 1971.
- [45] R. Paschotta, J. d. Au, and U. Keller, "Thermal effects in high-power end-pumped lasers with elliptical-mode geometry," *Quantum Electronics*, vol. 6, no. 4, pp. 636–642, 2000.
- [46] A. Hays and R. Burnham, "High duty-cycle diode-pumped nd: Ylf slab laser," in *Advanced Solid-State Lasers Conference*, 1993.
- [47] S. Chénais, F. Druon, S. Forget, F. Balembois, and P. Georges, "On thermal effects in solid-state lasers: The case of ytterbium-doped materials," *Progress in Quantum Electronics*, vol. 30, no. 4, pp. 89–153, 2006.
- [48] A. Demidovich, A. Shkadarevich, M. Danailov, P. Apai, T. Gasmi, V. Gribkovskii, A. Kuzmin, G. Ryabtsev, and L. Batay, "Comparison of CW laser performance of Nd:KGW, Nd:YAG, Nd:BEL, and Nd:YVO4 under laser diode pumping," *Applied Physics B*, vol. 67, no. 1, pp. 11–15, 1998.
- [49] D. Lancaster and J. Dawes, "Thermal-lens measurement of a quasi steady-state repetitively flashlamp-pumped Cr, Tm, Ho:YAG laser," *Optics & Laser Technology*, vol. 30, no. 2, pp. 103–108, 1998.
- [50] J. Wang and D. E. Silva, "Wave-front interpretation with Zernike polynomials," *Applied Optics*, vol. 19, no. 9, pp. 1510–1518, 1980.
- [51] T. M. Jeong, C. Lee, D.-K. Ko, J. Lee, and H. S. Kim, "Analysis of a laser resonator from the measurement of thermal aberrations in a laser-diode side-pumped Nd:YAG laser with a wavefront sensor," *Journal of the Korean Physical Society*, vol. 51, no. 1, pp. 78–83, 2007.
- [52] B. W. Smith and R. E. Schlieff, "Understanding lens aberration and influences to lithographic imaging," in *Microlithography 2000*, pp. 294–306, International Society for Optics and Photonics, 2000.
- [53] W. Koechner, *Optical resonator*. Springer, 2006.
- [54] I. A. Litvin, S. Ngcobo, D. Naidoo, K. Ait-Ameur, and A. Forbes, "Doughnut laser beam as an incoherent superposition of two petal beams," *Opt.lett*, vol. 39, no. 3, pp. 704–707, 2014.
- [55] S. Ngcobo, K. Ait-Ameur, I. Litvin, A. Hasnaoui, and A. Forbes, "Tuneable Gaussian to flat-top resonator by amplitude beam shaping," *Opt.express*, vol. 21, no. 18, pp. 21113–21118, 2013.
- [56] S. Ngcobo, K. Ait-Ameur, N. Passilly, A. Hasnaoui, and A. Forbes, "Exciting higher-order radial Laguerre–Gaussian modes in a diode-pumped solid-state laser resonator," *Appl. Opt*, vol. 52, no. 10, pp. 2093–2101, 2013.
- [57] V. Arrizón, U. Ruiz, R. Carrada, and L. A. González, "Pixelated phase computer holograms for the accurate encoding of scalar complex fields," *JOSA A*, vol. 24, no. 11, pp. 3500–3507, 2007.

- [58] M. Nakazawa, H. Kubota, A. Sahara, and K. Tamura, "Time-domain abcd matrix formalism for laser mode-locking and optical pulse transmission," *IEEE Journal of Quantum Electronics*, vol. 34, no. 7, pp. 1075–1081, 1998.
- [59] Optical Society of America, *Ultrafast Lasers with kW Class Output Power for Applications in Industry and Science*, 2014.
- [60] S. Ngcobo, I. Litvin, L. Burger, and A. Forbes, "A digital laser for on-demand laser modes," *Nature communications*, vol. 4, 2013.
- [61] International Society for Optics and Photonics, *Selective excitation and detection of higher-order doughnut laser modes as an incoherent superposition of two petals modes in a digital laser resonator*, 2015.
- [62] R. Brünig, S. Ngcobo, M. Duparré, and A. Forbes, "Direct fiber excitation with a digitally controlled solid state laser source," *Opt.lett.*, vol. 40, no. 3, pp. 435–438, 2015.
- [63] D. Flamm, D. Naidoo, C. Schulze, A. Forbes, and M. Duparré, "Mode analysis with a spatial light modulator as a correlation filter," *Opt.lett.*, vol. 37, no. 13, pp. 2478–2480, 2012.
- [64] C. Schulze, S. Ngcobo, M. Duparré, and A. Forbes, "Modal decomposition without a priori scale information," *Opt.express*, vol. 20, no. 25, pp. 27866–27873, 2012.
- [65] A. Hasnaoui and K. Ait-Ameur, "Properties of a laser cavity containing an absorbing ring," *Applied optics*, vol. 49, no. 21, pp. 4034–4043, 2010.
- [66] I. A. Litvin, A. Dudley, F. S. Roux, and A. Forbes, "Azimuthal decomposition with digital holograms," *Optics express*, vol. 20, no. 10, pp. 10996–11004, 2012.
- [67] K. Sueda, G. Miyaji, N. Miyanaga, and M. Nakatsuka, "Laguerre-Gaussian beam generated with a multilevel spiral phase plate for high intensity laser pulses," *Opt. Express*, vol. 12, no. 15, pp. 3548–3553, 2004.
- [68] N. Matsumoto, T. Ando, T. Inoue, Y. Ohtake, N. Fukuchi, and T. Hara, "Generation of high-quality higher-order Laguerre-Gaussian beams using liquid-crystal-on-silicon spatial light modulators," *JOSA A*, vol. 25, no. 7, pp. 1642–1651, 2008.
- [69] D. Rhodes, D. Gherardi, J. Livesey, D. McGloin, H. Melville, T. Freearde, and K. Dhollakia, "Atom guiding along high order Laguerre-Gaussian light beams formed by spatial light modulation," *J. Mod. Opt.*, vol. 53, no. 4, pp. 547–556, 2006.
- [70] A. Mair, A. Vaziri, G. Weihs, and A. Zeilinger, "Entanglement of the orbital angular momentum states of photons," *Nat*, vol. 412, no. 6844, pp. 313–316, 2001.
- [71] K. C. Neuman and S. M. Block, "Optical trapping," *Review of scientific instruments*, vol. 75, no. 9, pp. 2787–2809, 2004.
- [72] F. Pampaloni and J. Enderlein, "Gaussian, Hermite-Gaussian, and Laguerre-Gaussian beams: A primer," *arXiv*, 2004.
- [73] N. Simpson, L. Allen, and M. Padgett, "Optical tweezers and optical spanners with Laguerre-Gaussian modes," *J. Mod. Opt.*, vol. 43, no. 12, pp. 2485–2491, 1996.

- [74] International Society for Optics and Photonics, *Strong reducing of the laser focal volume*, 2011.
- [75] J. Arlt, R. Kuhn, and K. Dholakia, “Spatial transformation of Laguerre-Gaussian laser modes,” *J. Mod. Opt.*, vol. 48, no. 5, pp. 783–787, 2001.
- [76] Y.-X. Ren, M. Li, K. Huang, J.-G. Wu, H.-F. Gao, Z.-Q. Wang, and Y.-M. Li, “Experimental generation of Laguerre-Gaussian beam using digital micromirror device,” *Appl. Opt.*, vol. 49, no. 10, pp. 1838–1844, 2010.
- [77] S. Ngcobo, T. Bell, K. Ait-Ameur, and A. Forbes, “Low-loss selective excitation of higher-order modes in a diode-pumped solid-state digital laser,” in *SPIE Optical Engineering+ Applications*, pp. 95810S–95810S, International Society for Optics and Photonics, 2015.
- [78] T. Bell, A. Hasnaoui, K. Aït-Ameur, A. Forbes, and S. Ngcobo, “Intracavity generation of low-loss radial-order Laguerre-Gaussian modes using digital holograms,” in *SPIE LASE*, pp. 97271K–97271K, International Society for Optics and Photonics, 2016.
- [79] S. Kubota and Y. Kaneda, “End pumped solid-state laser,” Apr. 13 1993. US Patent 5,202,893.
- [80] A. Hasnaoui, A. Bencheikh, M. Fromager, E. Cagniot, and K. Aït-Ameur, “Creation of a sharper focus by using a rectified tem p0 beam,” *Optics Communications*, vol. 284, no. 5, pp. 1331–1334, 2011.
- [81] A. Hasnaoui, S. Haddadi, M. Fromager, D. Louhibi, A. Harfouche, E. Cagniot, and K. Aït-Ameur, “Transformation of a lg10 beam into an optical bottle beam,” *Laser Physics*, vol. 25, no. 8, p. 085004, 2015.
- [82] S. Haddadi, A. Hasnaoui, M. Fromager, D. Louhibi, A. Harfouche, E. Cagniot, and K. Aït-Ameur, “Use of a diaphragm for transforming a lg 10 beam into a flat-top,” *Optik-International Journal for Light and Electron Optics*, vol. 127, no. 4, pp. 2207–2211, 2016.
- [83] J. Alda, “Laser and gaussian beam propagation and transformation,” *Encyclopedia of Optical Engineering*, vol. 2013, pp. 999–1013, 2003.
- [84] I. Standard, “Handbook of standard iso,” 2005.
- [85] T. Bell and S. Ngcobo, “Selective excitation of higher-radial-order laguerre-gaussian beams using a solid-state digital laser,” *J. Laser Opt Photonics*, vol. 3, no. 2, 2017.
- [86] A. Grudinin, E. Dianov, D. Korobkin, A. Prokhorov, V. Serkin, and D. Khaidarov, “Stimulated-raman-scattennng excitation of 18-fs pulses in the 1.6-ij-m region during pumping of a single-mode optical fiber by the beam from a ndryag laser ($k= 1.064 (\lambda_m)$),” *JETP Lett*, vol. 45, no. 5, 1987.
- [87] G. Cerullo, C. Bardeen, Q. Wang, and C. Shank, “High-power femtosecond chirped pulse excitation of molecules in solution,” *Chemical Physics Letters*, vol. 262, no. 3, pp. 362–368, 1996.

- [88] H. C. Kapteyn, "Photoionization-pumped x-ray lasers using ultrashort-pulse excitation," *Applied optics*, vol. 31, no. 24, pp. 4931–4939, 1992.
- [89] P. V. Nickles, V. Shlyaptsev, M. Kalachnikov, M. Schnürer, I. Will, and W. Sandner, "Short pulse x-ray laser at 32.6 nm based on transient gain in ne-like titanium," *Physical review letters*, vol. 78, no. 14, p. 2748, 1997.
- [90] U. Österberg and W. Margulis, "Dye laser pumped by nd: Yag laser pulses frequency doubled in a glass optical fiber," *Optics letters*, vol. 11, no. 8, pp. 516–518, 1986.
- [91] K. Spariosu, A. Shestakov, W. Chen, R. Stultz, and M. Birnbaum, "Dual q switching and laser action at 1.06 and 1.44 μm in a nd 3+: Yag-cr 4+: Yag oscillator at 300 k," *Optics letters*, vol. 18, no. 10, pp. 814–816, 1993.
- [92] J. Wilson and J. Hawkes, *Lasers, principles and applications*. Prentice Hall, 1987.
- [93] J. Gu, F. Zhou, W. Xie, S. C. Tam, and Y. L. Lam, "Passive q-switching of a diode-pumped nd: Yag laser with a gaas output coupler," *Optics communications*, vol. 165, no. 4, pp. 245–249, 1999.
- [94] J. Garcí, V. Aboites, A. Kir'yanov, M. Damzen, A. Minassian, *et al.*, "High repetition rate q-switching of high power nd: Yvo 4 slab laser," *Optics communications*, vol. 218, no. 1, pp. 155–160, 2003.
- [95] H. A. Haus, "Theory of mode locking with a fast saturable absorber," *Journal of Applied Physics*, vol. 46, no. 7, pp. 3049–3058, 1975.
- [96] P. W. Smith, "Mode-locking of lasers," *Proceedings of the IEEE*, vol. 58, no. 9, pp. 1342–1357, 1970.
- [97] R. Tucker, U. Koren, G. Raybon, C. Burrus, B. Miller, T. Koch, and G. Eisenstein, "40 ghz active mode-locking in a 1.5 μm monolithic extended-cavity laser," *Electronics letters*, vol. 25, no. 10, pp. 621–622, 1989.
- [98] C. Hönninger, R. Paschotta, F. Morier-Genoud, M. Moser, and U. Keller, "Q-switching stability limits of continuous-wave passive mode locking," *JOSA B*, vol. 16, no. 1, pp. 46–56, 1999.
- [99] T. Brabec, C. Spielmann, P. Curley, and F. Krausz, "Kerr lens mode locking," *Optics letters*, vol. 17, no. 18, pp. 1292–1294, 1992.
- [100] International Society for Optics and Photonics, *Femtosecond pulse laser ablation of metallic, semiconducting, ceramic, and biological materials*, 1994.
- [101] P. Gibbon and E. Förster, "Short-pulse laser-plasma interactions," *Plasma physics and controlled fusion*, vol. 38, no. 6, p. 769, 1996.
- [102] R. Luo, L. Li, W. Cui, Z. Yang, H. Wang, and X. Xu, "Experimental study of diode pumped rubidium amplifier for single higher-order laguerre-gaussian modes," *Optics Express*, vol. 24, no. 12, pp. 13351–13356, 2016.
- [103] J. J. Degnan, "Satellite laser ranging: current status and future prospects," *IEEE Transactions on Geoscience and Remote Sensing*, no. 4, pp. 398–413, 1985.

- [104] D.-M. He and G. G. Seet, "Laser gated-ranging for underwater robot vision in turbid waters," in *International Symposium on Remote Sensing*, pp. 11–22, International Society for Optics and Photonics, 2002.
- [105] T. Wiener and S. Karp, "The role of blue/green laser systems in strategic submarine communications," *IEEE Transactions on Communications*, vol. 28, no. 9, pp. 1602–1607, 1980.
- [106] F. Bandello, R. Brancato, R. Lattanzio, G. Trabucchi, C. Azzolini, and A. Malegori, "Double-frequency nd: Yag laser vs. argon-green laser in the treatment of proliferative diabetic retinopathy: Randomized study with long-term follow-up," *Lasers in surgery and medicine*, vol. 19, no. 2, pp. 173–176, 1996.
- [107] X. Li, X. Shen, and G. Li, "Cyclic variation of output energy with ambient temperature changes in intracavity ktp frequency-doubling laser," *Optik-International Journal for Light and Electron Optics*, vol. 126, no. 2, pp. 279–282, 2015.
- [108] S. F. Liew, S. Knitter, S. Weiler, J. F. Monjardin-Lopez, M. Ramme, B. Redding, M. A. Choma, and H. Cao, "Intracavity frequency-doubled degenerate laser," *arXiv preprint arXiv:1609.05534*, 2016.
- [109] D. N. Nikogosyan, *Nonlinear optical crystals: a complete survey*. Springer Science & Business Media, 2006.
- [110] V. G. Dmitriev, G. G. Gurzadyan, and D. N. Nikogosyan, *Handbook of nonlinear optical crystals*, vol. 64. Springer, 2013.
- [111] C. Defan and Y. Zhengtang, "Investigation on some properties of ktiopo 4 crystals," *Journal of Crystal Growth*, vol. 79, no. 1, pp. 974–977, 1986.
- [112] R. Ganeev, I. Kulagin, A. Ryasnyansky, R. Tugushev, and T. Usmanov, "Characterization of nonlinear optical parameters of kdp, linbo 3 and bbo crystals," *Optics communications*, vol. 229, no. 1, pp. 403–412, 2004.
- [113] R. Weis and T. Gaylord, "Lithium niobate: summary of physical properties and crystal structure," *Applied Physics A*, vol. 37, no. 4, pp. 191–203, 1985.
- [114] M. E. Hagerman and K. R. Poeppelmeier, "Review of the structure and processing-defect-property relationships of potassium titanyl phosphate: a strategy for novel thin-film photonic devices," *Chemistry of materials*, vol. 7, no. 4, pp. 602–621, 1995.
- [115] Z. Kecong and W. Ximin, "Structure sensitive properties of ktp-type crystals," *Chinese science bulletin*, vol. 46, no. 24, pp. 2028–2036, 2001.
- [116] T. A. Driscoll, P. E. Perkins, H. J. Hoffman, and R. E. Stone, "Efficient second-harmonic generation in ktp crystals," *JOSA B*, vol. 3, no. 5, pp. 683–686, 1986.
- [117] R. Smith, "Theory of intracavity optical second-harmonic generation," *IEEE Journal of Quantum Electronics*, vol. 6, no. 4, pp. 215–223, 1970.
- [118] R. G. Brewer and E. Hahn, "Coherent two-photon processes: Transient and steady-state cases," *Physical Review A*, vol. 11, no. 5, p. 1641, 1975.

-
- [119] W. J. Kozlovsky, C. Nabors, and R. L. Byer, "Efficient second harmonic generation of a diode-laser-pumped cw nd: yag laser using monolithic mgo: linbo/sub 3/external resonant cavities," *IEEE journal of quantum electronics*, vol. 24, no. 6, pp. 913–919, 1988.
- [120] V. Arrizón, "Optimum on-axis computer-generated hologram encoded into low-resolution phase-modulation devices," *Optics letters*, vol. 28, no. 24, pp. 2521–2523, 2003.
- [121] L. Bergstein, "Modes of stable and unstable optical resonators," *Applied optics*, vol. 7, no. 3, pp. 495–504, 1968.

Appendix A

Crystal Materials

A.1 Nd:YAG Crystal

Neodymium Doped Yttrium Aluminum Garnet (Nd:YAG) Crystal is the most widely used solid-state laser material to date. Nd³⁺: YAG is a four-level gain medium, The energy diagram is shown in Fig. A.1. The Nd: YAG gain medium was pumped using a diode laser operating at 808 nm, laser emitted was 1064 nm. All the designated levels are populated to some extent due to pumping. The number of electrons in the energy states E₁, E₂, E₃, and E₄ will be N₁, N₂, N₃, and N₄. E₁, N₁ are at the ground level. Under active pumping the atoms raises from E₁ to E₄. Note that atoms at E₄ fast decay to E₃. Finally, lasing happens between E₃ and E₂. While atoms at E₂ then decay very fast to E₁.

Typically neodymium doping concentrations are of the order of 1 at.%. However, it varies according to the purpose of the user. The Nd: YAG gain medium is favourable in solid-state laser due to desired combination of optical, mechanical, and thermal properties. The properties are shown in Tab. A.1.

A.2 KTP Crystals

Potassium Titanil Phosphate (KTP or KTiOPO₄) is a nonlinear optical crystal, which has excellent nonlinear and electrooptic properties. KTP is widely used in frequency doubling of Nd-doped laser systems for green output. Optical properties are shown in Tab. A.2.

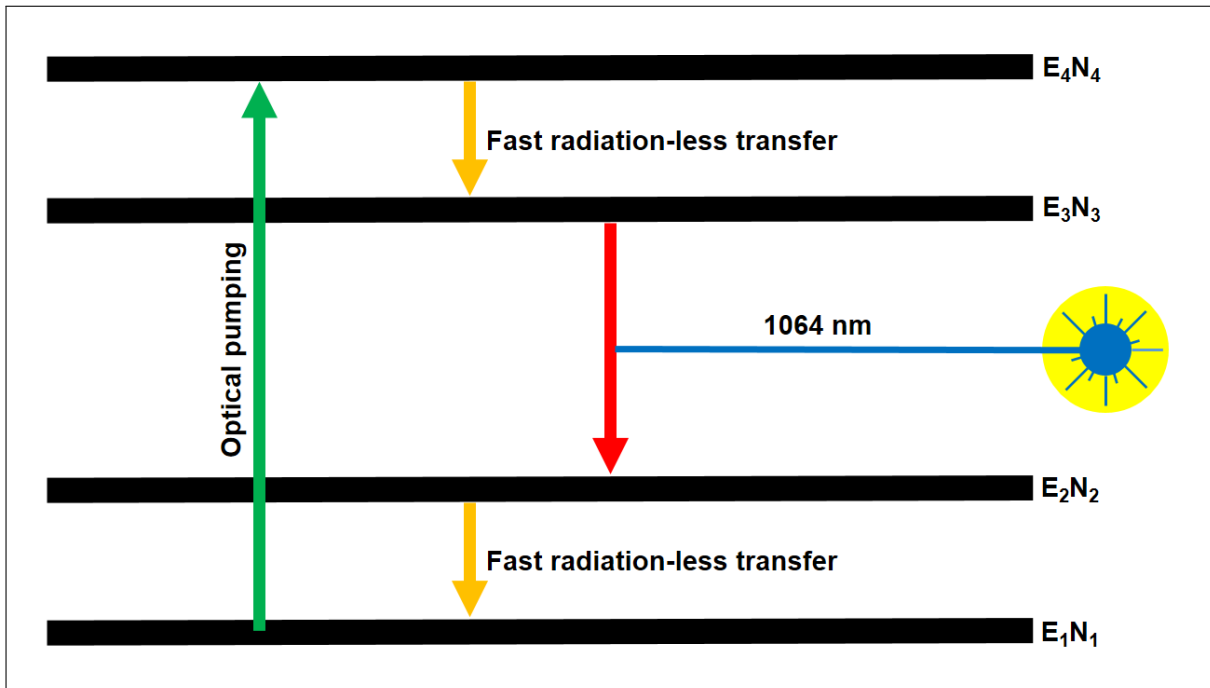


Figure A.1 Four energy level diagram for Nd:YAG laser principle of operation.

Table A.1 Nd: YAG optical properties.

Property	Value
Chemical formula	$\text{Nd}^{3+}:\text{Y}_3\text{Al}_5\text{O}_{12}$
Crystal structure	cubic
Mass density	4.56 g/cm^3
Moh hardness	8–8.5
Young's modulus	280 GPa
Tensile strength	200 MPa
Melting point	1970 °C
Thermal conductivity	10–14 W/(mK)
Thermal expansion coefficient	$7-8 \times 10^{-6} /\text{K}$
Thermal shock resistance parameter	790 W/m
Birefringence	none (only thermally induced)
Refractive index at 1064 nm	1.82
Temperature dependence of refractive index	$7-10 \times 10^{-6} /\text{K}$
Nd density for 1 at.% doping	$1.36 \times 10^{20} \text{ cm}^{-2}$
Fluorescence lifetime	230 μs
Absorption cross section at 808 nm	$7.7 \times 10^{-20} \text{ cm}^2$
Emission cross section at 1064 nm	$28 \times 10^{-20} \text{ cm}^2$
Gain bandwidth	0.6 nm

Table A.2 KTP optical properties.

Property	Value
Transmission range	350 nm ~ 4500 nm
Phase matching range	947 nm ~ 3400 nm
Refractive Indices @ 1064 nm	1.7377 (n_x), 1.7453 (n_y), 1.8297 (n_z)
Refractive Indices @ 532 nm	1.7780 (n_x), 1.7886 (n_y), 1.8887 (n_z)
Thermooptic coefficients in 0.4 – 1.0 μm range	$\partial n_x / \partial T = 1.1 \times 10^{-5} (\text{K})^{-1}$ $\partial n_y / \partial T = 1.3 \times 10^{-5} (\text{K})^{-1}$ $\partial n_z / \partial T = 1.6 \times 10^{-5} (\text{K})^{-1}$
Wavelength dispersion of refractive indices	$n_x^2 = 3.0065 + 0.03901 / (\lambda^2 - 0.04251) - 0.01247 \times \lambda^2$ $n_y^2 = 3.0319 + 0.04152 / (\lambda^2 - 0.04586) - 0.013377 \times \lambda^2$ $n_z^2 = 3.3134 + 0.05694 / (\lambda^2 - 0.05941) - 0.016713 \times \lambda^2$
Absorption coefficient	$\alpha < 1\% / \text{cm}$ @ 1064 nm and 532 nm
Dielectric constant	$\epsilon_{eff} = 13$